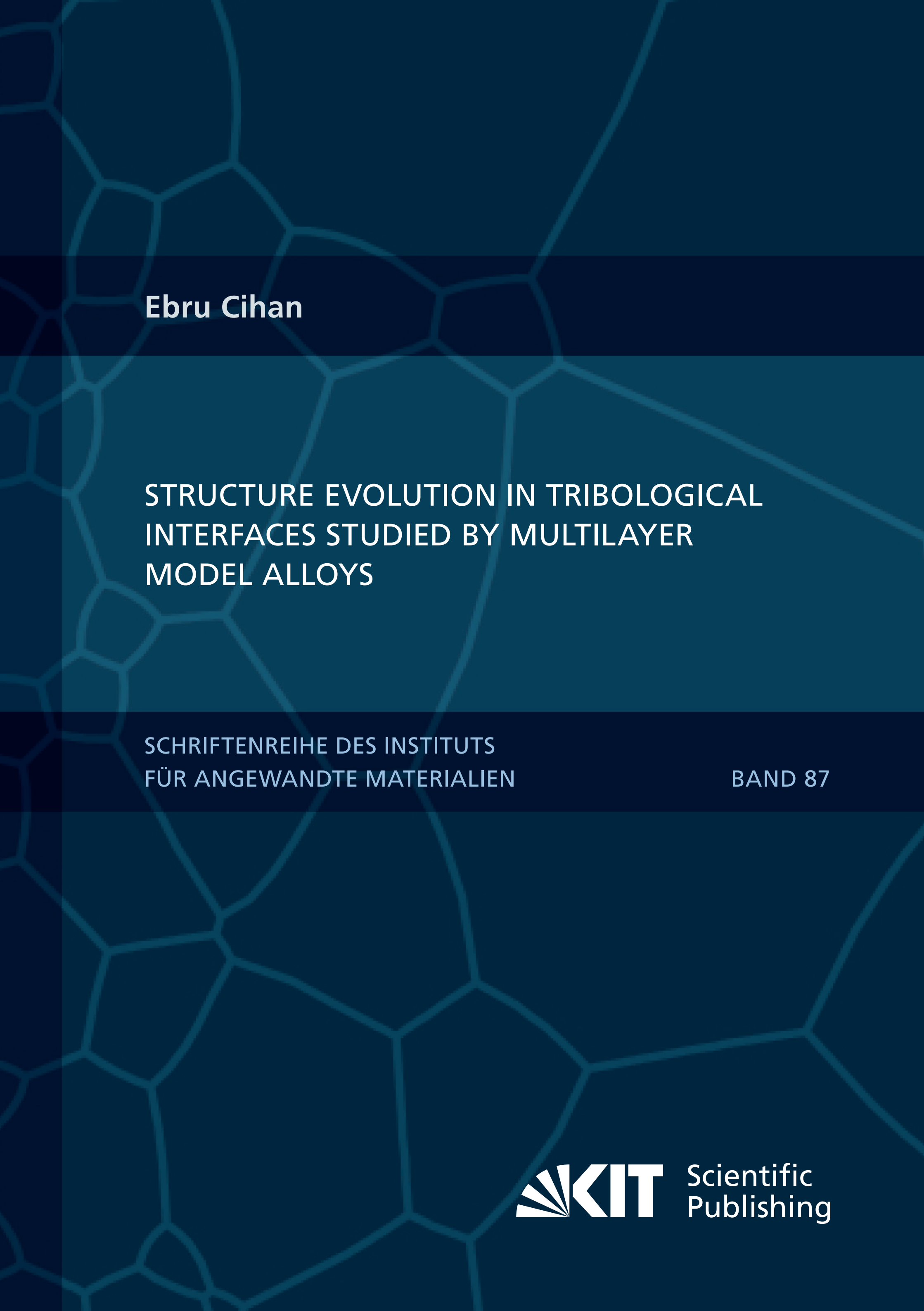

Ebru Cihan

STRUCTURE EVOLUTION IN TRIBOLOGICAL INTERFACES STUDIED BY MULTILAYER MODEL ALLOYS

SCHRIFTENREIHE DES INSTITUTS
FÜR ANGEWANDTE MATERIALIEN

BAND 87

KIT Scientific Publishing

Ebru Cihan

Structure evolution in tribological interfaces studied by multilayer model alloys

Schriftenreihe
des Instituts für Angewandte Materialien
Band 87

Karlsruher Institut für Technologie (KIT)
Institut für Angewandte Materialien (IAM)

Eine Übersicht aller bisher in dieser Schriftenreihe erschienenen Bände
finden Sie am Ende des Buches.

Structure evolution in tribological interfaces studied by multilayer model alloys

by
Ebru Cihan

KIT Scientific Publishing

Karlsruher Institut für Technologie
Institut für Angewandte Materialien

Structure evolution in tribological interfaces
studied by multilayer model alloys

Zur Erlangung des akademischen Grades eines Doktor der Ingenieurwissenschaften (Dr.-Ing.) von der KIT-Fakultät für Maschinenbau des Karlsruher Instituts für Technologie (KIT) genehmigte Dissertation

von M. Sc. Ebru Cihan

Tag der mündlichen Prüfung: 30. September 2019
Referent: Prof. Dr. rer. nat. Martin Dienwiebel
Korreferenten: Prof. Dr. Hendrik Hölscher, Prof. Dr. Andre Schirmeisen
Vorsitz: Prof. Dr.-Ing. Wolfgang Seemann

Impressum

KIT Scientific
Publishing

Karlsruher Institut für Technologie (KIT)
KIT Scientific Publishing
Straße am Forum 2
D-76131 Karlsruhe

KIT Scientific Publishing is a registered trademark
of Karlsruhe Institute of Technology.
Reprint using the book cover is not allowed.

www.ksp.kit.edu

This document – excluding the cover, pictures and graphs – is licensed under a Creative Commons Attribution-Share Alike 4.0 International License (CC BY-SA 4.0): https://creativecommons.org/licenses/by-sa/4.0/deed.en

The cover page is licensed under a Creative Commons Attribution-No Derivatives 4.0 International License (CC BY-ND 4.0): https://creativecommons.org/licenses/by-nd/4.0/deed.en

Print on Demand 2020 – Gedruckt auf FSC-zertifiziertem Papier

ISSN 2192-9963
ISBN 978-3-7315-0999-8
DOI 10.5445/KSP/1000100033

Abstract

Understanding of the governance of friction and wear of metallic surfaces is of an on-going endeavor for engineers and scientists since when examining the industrial world of the 21st century; one would definitely meet with a considerable amount of energy dissipation during friction processes that brings about huge economic impact. Furthermore, it becomes extremely difficult to predict friction and wear behavior of metallic surfaces when the influence of sub-surface deformations during sliding is taken into account. Recent studies of deformation mechanisms of metals and alloys pioneer the better investigation of the friction and wear behavior of materials with well-defined initial microstructures. Within this scope, in this thesis, the effect of sub-surface deformations on the resulting friction and wear behavior has been searched by means of a systematic experimental study on Au-Ni metallic multilayer model alloy system.

The sliding experiments performed with Au-Ni multilayer samples under ultrahigh vacuum (UHV) conditions demonstrated that the individual layer thickness of multilayer systems has a strong impact on friction due to the transition in the dominant deformation mechanism near the surface. The experiments also prescribed a new route for lowering the friction force of metallic material systems in dry, clean contact by providing more stable microstructures (i.e alloy formation). Through the ultrafine grains formed by mechanical mixing the number of grain boundaries increased and hence, grain boundary-mediated deformation resulted in the low friction coefficient. As the number of sliding cycles increased, the formation of the metastable microstructure between Au and Ni metals has been maintained to a certain extent (i.e. up to the fracture of the tribolayer).

In an attempt to contribute to the examination on the effect of the environment on friction and wear of metallic materials, the second part of the experiments has been carried out in a controlled N_2 atmosphere. Although a significant increase of the COF with increasing layer thickness has been found as already encountered under UHV conditions, the friction forces were higher than that observed in vacuum. Distinctive microstructure evolution as well as wear behavior has also been obtained due to the different interface characteristics during sliding.

Zusammenfassung

Das Verständnis von Reibung und Verschleiß metallischer Oberflächen ist eine kontinuierliche Herausforderung für Ingenieure und Wissenschaftler – würde man die industriellen Prozesse des 21. Jahrhunderts insgesamt betrachten, ergäbe sich eine beachtlicher Energieaufwand durch Reibungsprozesse mit entsprechend großen wirtschaftlichen Auswirkungen. Es ist darüber hinaus sehr schwierig, Reibung und Verschleiß metallischer Oberflächen vorherzusagen, wenn der Einfluss der Randzonenverformung berücksichtigt werden soll. Studien zu den Verformungsmechanismen von Metallen und Legierungen ermöglichen ein besseres Verständnis der Reibungs- und Verschleiß-mechanismen von Werkstoffen mit genau definierten Ausgangsgefügen. In diesem Rahmen wurde in der vorliegenden Arbeit der Einfluss der Randzonenverformung auf das gemessene Reibungs- und Verschleißverhalten über eine systematische experimentelle Studie an einem Au-Ni-Multilagenmodellsystem untersucht.

Die Reibexperimente, die an Au-Ni Multilagenproben unter Ultrahochvakuum-edingungen (UHV) durchgeführt wurden, zeigten, dass die Dicke der einzelnen Schichten im Multilagensystem einen starken Einfluss auf die Reibung hat. Grund dafür ist der Übergang der vorherrschenden Verformungsmechanismen nahe der Oberfläche. Die Versuche geben auch einen neuen Ansatz vor für metallische Systeme in trockener und sauberer Umgebung vor: Die Verringerung der Reibkraft kann durch stabile Gefüge, z.B. über Legierungen, erreicht werden. Durch die ultrafeinen Körner, die durch mechanische Vermischung gebildet wurden, erhöht sich die Zahl der Korngrenzen. Die Verformung über die Korngrenzen ergibt einen niedrigen Reibungskoeffizienten. Mit zunehmender Zyklenzahl bildete sich ein

metastabiles Gefüge aus Au und Ni, das bis zum Bruch der Triboschicht erhalten blieb.

Um den Einfluss der Umgebung auf Reibung und Verschleiß metallischer Werkstoffe zu betrachten, wurde der zweite Teil der Versuche unter definierter Stickstoffatmosphäre durchgeführt. Wie bereits unter UHV-Bedingungen wurde ein deutlicher Anstieg des Reibungskoeffizienten mit zunehmender Schichtdicke gefunden. Die Reibungskräfte waren jedoch insgesamt höher als unter UHV-Bedingungen. Aufgrund der anderen Grenzflächeneigenschaften wurde verglichen zu den UHV-Bedingungen ein unterschiedliches Verschleißverhalten als auch eine andere Randzonengefügeentwicklung gefunden.

Acknowledgement

First and uppermost, I would like to thank my academic advisor, Prof. Dr. Martin Dienwiebel, for providing me the opportunity to work at the Institute for Applied Materials-Computational Materials Science (IAM-CMS) and the Fraunhofer Institute for Mechanics of Materials (IWM)-MicroTribology Center (µTC). I also would like to express my gratitude to him for his valuable support and guidance throughout my dissertation.

I would like to thank Prof. Dr. Hendrik Hölscher and Prof. Dr. Andre Schirmeisen as the co-referees in the committee for investing time in reviewing this thesis. I would like to also thank Prof. Dr. Wolfgang Seemann as the chairman of the oral examination.

I really appreciate the significant advices Prof. Dr. Peter Gumbsch and Prof. Dr. Matthias Scherge gave me thorough the medium of highly productive discussions during our institute meetings.

I am very grateful to the Karlsruhe House of Young Scientists (KHYS) community for the research travel grant, as an excellent opportunity for a PhD student who wants to widen his/her scientific horizon. In this regard, I would like to thank Dr. Michael Chandross and Dr. Nicolas Argibay for welcoming me in their research group at Sandia National Laboratories in Albuquerque, USA and their wholehearted hospitability during my stay there. I had the chance to work with the other group members Dr. John Curry, Brendan Nation, and Dr. Adam Hinkle whom I also would like to thank for their help in my daily life in Albuquerque. Dr. Brad Boyce, Katherine Jungjohann, and Douglas Pete also provided me valuable support during my scientific research at the

Center for Integrated Nanotechnologies (CINT) at Sandia National Laboratories.

I very much appreciate the collaboration with Dr. Harald Leiste, Dr. Michael Stüber, and Dr. Sven Ulrich for the growth of multilayer samples which are the origin of the results gathered in this thesis. Besides, Dr. Heike Störmer carried out the TEM/(S)TEM/HRTEM/EDXS analyses for corresponding multilayer samples subsequent to the friction experiments. In this regard, I would like to kindly thank her for the great contribution to this thesis through our fruitful discussion during the TEM sessions.

I would like to thank the members of the Applied Nanotribology research group for their company as colleagues, and also acknowledge the contribution of Eberhard Nold and Philipp Daum for the XPS analysis, Andre Blockhaus for the microtribometer setup suitable to the working conditions, Dr. Dominic Linsler for the nanoindentation analysis and the German translation of the abstract.

Furthermore, I would like to thank all my colleagues and technical people at KIT, especially at the IAM-CMS, for their support and the times we have spent together.

To tell the truth, a place can become special if and only if it is surrounded by the right people. In this sense, I would heartedly say that I have been very lucky thanks to my friends in Karlsruhe who are of great value for me. Besides, I have achieved a family bliss through my little sweets *Ela* and *Can*, and their lovely parents *Şafak* and *Arda*; therefore, I could consider myself luckier than ever before.

The last but not the least, I would like to thank *my dear family* for their endless love and belief in me, and their support all the time. My life has undoubtedly taken on a new meaning in the recent year thanks to my little, cute niece *Belemir*, who definitely upgrades my endurance throughout the writing process.

I would like to put an end to this section with the person who left his mark in history, and has been a 'lodestar' for a despaired nation in the light of the truest guiding principles. *Mustafa Kemal Atatürk*, who is the unique leader of Turks, has always been a great motivator for me as a prescient and hardworking man. In this regard, I would like to gratefully address to his quote "Our true mentor in life is science (Hayatta en hakiki mürşit ilimdir)" in which I do believe deeply.

Karlsruhe, October 2019 Ebru Cihan

Table of Contents

Abstract .... **i**

Zusammenfassung .... **iii**

Acknowledgement .... **v**

1 Introduction **1**

1.1 Overview 1

1.1.1 Tribology: The science of friction, lubrication, and wear 2

1.1.2 Significance of nanotribology 3

1.1.3 Continuum mechanics theories 4

1.2 Microstructure evolution during sliding 5

1.2.1 Plastic deformation of multi-asperity contact 6

1.2.2 Microstructural changes of metallic materials during sliding : Third-body formation, transfer and mixing ... 7

1.2.3 Effect of microstructure on metallic friction 14

1.3 Effect of environment on metallic friction 19

1.4 Tribology of multilayer thin films 22

1.5 Scope of this thesis 25

2 Materials and Methods **27**

2.1 Abstract 27

2.2 Principle of methods 27

2.2.1 Magnetron sputtering 27

2.2.2 X-ray diffraction (XRD) …………………………… 29

2.2.3 Atomic force microscope (AFM) ……………………... 30

2.2.4 Nanoindentation …………………………………… 33

2.2.5 X-ray photoelectron spectroscopy (XPS) …………… 35

2.2.6 UHV microtribometer ……………………………... 37

2.2.7 Microtribometer utilized in nitrogen (N_2) atmosphere … 40

2.2.8 Focused ion beam (FIB) / scanning electron microscope (SEM) ………………………………………… 41

2.2.9 Tranmission electron microscope (TEM) / energy dispersive x-ray spectroscopy (EDXS) / high resolution (HR)TEM ………………………………………… 43

2.2.10 Transmission Kikuchi diffraction (TKD) …..………… 45

2.3 Materials ……………………………………………….. 47

2.3.1 Selection of materials: gold and nickel ……….……… 47

2.3.2 Preparation and structural characterization of Au-Ni multilayers ……………………………………….. 49

2.3.2.1 Growth of multilayers ……………………... 49

2.3.2.2 Crystallographic identification via XRD …..... 51

2.3.2.3 Roughness analysis via AFM …………….. 54

2.3.2.4 Nanoindentation hardness measurements …..... 55

2.4 Friction tests and characterization of worn Au-Ni multilayers . 58

2.4.1 Friction tests under UHV conditions ………………… 58

2.4.1.1 Cleaning the sample surface prior to the friction tests, via Ar sputtering 59

2.4.2 Friction tests under N_2 atmosphere 61

2.4.3 Post-sliding microstructure observation of Au-Ni multilayers 61

2.4.3.1 TEM lamella preparation via FIB/SEM 61

2.4.3.2 Microstructure evolution via TEM/HRTEM ... 65

2.4.3.3 Microstructure evolution via TKD 65

3 Results 67

3.1 Abstract 67

3.2 Friction behavior of individual metallic multilayer system 67

3.2.1 Friction behavior under UHV conditions 67

3.2.2 Friction behavior under N_2 atmosphere 69

3.3 Microstructure characterization of individual metallic multilayer system subsequent to the friction tests for 100 cycles 72

3.3.1 Microstructure characterization under UHV conditions . 72

3.3.1.1 Cross-sectional (S)TEM analysis via TEM 74

3.3.1.2 TEM/HRTEM analysis 83

3.3.2 Microstructure characterization under N_2 atmosphere ... 85

3.3.2.1 Cross-sectional (S)TEM analysis via TEM 85

3.3.2.2 TEM/HRTEM analysis 89

3.4 Microstructure characterization of the 10 nm and 100 nm Au-Ni multilayers subsequent to the friction tests for 1000 cycles under UHV conditions 93

3.4.1 Cross-sectional FIB/SEM analysis 93

3.4.2 Cross-sectional (S)TEM analysis via TEM 94

3.4.3 TEM analysis 97

3.5 Summary of the results 98

4 Discussion 101

4.1 Abstract 101

4.2 Distinctive microstructure evolution of metallic multilayers worn under UHV conditions 101

4.2.1 'Partially mixing' case: formation of vortex-like structures 102

4.2.2 'Fully mixing' case: formation of the metastable AuNi alloy 103

4.2.2.1 Grain coarsening beneath the intermixinig tribolayer 105

4.2.2.2 Severance of the intermixinig tribolayer 106

4.2.3 Tribologically deformed-layer for the unmixing case: formation of the pile-up 106

4.3 Distinctive microstructure evolution of metallic multilayers worn under N_2 atmosphere 108

4.3.1 Tribologically deformed-layer 108

4.3.1.1 Severance of the tribolayer 109

4.4 Comparison of the friction behavior with regard to the microstructure evolution under UHV conditions and N_2 atmospehere 110

4.5 A model based on the relationship between microstructure, deformation mechanism, and friction behavior …………… 117

4.5.1 Predictions from the model for corresponding UHV results ………………………………………... 120

4.5.2 Limitations of the model for our material system …… 124

5 Conclusions ……………………………………….……….... **127**

6 Outlook ……………………………………………………... **131**

Bibliography …………………………………………………….. **135**

Appendix Figures ……………………………………………... **153**

Dissemination ………………………………………………… **157**

1 Introduction

1.1 Overview

Friction is a prevalent phenomenon in our daily lives, which even controls simple actions such as walking and writing with a pencil. It is the physical resistance against the relative movement of two contacting surfaces. As a natural phenomenon occurring also between rocks, friction can arise from a seismic slip during earthquake [1]. Furthermore, as the main mechanism responsible for energy dissipation, it has great significance for many industrial processes (i.e. forging and extrusion) and advanced mechanical systems such as micro- and nanoelectromechanical systems (MEMS/NEMS) [2, 3]. It has been reported that in the automotive industry, one-third of the fossil fuel energy is dissipated frictionally [4]. Besides, as a physical phenomenon, friction is important for several biological systems, i.e. musculoskeletal system [5, 6] and processes such as mechanical interactions between cells [7]. The physical process of friction dissipation is based on the conversion of the motion energy (so-called the kinetic energy) to the thermal energy during sliding. As a practical manifestation of this principle, this characteristic of friction has been utilized since ancient times (the Lower Palaeolithic Era ≈ 1 million years ago) to obtain fire by rubbing two pieces of wood against each other [8].

1.1.1 Tribology: The science of friction, lubrication and wear

Tribology can be defined as the science and technology of friction, lubrication and wear, and has been accepted as the key technology in most mechanical systems [9]. It has been noted for hundreds of years to study this particular fact because the performance of many systems is mainly controlled by tribology. However, since friction is the main source of energy dissipation in many different processes, it has a significant impact on the world economy [10]. Therefore reducing friction and wear has been of key parameter from both scientific and technical point of view, and the ancient Egyptians can be exemplified as the first lubricant users for that manner [11].

Leonardo da Vinci (1452-1519) can be considered as the father of modern tribology. Although he discovered the classical rules of sliding friction [12, 13], he did not publish these results in his lifetime. Around 150 years later, Guillaume Amontons (1663-1705) introduced “Amontons’ Laws of Friction” in which he explained the nature of friction on the macroscale [14]. His first law emphasizes that the friction force is directly proportional to the applied load whereas the second law states that the friction force is independent from the contact area. Belidor (1698-1761) further developed these observations with a rough surface, and Leonard Euler (1707-1783) made the first discrimination among kinetic and static friction [15]. After these discoveries, Charles-Augustin Coulomb (1736-1806) studied in detail the effects of the structure of the contacting surfaces, the size of the contact area, the applied load and the time spent in contact, and then he introduced “Coulomb’s Law of Friction” in which he showed the independence of the kinetic friction from the sliding velocity [16].

The coefficient of friction (COF), μ was described as the proportionality constant between the friction force, F_F and the normal load, F_N as follows [17]:

$$F_F = \mu F_N \tag{1.1}$$

Later on, Bowden and Tabor indicated that at the macroscopic scale, the real contact area (A) must be smaller than the apparent contact area (A_a). It is likely that the real contact area, A is formed due to a number of small asperities on the contacting surfaces, which results in a multi-asperity nature [18]. Then, the friction force becomes directly proportional to the real contact area, A:

$$F_F = \tau A \tag{1.2}$$

where τ is the shear strength of the material. Bowden and Tabor proposed that the applied pressure might be sufficiently high to plastically flow the asperities in contact of two rough surfaces, in that the real contact area, A rises up to a certain level where the yield stress of the material exceeds the contact pressure. In this latter case, the real contact area, A would be proportional to the pressure remaining on it.

1.1.2 Significance of nanotribology

When tribological studies are performed on the nanometer scale (1-100 nm) with the aim of understanding the fundamental mechanisms of sliding friction, the term ‘nanotribology’ is assigned [19, 20].

The importance of nanotribology arises from the fact of multi-asperity nature of the macroscopic contacts composing of nano-/micro scale single-asperities. As such, in order to clarify the fundamental mechanisms of sliding friction, observations of single-asperity contacts are needed. After the invention of the surface force apparatus (SFA) in 1969 by Tabor and Winterton [21] and of the atomic force microscopy (AFM) in 1986 by Binnig, Quate, and Gerber [22], the applications of nanotribology were made possible. Particularly, the use of AFM in friction measurements has led to the manifestation of the friction force microscopy (FFM) in 1987 by Mate et al. [23] which enables obtaining various fundamental phenomena such as stick-slip behavior of atomic scale friction [24] and superlubric sliding [25], alongside of being conducive to the investigation of friction behavior on different material or material pairs [26-47].

1.1.3 Continuum mechanics theories

A number of approaches in contact mechanics have been proposed to determine the behavior of elastic deformation of two contact bodies exposing the compressive stresses. The first theory was introduced by Hertz in 1882 [48], in which he described two elastic spherical contacts with radii R_1 and R_2 (Figure 1.1) that form a contact circle with the radius, a, under the applied load, F_N. The contact radius, a, can be specified in the Hertzian contact mechanics approach:

$$a = \left(\frac{3\, F_N\, R}{4\, E^*} \right)^{1/3} \tag{1.3}$$

where $\frac{1}{R} = \frac{1}{R_1} + \frac{1}{R_2}$, and $\frac{1}{E^*} = \frac{1 - \nu_1^2}{E_1} + \frac{1 - \nu_2^2}{E_2}$. E and ν express the Young's modulus and Poisson ratios of the contacting surfaces. Additionally, by substituting the Equation 1.3 into the Equation 1.2, and assuming that τ is constant, a “2/3” power law dependence of the friction force on the applied load is achieved:

$$F_F = \tau \pi \left(\frac{3R}{4E^*} \right)^{2/3} F_N^{\;2/3} \tag{1.4}$$

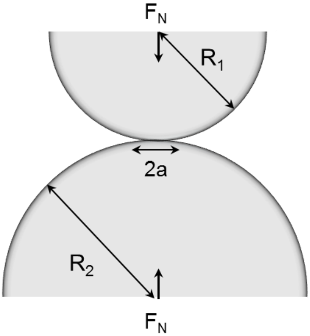

Figure 1.1: Schematic view of two elastic spherical contacts with radii R_1 and R_2 when pressed against each other, adopted from [9]. They form a contact circle with the radius, a, under the applied load, F_N , during elastic deformation.

This model was then developed by Johnson, Kendall and Roberts (the JKR model) in 1971 with supplementing the adhesive forces inside the contact area [49]. Herewith, the adhesive term increases the size of the contact, in which a negative force (pull-off force) is needed to separate the surfaces in contact. Thereafter, in addition to the adhesive forces, the Derjaguin-Muller-Toporov (DMT) model considered the attractive forces outside of the Hertzian contact area [50, 51]. Eventually, the Maugis-Dugdale (MD) theory was introduced as a composition of all these theories in 1992 [52].

1.2 Microstructure evolution during sliding

Deformation of the contacting bodies can be broadened from a few nanometers to meters and is dependent upon the materials in contact, applied stresses, and strains as the material response. As a matter of fact, the sliding interface is affected by large plastic strains generated during sliding and in this case, modifications in the microstructure near to the surface would be inevitable. Therefore, it is of critical importance to become familiar with the deformation behavior of tribological contact pairs before dealing with them.

1.2.1 Plastic deformation of multi-asperity contact

Regarding the von Mises stress distribution on sub-surfaces under tribological loading, Hamilton and Goodman made their first assumption in 1966, in which they studied the complete stress field of a Hertzian point contact that is proportionally distributed at the sub-surface [53]. Later on, Hamilton moved this assumption forward by the investigation of the stress fields (tensile and compressive stresses existing in the direction of sliding) for a Hertzian point contact, in which he found that the maximum stress resides at the trailing edge of the contact near to the surface [9, 54]. According to the Hamiltonian model, the maximum stress, σ during sliding can be determined as follows:

$$\sigma = P_0 \left(\frac{1 - 2\nu}{3} + \frac{4 + \nu}{8} \pi \mu \right) \tag{1.5}$$

where P_0 is the maximum pressure at the center of the contact (r = 0).

One of the early investigations for the contact of rough surfaces was made by Greenwood and Williamson and they argued that every single contact-asperity has spherical nature within the same radii which deforms elastically under a Hertzian contact pressure [55]. Although their model was produced for the elastic contacts, it does enable predicting the origin of plastic deformation at the contact-asperities as well [9].

1.2.2 Microstructural changes of metallic materials during sliding: Third-body formation, transfer and mixing

Metallic surfaces that are subjected to sliding friction often develop new microstructures (e.g. wear debris particles), phases or compositions which are not present in the original material at the near surface [56-58] (Figure 1.2). The development of these so-called 'third-bodies' or tribomaterials [59] strongly influences the frictional and wear behavior of tribological systems and many examples exist for technical alloys and pure metals [60-70]. According to Rigney et al. [71], the main factors affecting the generation of the third-bodies at the sub-surface during sliding can be arrayed in this way:

- Large plastic strains and strain gradients,
- High strain rates and strain rate gradients,
- Mechanical mixing of the constituents from either surfaces in contact or from the environment,
- Different recovery processes.

As stated, shear deformation of the interfaces can differ from each other and a number of experimental parameters such as sliding velocity, applied load, temperature and environment, as well as the mechanical properties of the interface materials such as hardness and yield strength can influence the resulting behavior. As a connective consequence of all these features, the distribution of the shear stress and strain would lead to observing different deformation levels near to the surface beneath the wear track. Figure 1.3a displays such an example, in which the ultrafine grains are remarkable at the very surface of copper whereas coarser grains are further developed beneath this region throughout sliding [72].

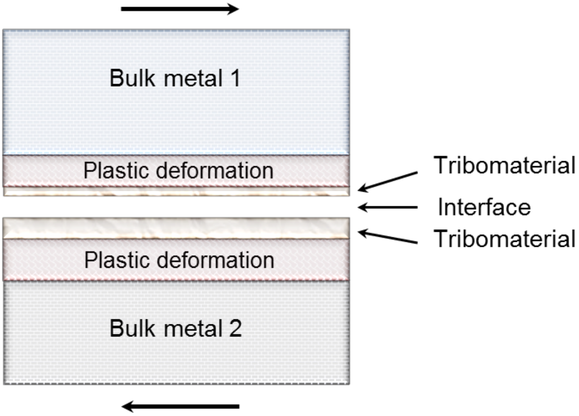
Bulk metal 1
Plastic deformation
Tribomaterial
Interface
Tribomaterial
Plastic deformation
Bulk metal 2

Figure 1.2: Basic illustration of a tribological contact pair adopted from [71]. Plastic deformationtakes place as sliding is in progress. Tribomaterial develops near to the sliding interface due to the modifications in local asperity contacts forced by the strain and strain rate gradients. Composition of the tribomaterial may either differ from bulk metals (mechanical mixing with the bulk metals and/or the environment) or remain unchanged. While observed tribomaterial is frequently nanocrystalline, amorphous structure can either be obtained, for example, in the case of mixing with O_2. Wear debris particles might be produced sometimes in the tribomaterial.

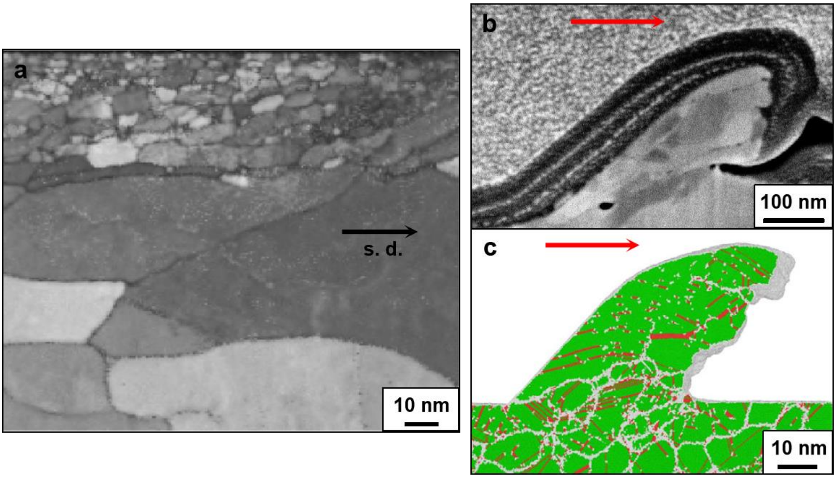

Figure 1.3: Different examples of the deformation at the sliding interface. (a) Cross sectional image of a worn copper surface under dry sliding conditions [72]. Modified figure from M. Chandross et al., Scripta Materialia 143, 54-58 (2018), with DOI link: https://doi.org/10.1016/j.scriptamat.2017.09.006. Creative Commons Attribution-NonCommercial-No Derivatives License (CC BY NC ND). Copyright (2017) by Elsevier. (b) Cross-section of an experimentally plowing nanocrystalline copper chip by an AFM tip [74]. (c) Chip cross-section from the atomistic simulation (at t = 6.5 ns). (b-c) Reprinted figures with permission from [N. Beckmann et al., Physical Review Applied 2, 064004 (2014)]. Copyright (2014) by the American Physical Society.

Moreover, bulging and coarsening during sliding can be seen where the surrounding material is dragged throughout sliding over the surface material, which causes the strong roughness at the surface. As an example to the case at microscale, the study within the AISI 52100 steel slid over an interface consisting of Au coated-AISI 1020 steel can be given [73]. This latter process can also be observed at nanoscale. Figure 1.3b depicts a cross section of a nanocrystalline copper chip plowed by an AFM tip while the atomistic simulation (Figure 1.3c) is also in agreement with the experimental result [74].

The grains with suitably oriented slip systems led to the plastic flow throughout plowing, which resulted in bulging and folding of the material. Hence, the plasticity instabilities can be held accountable from the formation of folding on polycrystalline surfaces.

In order to understand the accurate mechanisms underlying the interfacial interactions of the two sliding bodies, molecular dynamics (MD) simulations have a great potential. As a good example, an atomistic approach to the experimentally observed third-body structure at the tungsten (W) / tungsten carbide (WC) interface by Stoyanov et al. [75] can be cited, where the roughness of the two contacting bodies is specifically examined (Figures 1.4-5). For the “flat on flat atomistic sliding” the researchers reported that, at the beginning of the simulations, a binding of the uppermost layer of the W body to the C atoms of the WC body occurred and this led to the formation of a W-transfer monolayer at the sliding interface (Figure 1.4a). By further sliding, W atoms moved to the next W adlayer causing the development of a W-rich region (Figure 1.4b) which led to the nucleation and propagation of dislocations and changes in grain orientation through the W body (Figure 1.4c). And consequently, an amorphous tribolayer formed through the WC body by breaking the flatness of the W/WC interface (Figures 1.4d-e). The level of amorphization and the evolution of the shear stress are demonstrated in Figure 1.4f.

Amorphization of the WC layer has also been observed during a “rough on rough atomistic sliding”. For this latter case, MD simulations showed that the W multi-asperities make it difficult for the WC body to move in the beginning (Figure 1.5a). However, with further sliding, the C atoms started to mix with the W atoms which are already disordered (Figure 1.5b), and subsequently a mixed amorphous WC tribolayer is produced (Figure 1.5c-e). The level of amorphization and the evolution of the shear stress during sliding are demonstrated in Figure 1.5f.

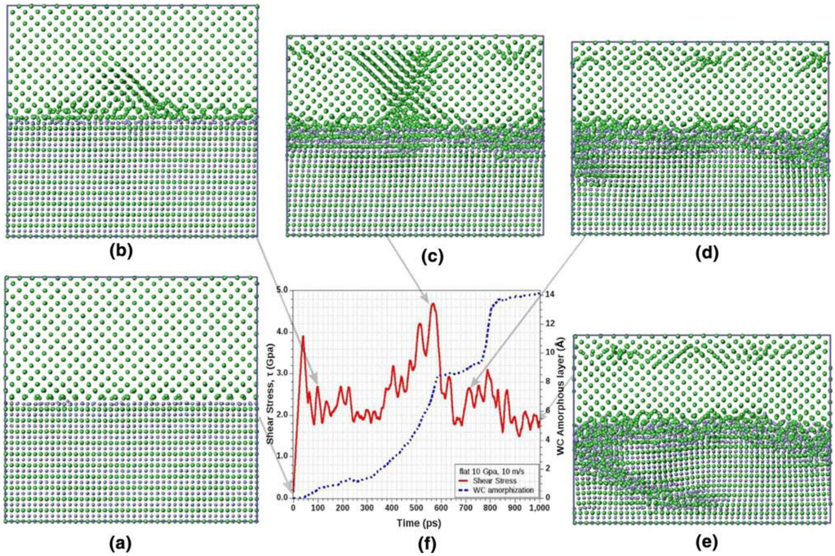

Figure 1.4: MD simulation of a "flat on flat atomistic sliding" within a pressure of 10 GPa and a sliding velocity of 10 m/s [75]. (a) Binding of the uppermost layer of the W body to the C atoms of the WC body occurred and a W-transfer monolayer at the sliding interface formed. (b) W atoms moved to the next W adlayer causing the development of a W-rich region. (c) The nucleation and propagation of dislocations and changes in grain orientation through the W body are observed. (d) The flatness of the W/WC interface started to break. (e) An amorphous tribolayer formed through the WC body. (f) The level of amorphization and the evolution of the shear stress during sliding. Reprinted by permission from Springer Nature: Tribology Letters, 50, Experimental and numerical atomistic investigation of the third-body formation process in dry tungsten/tungsten-carbide tribo couples, 67-80, P. Stoyanov, et al, Copyright (2012).

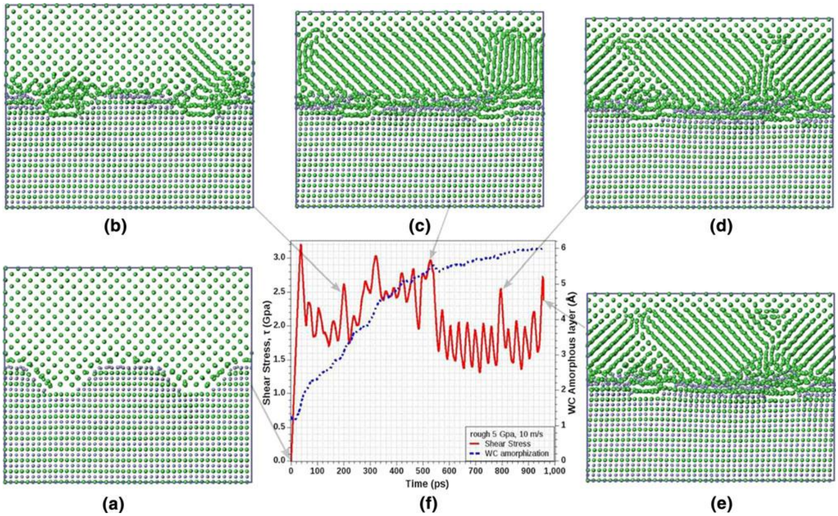

Figure 1.5: MD simulation of a "rough on rough atomistic sliding" within a pressure of 5 GPa anda sliding velocity of 10 m/s [75]. (a) The W multi-asperities make difficult for the WC body to move in the beginning. (b) The C atoms started to mix with the W atoms which are already disordered. (c-e) A fully mixed amorphous WC tribolayer formed. (f) The level of amorphization and the evolution of the shear stress during sliding. Reprinted by permission from Springer Nature: Tribology Letters, 50, Experimental and numerical atomistic investigation of the third-body formation process in dry tungsten/tungsten-carbide tribo couples, 67-80, P. Stoyanov, et al, Copyright (2012).

Furthermore, a mechanical mixing process during sliding is possible due to the formation of vortices in the tribomaterial [76-78]. The process for producing vortices to drive mechanical mixing has been described as a plastic flow process rather than a simple thermal diffusion [56]. Shear instabilities, instead of the Kelvin-Helmholtz instability in fluid dynamics, have previously been discussed to be responsible for the formation of vorticity when localized, inhomogeneous strains are generated among the contacting surfaces [71, 74]. The velocity profiles obtained via MD simulations have also supported the development of this atomic flow process in crystalline materials [79-81] for which the mechanism of mechanical mixing depends on the microstructure [74]. Essentially, localization of the grain size anisotropy has been accountable for the formation of the vortex-like structures at the near surface which would provide transferring the material and generating the nanocrystalline structure. It is likely that this process results in an increase in hardness due to the refinement of grains with respect to the Hall-Petch relation [82] whereas ductility diminishes [83]. However, there have been several studies [63-64, 84-87] where the breakdown of the Hall-Petch effect is demonstrated when a transition in the dominant deformation mechanism has been observed when a critical grain size has been reached. Sometimes, mechanical mixing processes driven by large plastic strains on sub-surfaces can be reinforced by mechanical alloying [88, 89]. It has been reported that this mechanism could even force the mixing of immiscible elements at equilibrium, such as Ag and Cu, Ag and Ni, and Au and Ni (the material pair selected in this thesis). Depending on the operating temperature [90, 91] where the thermally activated diffusion process is hindered during ball milling (even at cryogenic temperatures) and the initial surface grain size, applied stress and the exposure time to shearing [92], fully mixing of immiscible elements can be obtained under non-equilibrium conditions. In order to be able to realize the aforesaid situation, a sufficient amount of stress and/or time must be provided, and more importantly, the critical grain size for the material transfer must be achieved as handled in detail in Chapter 4.

1.2.3 Effect of microstructure on metallic friction

As indicated earlier, the work by Bowden and Tabor [93, 94] contributed greatly to our knowledge of contact mechanics of solid metals. They developed a new equation where the friction force, F_F is expressed as the product of the real contact area, A, and shear strength of the softer material, τ, $F_F = \tau A$ (Equation 1.2). By substituting Equation 1.2 into the Equation 1.1 and using the relation $F_N = PA$, the coefficient of friction (COF) can be defined as follows:

$$\mu = \frac{F_F}{F_N} = \frac{\tau A}{A\, P} = \frac{\tau}{P} \tag{1.6}$$

where P is the Hertzian contact pressure or flow (yield) stress of the softer metal. The concept of 'soft-hard' metal contacts is illustrated in Figure 1.6a while Figure 1.6b shows a hard-hard metal contact in which lower friction coefficient is expected due to the smaller contact area. Principally, a higher COF would be expected as the contact area increases (due to the tendency to ploughing); however, some of the experiments have shown contradictory results in the case of lubrication and/or the formation of a thin film at the sliding interface. To give an example, Bowden and Tabor coated a hard steel substrate with indium metal in the form of a thin film and observed a lower friction coefficient with increasing applied load compared to that in the uncoated steel although the contact area appeared to be risen (Figure 1.6c). It is quite clear that the indium thin film acted as a solid lubricant which is responsible for lowering the COF. As stated previously, Amontons first law of friction says that the friction coefficient of a sliding system depends on the applied load; however in this latter case, opposite observations were recorded. This situation can be verified by the following equation for the elastic contact deformation:

$$\mu = \tau \pi \left(\frac{3R}{4E^*} \right)^{2/3} F_N^{-1/3} \tag{1.7}$$

in which a minimal increase in the area of contact leads to a slight change in the friction force. Since this change is very small in comparison with the applied load ($\mu \propto F_N^{-1/3}$), a certain decrease in the COF, μ is expected [95].

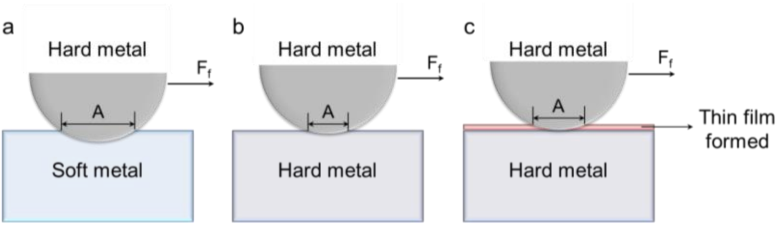

Figure 1.6: Basic illustration of relation of friction force to metal substrate hardness ($F_F = \tau A$) adopted from [95]. (a) Hard metal in contact with soft metal (small τ and large A). (b) Hard metal in contact with hard metal (large τ and small A). (c) Hard metal in contact with hard metal separated by a thin film (lubricant) on one metal surface (small τ and small A).

As explained earlier, sub-surfaces are inclined to the structural modifications due to the large plastic strain gradients generated during sliding of the surfaces in contact. These arisen instabilities might lead to forming folding or cracking at the sub-surface in which an increment in the coefficient of friction (COF) can be usually observed due to the rougher sliding surface that can be ploughed more easily. When sliding is maintained on that rippled surface, wear debris particles may be developed and, mechanical mixing/alloying between particles and sliding surface can even be processed towards obtaining a nanostructured tribomaterial which also can lower the COF. If sliding is continued, a modified surface might cause delamination of the tribomaterial which is more brittle than that obtained in the former case, and under these circumstances, the COF will be higher [68].

When the influence of friction and wear on world economy, associated with attaining main source of energy dissipation during different industrial processes, is considered, reducing the COF and/or the amount of wear is of great importance from either a scientific or an engineering perspective. For that manner, a number of studies have been done particularly aiming to provide nanostructured tribomaterial under both dry and lubricated sliding conditions [62-64, 68, 85-87, 92, 96-104].

To give an example, both high and low steady-state friction values can be obtained during sliding of an initially nanocrystalline structure [64]. Following a temporary COF at the beginning, Padilla et al. encountered with either a low COF as of 0.2 with less fluctuation or a high COF as of 0.8 with large fluctuation in their work. By considering sub-surface deformation, they accounted for this duality in friction behavior in four stages: **(a)** A temporary COF is evaluated at the very beginning. **(b)** As the sub-surface structure is deformed by means of high shear stresses due to the various magnitudes and gradients, different scaled grains are generated. Because the strength between the regions (layers) with ultra-nanocrystalline (UNC) grains, coarsed grains (CG) and nanocrystalline (NC) grains differs from each other, the stress distribution would be the key parameter to determine the friction behavior. **(c)** If the interfacial stress between the UNC and CG layers exceeds the threshold for delamination, then sub-surface structure will be delaminated and result in a high COF with large fluctuations. **(d)** On the other hand, if the delamination threshold is not exceeded (lower stress magnitude), the UNC layer will accommodate shear which leads to reduce the COF. This process is summarized in Figure 1.7.

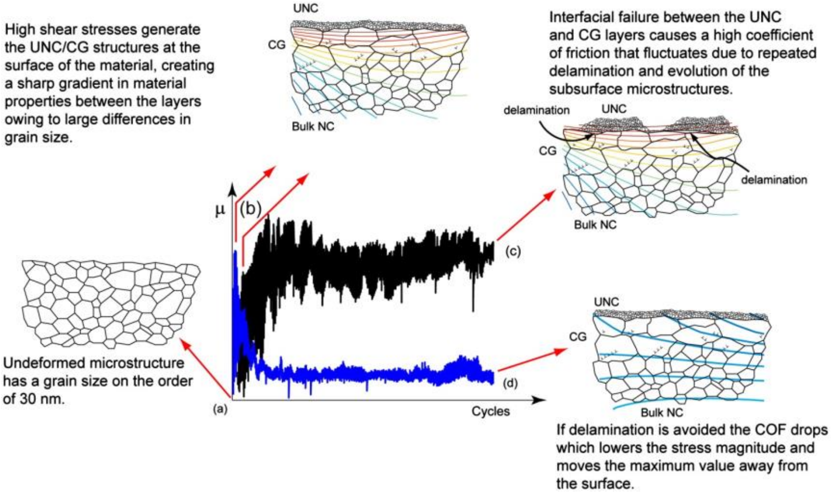
High shear stresses generate the UNC/CG structures at the surface of the material, creating a sharp gradient in material properties between the layers owing to large differences in grain size.
UNC
CG
Bulk NC
Interfacial failure between the UNC and CG layers causes a high coefficient of friction that fluctuates due to repeated delamination and evolution of the subsurface microstructures.
delamination
UNC
CG
delamination
Bulk NC
μ
(b)
(c)
Undeformed microstructure has a grain size on the order of 30 nm.
(a)
(d)
Cycles
UNC
CG
Bulk NC
If delamination is avoided the COF drops which lowers the stress magnitude and moves the maximum value away from the surface.

Figure 1.7: Schematic view of the grain structure evolution associated with the high and low COFvalues [64]. (a) Sliding friction of a nanocrystalline structure at the very beginning. A temporary COF is evaluated. (b) Deformed sub-surface structure initially resulting in the high COF. Strength between the layers with ultra-nanocrystalline (UNC) grains, coarsed grains (CG) and nanocrystalline (NC) grains differs from each other. Note that magnitude and gradient of stresses relative to the physical dimensions are indicated with the color contour lines. (c) Delamination on the sub-surface microstructure resulting in the high COF with fluctuations in 'high stress magnitude'. Higher interfacial stress may lead to delamination if it can exceed the threshold. (d) If the delamination threshold is not exceeded (lower stress magnitude), the UNC layer accommodate shear which decreases the COF. Reprinted from Wear, 297, H. A. Padilla, et al., Frictional performance and near-surface evolution of nanocrystalline Ni–Fe as governed by contact stress and sliding velocity, 860-871, Copyright (2013), with permission from Elsevier.

Authors have reported that under lubricated sliding the COF can be decreased at relatively low sliding speeds [101, 102], however higher sliding speeds might still cause to observing higher COF apparently due to the high wear rate [102]. Comprehensive comparison between dry and lubricated sliding of WC against W revealed higher friction forces under dry conditions [103]. The reason here arises from the formation of the third-body between WC (observed amorphization) and W (grain refinement near to the surface) by the initial plowing events, which was also confirmed by MD simulations [75]. Even though the formation of the third-body is a matter of lubricated sliding as well, low viscose hexadecane monolayers inhibited a high friction behavior under lubricated conditions.

Indeed, as one can notice from previous literature data, dry sliding conditions for pure metals do not always contribute to a reduction of friction since shear-induced plastic strains grossly deform the sub-surface. In this case, the formation of the nanostructured tribomaterial to decrease the COF becomes useless because of the stress-strain instability near to the surface. Therefore, it is obvious that persistent microstructures on sub-surfaces are needed for stable and low friction behavior [68].

Recently, Argibay et al. proposed that it is possible to provide remarkably low friction at low applied stresses below an equilibrium surface grain size [87], where they described a feedback loop between maximum surface stress, σ, surface grain size, d, and friction coefficient, μ, as illustrated in Figure 1.8. There are a number of studies which state the deformation mechanisms as dislocation-induced deformation (grain size < 100 nm) and grain boundary (GB)-induced deformation (grain size < 20 nm) [64, 105-107]. At this stage, Argibay et al. interpolated the COF value into the equations of interest [107] and developed their model which points out that depending upon the applied stresses and initial microstructures, different deformation mechanisms which can control the friction behavior of the system can be observed [87].

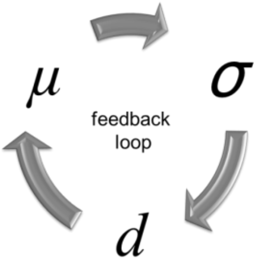

Figure 1.8: Feedback loop between friction coefficient, μ, surface stress, σ, and grain size, d, adopted from [87].

1.3 Effect of environment on metallic friction

In terms of its application, the environment can induce alteration of the sliding pairs. As opposed to many different industrial processes which are usually exposed to the ambient conditions (i.e. air), sliding under ultrahigh vacuum (UHV) conditions is necessary for more special-designed components, for example, in space technology. By the virtue of changes at the asperity level under different environments such as different chemical composition and morphology evolution in mechanical intermixing, friction and wear behavior of the materials based on their mechanical properties might be notably influenced. Therefore, it would be to the point to emphasize the friction and wear behavior of metallic components under different environments.

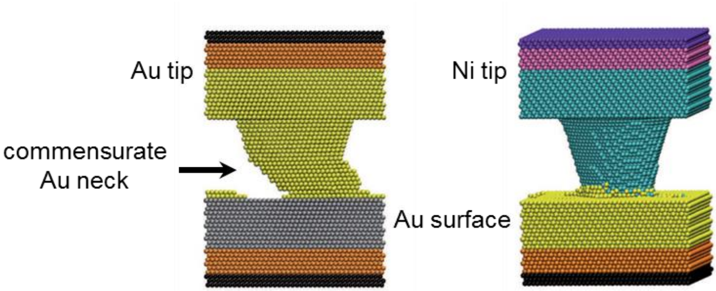

Figure 1.9: Snapshots from the atomistic simulation of the Au and Ni tips sliding over the Au surface, adopted from [108]. The junction growth (neck formation) between two Au surfaces (below 170 K, left figure) results in the high friction force compared to the much lower case where the diffusion of surface atoms at the interface is in dynamic equilibrium (above 170 K, right figure). Reprinted figure with permission from [N. N. Gosvami et al., Physical Review Letters 107, 144303 (2011)]. Copyright (2011) by the American Physical Society.

Change in composition and microstructure prevails for metals during sliding in both cases (i.e. ambient and UHV conditions); however, recorded COF values in air (for dry sliding) are typically much lower than in vacuum. The main reason for higher COF under vacuum can be explained due to the fact that strong adhesion is generally observed when two clean metal surfaces are brought into contact. The latter is caused by strong metallic bonds at the interface and usually, growth of junctions can take place depending on the ductility of the asperity material [9]. These are evidence for high friction behavior under UHV conditions. Although it much more suits to the topic on the effect of temperature on metallic friction (however this subtopic is not included in this thesis), the study by Gosvami et al., demonstrates the junction growth (neck formation) under UHV between two Au surfaces (below 170 K) as displayed in Figure 1.9 which results in the high friction force compared to the much lower case where the diffusion of surface atoms at the interface is in dynamic equilibrium (above 170 K). In this corresponding case, MD simulations very well supported the AFM measurements [108].

As mechanical mixing among the contact bodies can be seen in either atmosphere, ambient conditions make the interface more susceptible to mix with the adsorbed gases omnipresent in air. The most frequently encountered state here is the oxidation of metals to some extent, by forming oxide films which are usually between 1 and 10 nm thick. In such a case, the sliding behavior would be controlled by the structure of these oxide films. If the oxide film is penetrated during sliding, then the COF is directly determined by the interaction among the contacting bodies. However, if the surface oxidation is not broken, the oxide film itself determines the friction force since it still adheres to the metallic contact [9]. In the case of the presence of an oxide or another reaction-formed film at the interface, recorded COF values in air have generally been much lower than in vacuum. For instance, when the effect of oxygen (O_2) on the sliding friction of pure iron (Fe) is examined, researchers have seen a reduction in the COF with increasing the O_2 content [109]. It has also been reported that the low COF of a copper-copper (Cu-Cu) contact at low normal loads in air stems from the oxide film which separates the two metallic surfaces from each other and might act as a low shear strength film at the interface [9]. They also argued that the growth of junction between two Cu surfaces is inhibited at low loads with the help of the outsider (the oxide film) since higher friction force is recorded due to the formation of more strong metallic contact between Cu bodies as the applied load is increased.

1.4 Tribology of multilayer thin films

As stated earlier, the origin of the friction and wear mechanisms at the macroscopic level stems from the micromechanical mechanisms (about 1 µm or less down to the nm range) correlated with contacts at the asperity level, stress-strain formation and distribution, crack formation and propagation, and wear debris particle formation. However, in most instances, these factors cause complicated understanding of the mechanisms that govern friction and wear due to the unpredictable microstructural, chemical and topographical alterations through the medium of plastic deformation at the sliding interface. Thus, a better investigation of the microstructure and chemistry of the tribozones, i.e. tribolayer, tribomaterial, third-body or mechanically mixed material, within the interiors and boundaries, is needed [110]. In the present circumstances, multilayer thin films can become more attractive since they are extremely promising and can serve as model materials to be able to clarify the inexplicable tribology mechanisms.

Multilayer thin films consist of periodically repeated structures of two or more materials. If the thickness of individual layer is in the nanometer range, this structure is then classified as 'superlattice' [111]. First studies on the growth of multilayered films were performed at the Los Alamos Laboratories, USA in the late 1970s [112]. The researchers mainly aimed to hinder the formation of dislocation and its mobility based on Al/Al_xO_y films deposited via physical vapor deposition (PVD) system. Later on, metal/metal multilayer pair were also examined and better mechanical properties were recorded as the layer thickness decreases [113]. Many other studies have also been done to further reveal the benefits of multilayered systems [111, 114-116].

In the course of compression of multilayer thin films, one layer can be the alternative for another to accommodate shear. As illustrated in Figure 1.10, deflection might occur through the film structure without fracture of the hard layers whereas the soft layers act as a shear zone since it is exposed to much more stress than the hard layers [117]. It is crucial to state that this behavior can differ in some cases, i.e. if a compressive stress greater than the yield stress of the uppermost hard layer material is applied, then deformation (fracture) of this layer can be expected. Besides that, the thickness of the layers must be also taken into account, in which thicker layers will be subject to more stress. In the opposite case (i.e. the uppermost layer is soft, and the soft and hard layers sequence), due to its low shear modulus, G (or elastic modulus, E), the uppermost soft layer cannot accommodate shear anymore and fracture can happen depending on the applied stress and the layer thickness. In the case of completely deformation of this layer, the following hard layer will manage the further process by either transferring only the shear stress to the posterior layers (when shear stress < yield stress) or receiving the shear stress and fracturing (when shear stress > yield stress).

The control of the parameters such as hardness, thickness and surface roughness of thin films [118] is of critical importance for sliding of multilayer thin films as well, since they have profound impact on the formation of the third-body at the interface. For a FCC/BCC Cu-Nb system, different deformation mechanisms have been reported by Misra et al. [119], in which glide of single dislocations confined to individual layers has been predicted for a few nm to a few tens of nm thickness, whereas piling-up of dislocations in larger layers (sub-µm to µm) has been mentioned. They have also addressed an interface crossing for smaller layer thickness (i.e. 1-2 nm). Notwithstanding that, further factors which may influence other material systems have been drawn attention [119]. On the other side, as indicated with the sliding experiments performed on the FCC/FCC material systems, i.e. Au-Cu [77], Ag-Cu and Al-Cu [78], mechanical mixing of the layers through shear instabilities has been observed. Although these results can open new horizons in the field of tribology, a comprehensive tribological analysis of this mixing behavior is unfortunately lacking. In line with this objective, in this thesis, we would like to mainly address the friction behavior of Au-Ni metallic multilayer systems with different layer thicknesses associated with their microstructure evolution.

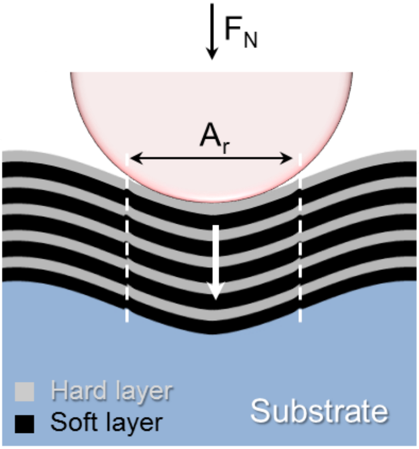

Figure 1.10: A basic illustration for a multilayer thin film system, in which the uppermost layer is harder, under the applied load, F_N, adopted from [117]. Deflection of the layers can tolerate the stress without deforming (yielding) the hard layers whereas shearing occurs in the soft layers. Applied stress, F_N is less than the yield stress of the hard layer material.

1.5 Scope of this thesis

The present study aims towards a better understanding of the dependence of friction on well-defined initial microstructures by utilizing a gold and nickel multilayer model alloy. After the introduction to the subjects initiated in this chapter, the thesis will proceed with Chapter 2 which will be a guide for the techniques utilized in the experiments and describe reasoning behind the selection of the Au-Ni material system for the tribological studies presented in this thesis. It also contains information regarding the preparation and structural characterization of Au-Ni multilayer thin films and sliding experiments. Chapter 3 will continue with results regarding the friction behavior of multilayer samples depending on the layer thicknesses under different environmental conditions as well as their microstructural evolution after sliding. A detailed discussion of the results of individual multilayer sample will be given in Chapter 4. The possible reasons of the distinctive microstructure evolution under different atmospheres will be explained and a comparison of the friction behavior with regard to the microstructure evolution will be given. Wear behavior of multilayer samples under different environments associated with the surface characteristics will be also addressed. Before finalizing the chapter, a theoretical model applied to the corresponding results observed under UHV conditions and based on the relationship between microstructure, deformation mechanism, and friction behavior will be addressed by including the limitations for our Au-Ni metallic material system. Chapter 5 will conclude the thesis by providing a summary of the results and ultimately, Chapter 6 will supply an outlook including the future research aspects.

2 Materials and Methods

2.1 Abstract

This chapter gives a detailed explanation of materials and methods which are used in this thesis. The theoretical methods section is initially provided to guide which techniques/instruments are utilized before and after, as well as during the friction experiments. Following this path, sample preparation is described by addressing why Au and Ni are selected as the main materials of the multilayer thin film structure for further tribological purposes. Subsequently, the characterization of the as-grown multilayer films in terms of crystallography, surface roughness, and indentation hardness is described. Friction tests in two different environments are reported and the microstructure evolution of the worn multilayer samples via the electron microscopy rounds this chapter out.

2.2 Principle of methods

2.2.1 Magnetron sputtering

Magnetron sputtering is the most widely used technique among physical vapor deposition (PVD) systems in order to coherently grow thin films. During this process, a magnetron target is bombarded by the highly energetic ions accelerating with the help of electric and magnetic fields applied to the ion plasma in the chamber. This destructive process provides sputtering of target atoms when they collide with the accelerated ions. The ejected atoms from the target surface accumulate on a substrate, and then condense forming a thin film [120]. A schematic representation of the process is given in Figure 2.1.

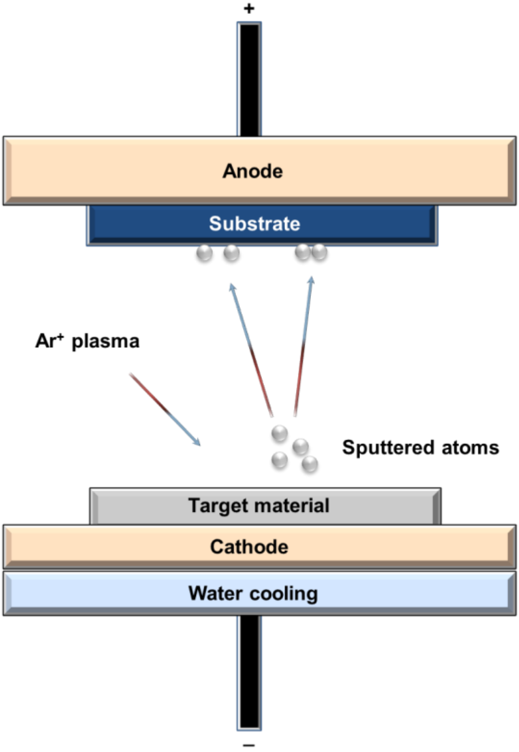

Figure 2.1: Schematic representation of magnetron sputtering process. Ar$^+$ ions are accelerated through a target material to sputter the target atoms. The ejected atoms from the target accumulate on the surface of the substrate, and then they condense forming thin film.

The name ‘magnetron’ stems from the construction of magnets surrounding the target material, which also increase the probability of an electron-atom collision during the ion bombardment. This step is of use to improve the efficiency of ionization for denser plasma in the target region; and hence, the bombardment of the target is increased leading higher sputter rates to the substrate. In addition, ejecting secondary electrons from the target surface also contributes to maintain the plasma [120].

Magnetron sputtering process was utilized in this thesis to coherently grow the Au-Ni multilayer thin films for further friction experiments.

2.2.2 X-ray diffraction (XRD)

XRD is a technique where an incident beam of monochromatic (single-wavelength) x-rays and a crystalline sample construct an interference to produce reinforced diffraction peaks in order to identify the crystallographic planes since the distance between the atomic planes in crystalline solid materials can be precisely determined by the wavelengths of x-rays (Figure 2.2) [121].

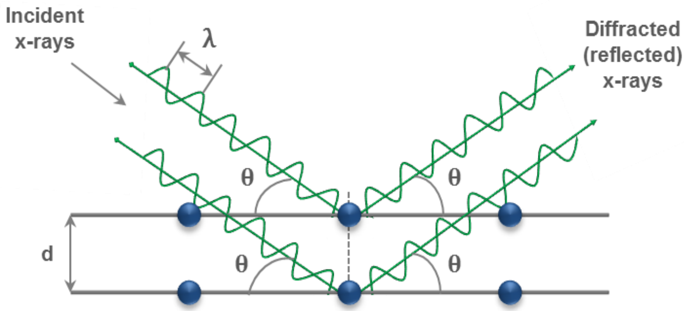

Figure 2.2: Illustration of the diffraction of an incident x-ray beam by the (*hkl*) planes of a crystal at the Bragg angle, θ, adopted from [121]. When the incident beam of monochromatic x-rays of wavelength, λ hit these planes and the reflected (diffracted) x-rays become in phase, the beam would be reinforced and consequently constructive interference takes place.

As shown in Figure 2.2, constructive interference only occurs when the conditions meet Bragg's Law during the diffraction of x-rays. This law is fundamentally related with the wavelength, λ and the diffraction angle of the electromagnetic radiation, θ and with the interplanar spacing of the crystal planes of Miller indices (*hkl*). Then, Bragg's Law [122] must be:

$$n\,\lambda = 2\,d_{hkl}\,\sin\theta \tag{2.1}$$

where n is called the order of the diffraction and in most cases, the first order of diffraction (n = 1) is used. In order to interpret the XRD data of the cubic unit cells, the interplanar spacing of the crystal planes, d_{hkl} must be calculated:

$$d_{hkl} = \frac{a}{\sqrt{h^2+k^2+l^2}} \tag{2.2}$$

By using Equation 2.2, it can be determined if a cubic unit cell is body-centered (BCC) or face-centered (FCC). For the simple cubic lattice structure, the diffraction of all (*hkl*) planes is possible whereas there are some simple rules for the diffraction of BCC and FCC crystal structures [121]. XRD analysis has been performed for the study presented in this thesis to identify the crystallographic feature of the as-grown Au-Ni multilayers.

2.2.3 Atomic force microscope (AFM)

Contact mode is the most fundamental operation mode of the AFM. In this mode, a nanometer-scale, single-asperity tip situated at the end of a flexible, micro-machined cantilever scans over a sample surface. During scanning, the sample is mounted to a piezoelectric tube (the piezo scanner) and the normal (vertical) interaction force acting between the tip and the sample is detected by recording the position of a laser beam deflected off the backside of the cantilever on a photodiode corresponding to the vertical deflection of the cantilever due to the interaction [123]. The general schematic associated with a typical AFM setup is given in Figure 2.

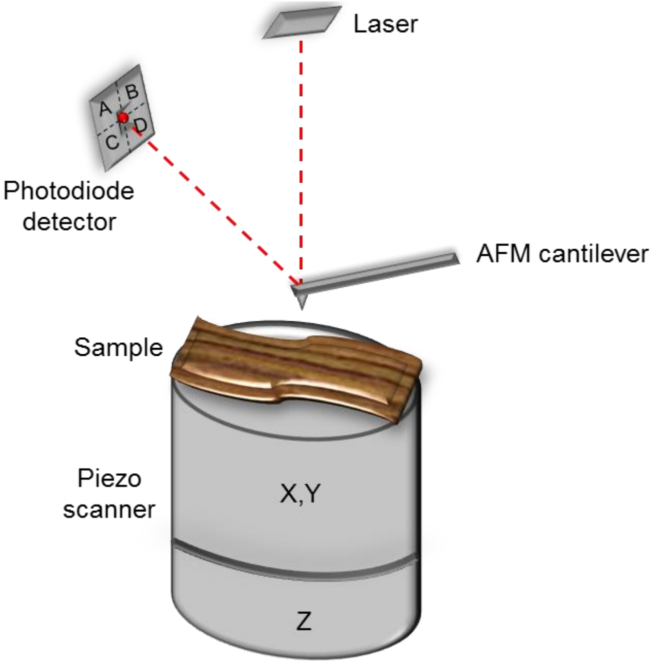
Laser
A
B
C
D
Photodiode detector
AFM cantilever
Sample
Piezo scanner
X,Y
Z

Figure 2.3: A basic illustration of a general AFM concept. The sample is mounted to a piezoelectric tube (the piezo scanner) and a nanometer-scale, single-asperity tip situated at the end of a flexible, micro-machined cantilever scans over the sample surface. The deflection of the cantilever in the vertical direction is detected by a four-quadrant photodiode. Topographical maps are acquired by keeping the normal force constant during scanning via a feedback loop and tracking the z-position of the piezo scanner.

The AFM tip and the sample can be moved with respect to each other, in three (x, y, z) directions and their displacements are converted from applied voltages into actual lengths by the piezoelectric constants. By keeping the normal force constant during scanning via a feedback loop and tracking the z-position of the piezo scanner, topographical maps are acquired. The normal force between the AFM tip and the sample surface can be detected by the amount of cantilever deflection [124].

In contrast of its general concept as already explained, some AFMs can be worked differently. A Bruker AFM (Veeco Dimension V), which was utilized in contact mode in order to topographically characterize the uppermost surfaces of the Au-Ni multilayer samples in this thesis, is of such an example. As displayed in Figure 2.4, instead of the sample, the AFM cantilever is placed onto the cylindrical piezoelectric scanner mounted near the top of the microscope in this latter case, and constant deflection of the AFM cantilever can be maintained by the feedback loop. To keep the cantilever deflection constant, the piezo scanner uses height data which corresponds changes in the deflection (voltage) signal between the top (A, B) and the bottom (C, D) segments of the four quadrant photodiode. By recording the output fluctuations from the photodiode (when the tip and cantilever are deflected due to the features on the surface of the sample), the accurate topographical data can be constituted. In addition to this, the feedback gains must be as high as possible in order to collect the height data by minimizing the cantilever deflection during scanning.

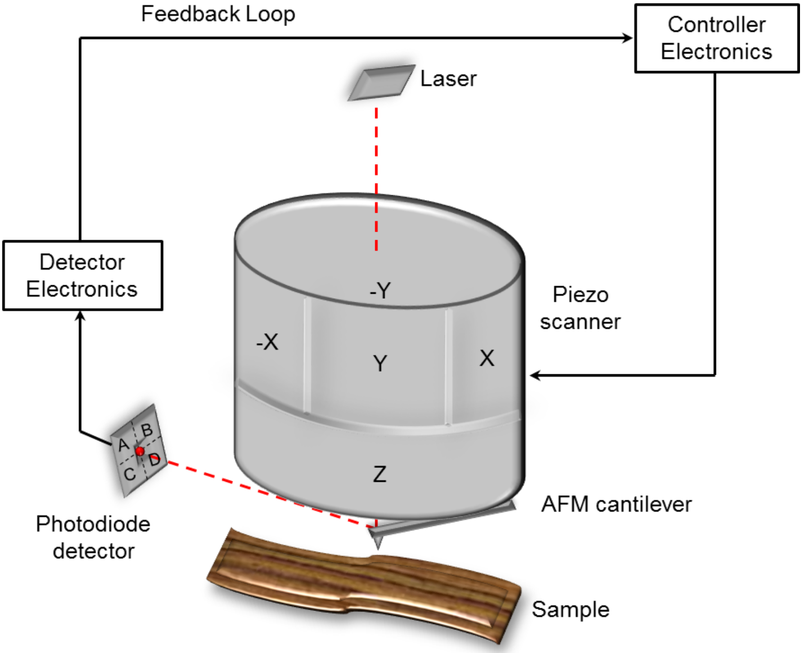
Feedback Loop
Controller Electronics
Laser
Detector Electronics
-Y
-X
Y
X
Piezo scanner
Z
A
B
C
D
AFM cantilever
Photodiode detector
Sample

Figure 2.4: Schematic illustration of a Bruker AFM (Veeco Dimension V). The AFM cantilever (within the cantilever holder) is placed onto the cylindrical piezo scanner mounted near the top of the microscope (the piezo scanner must be mounted downward to provide the accurate position for the AFM tip to scan). Constant deflection of the AFM cantilever can be maintained by the feedback loop of the system.

2.2.4 Nanoindentation

Nanoindentation is the most commonly used technique to determine the mechanical properties of materials in small scales for decades, and a nanoindenter is frequently utilized to obtain elastic modulus and hardness of the material from a ‘load-displacement’ curve [125].

During nanoindentation measurements, indents with specific depths and sizes are constituted by an indenter tip on the material surface, and the mechanical applied load as well as the displacement of the indenter is controlled by means of the sensors and special actuators. Mechanical applied load leads to adjust the displacement of the indenter (the depth of penetration) originating plastic deformation (can be referred as indent) on the sample surface, and the size of the contact area for this specified load can be calculated via the known geometry of the indent (indenter). Once the area of contact is determined, indentation hardness, H can be obtained by dividing the applied load, P by this projected area, A [126] as follows:

$$H = \frac{P}{A} \tag{2.3}$$

In addition, recording the applied load and the corresponding penetration depth (load-displacement curve) from zero to maximum load and vice versa during the measurement provides estimation for elastic modulus of the material. When the applied load is released, the material presumes to return its original shape; however, it would never occur since it is plastically deformed. Notwithstanding that, the recovery process would proceed by the relaxations of elastic strains in the material; and hence, elastic modulus of the material would be estimated by the slope of this relaxation (elastic unloading). Since a Berkovich type indenter does provide more precise control for the process due to its sharper tip, it is preferred in most indentation experiments and, the relationship between the load and the displacement for the elastic-plastic contact in this case would then be [125]:

$$\mathrm{h} = \sqrt{P}\left[\left(3\sqrt{3}\,H\,\tan^2\theta\right)^{-\frac{1}{2}} + \left(\frac{2\,(\pi-2)}{\pi}\right)\frac{\sqrt{H\pi}}{2\,\beta\,E_{\mathrm{i}}}\right] \tag{2.4}$$

where h refers the depth of penetration, $\theta = 65.27°$, E_i is the indentation modulus and β indicates the scaling factor ($\beta = 1.034$ for a Berkovich indenter [126]). Hardness of the as-grown multilayer samples has been measured via nanoindentation prior to friction tests.

2.2.5 X-ray photoelectron spectroscopy (XPS)

XPS (also known as electron spectroscopy for chemical analysis (ESCA)) is one of the most commonly used tools to analyze surfaces since it can accurately determine chemical states of the elements with their quantities on near surfaces of materials. By using a raster-scanned micro focused x-ray beam of the PHI5000 Versaprobe II XPS (Physical Electronic GmbH) which is utilized in this thesis (shown in Figure 2.5a), spatial distribution is provided and sample surface is excited with mono-energetic Al K_α x-rays. As a result of this process, photoelectrons are ejected from the sample surface. To evaluate the energy of ejected photoelectrons, an energy analyzer is utilized (see Figure 2.5a).

As illustrated in Figure 2.5b, an electron is ejected when an atom or a molecule absorbs an x-ray photon. Depending on the photon energy ($h\,v$) and the binding energy (BE) of this ejected electron, its kinetic energy (KE) can be determined by the Equation 2.5 [127]:

$$KE = h\,v - BE - \emptyset_{sp} \tag{2.5}$$

where h is Planck's constant, v is the photon's frequency and $\emptyset_{sp}$ is the work function of the spectrometer. This determination is crucial because the kinetic energy can reveal the present elements in the near surface with their chemical states and binding energies.

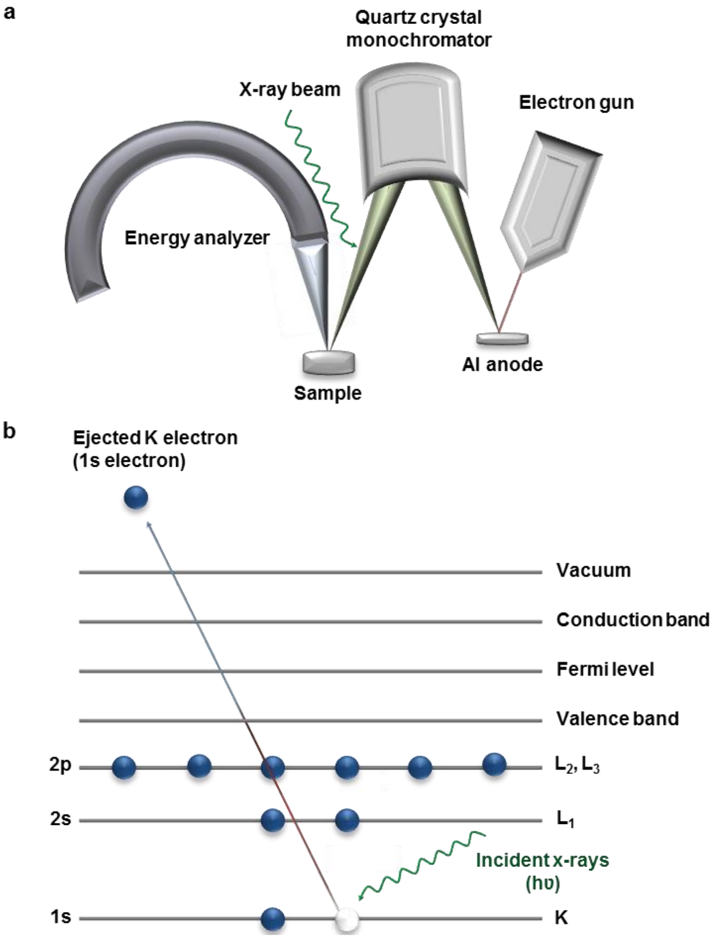
a
Quartz crystal monochromator
X-ray beam
Electron gun
Energy analyzer
Al anode
Sample
b
Ejected K electron
(1s electron)
Vacuum
Conduction band
Fermi level
Valence band
2p
L_2, L_3
2s
L_1
Incident x-rays
(hʋ)
1s
K

Figure 2.5: Schematic illustrations for the XPS. (a) A basic diagram of the PHI5000 Versaprobe II XPS (Physical Electronic GmbH); (b) Photoemission process for K 1s energy level during a XPS analysis. When an atom or a molecule absorbs an x-ray photon, an electron is ejected from the surface. Depending on the photon energy ($h\,v$) and the binding energy (BE) of this ejected electron, its kinetic energy (KE) can be determined ($KE = h\,v - BE - \emptyset_{sp}$).

Furthermore, there is a significant point worth to consider for the quality of the peaks in the XPS spectrum, which is generated by inelastically scattered electrons during analysis. These electrons cause a background in the spectrum by reducing the kinetic energy of the ejected electrons as well as intensities in their peak formats. Therefore, background must be eliminated prior to the quantification of the XPS spectrum.

From the point of this thesis, surface cleaning of the multilayer samples has been provided prior to each friction test via Ar ion sputtering in the XPS chamber.

2.2.6 UHV microtribometer

First friction experiments presented in this thesis were performed via a microtribometer operating in ultrahigh vacuum (10^{-7} Pa) which is achieved through the instrument of a 150 l/s Titan Ion Pump (Gamma Vacuum). A schematic diagram of the UHV microtribometer components is presented in Figure 2.6a. This UHV chamber is connected to the introduction load lock of the PHI5000 Versaprobe XPS system which is previously explained, but it is not shown in the figure. Accordingly, the design of the tribometer stage is compatible with PHI sample holders as depicted in Figure 2.6b; and thus, the sample can be moved from the microtribometer to the XPS system without being exposed to air. In order to provide this combination, the piezo actuator of the tribometer is placed on a shelf that can be moved up and down (z-direction) by 35 mm to bring the sample near the counter-body (a sphere in the corresponding experiments) attached to the cantilever. During measurements, the piezo actuator is free to move in three dimensions (x, y, z) with a range of 110 µm on each axis, which can be managed either manually or by software [128].

Technically, the force sensor of the microtribometer is predicated on a conception of double leaf spring cantilevers (Figure 2.6c) which is very well explained by Scherge et al. [129]. Unlike AFM cantilevers, the cantilevers specially designed for our tribometer do not show friction forces generated by torsional (twisting) motion since it is suppressed; only lateral deflections can be recorded to accentuate friction forces. In addition to this, bending in vertical direction induced by normal stress is also minimized. This described configuration of the cantilever makes essential using laser interferometers as well as mirrors (Figure 2.6b) in order to detect the displacement of the cantilever during reciprocating sliding (the movement in y direction is indicated in Figure 2.6c). It should be noted that only a reference mirror is illustrated in the figure; however, there exist two mirrors (one horizontal and one vertical). Differently from the single beam laser interferometer used in vertical direction, a double laser interferometer is equipped in horizontal direction to reduce measured noise signals also coming from mechanical deformations and thermal oscillations. Thus, the setup of the interferometer or the alignment of the laser is very important. In order to provide the accurate operating parameters, a sensor head is used by readjusting the drive parameters of its piezoelectric vibrator. To obtain highly accurate result for each measurement time, the frequency and the amplitude of the signals on the analog-signal channels of the oscilloscope must be improved, and a figure close to the 'Lissajous figure' [130] as displayed on the left hand side in Figure 2.7 must be reached. Once this adjustment is achieved, measurement can be started; otherwise, it is not possible to vertically apply and/or laterally record any forces until the laser, which is out of alignment, is aligned (on the right hand side, Figure 2.7) [128].

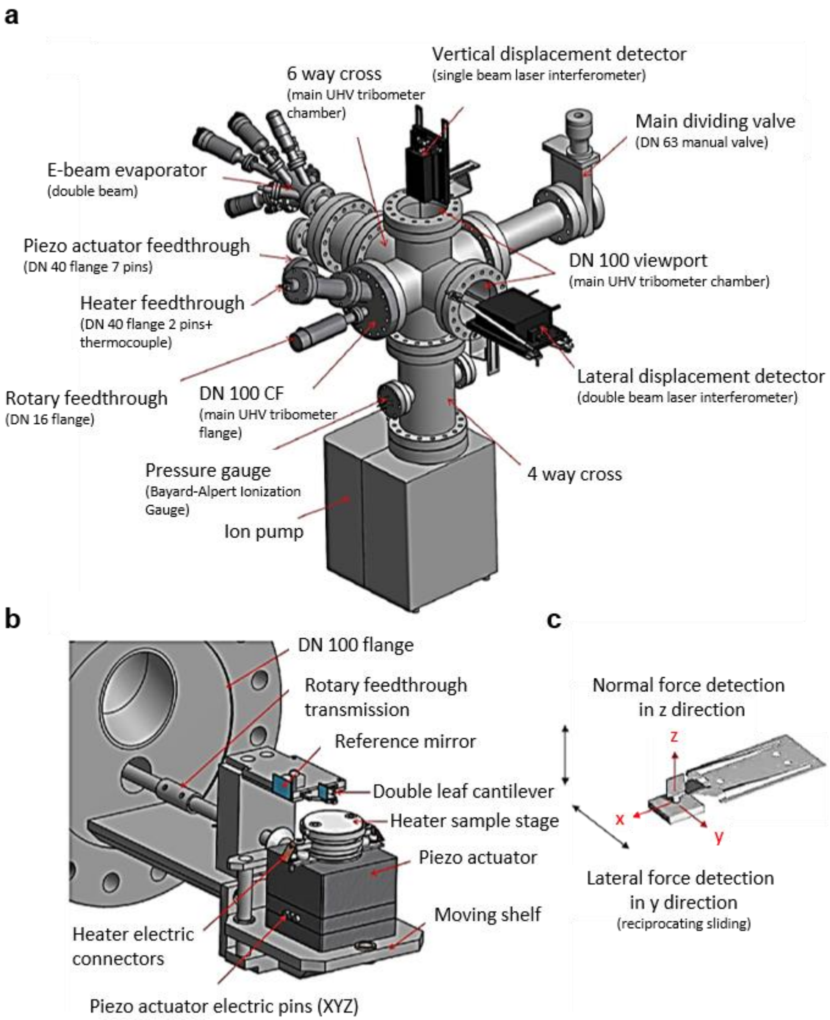
a
6 way cross
(main UHV tribometer chamber)
Vertical displacement detector
(single beam laser interferometer)
Main dividing valve
(DN 63 manual valve)
E-beam evaporator
(double beam)
Piezo actuator feedthrough
(DN 40 flange 7 pins)
DN 100 viewport
(main UHV tribometer chamber)
Heater feedthrough
(DN 40 flange 2 pins+ thermocouple)
Lateral displacement detector
(double beam laser interferometer)
Rotary feedthrough
(DN 16 flange)
DN 100 CF
(main UHV tribometer flange)
Pressure gauge
(Bayard-Alpert Ionization Gauge)
4 way cross
Ion pump
b
DN 100 flange
Rotary feedthrough transmission
Reference mirror
Double leaf cantilever
Heater sample stage
Piezo actuator
Moving shelf
Heater electric connectors
Piezo actuator electric pins (XYZ)
c
Normal force detection in z direction
z
x
y
Lateral force detection in y direction
(reciprocating sliding)

Figure 2.6: Schematic diagram of the UHV microtribometer components (which are shown in the previous page) [128]. (a) The tribometer chamber is equipped with an e-beam evaporator for deposition of metallic thin layers. The instrument is also connected to

an XPS system which is not shown here; (b) Schematic diagram of the microtribometer setup with the components; (c) Schematic diagram of the cantilever with the directional indicators for the detection of normal and lateral forces in the z and y directions, respectively.

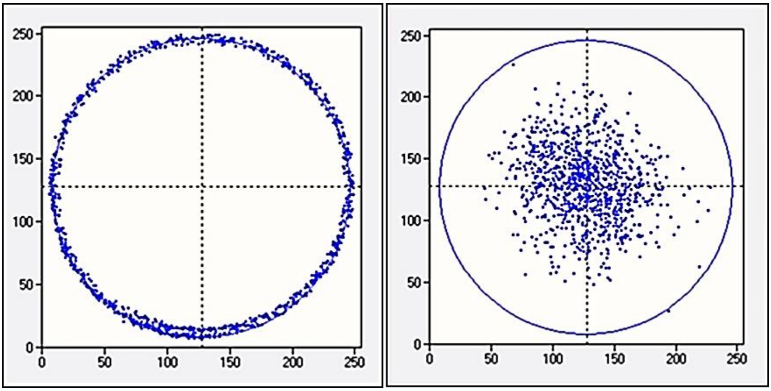

Figure 2.7: Oscilloscope windows showing the laser adjustment process [128]. (left) The figure close to the 'Lissajous figure' [130] on the x-y trace of the analog signals on the oscilloscope, for an optimal adjustment of the vibrator with automatic gain control (laser is aligned); (right) the case for the laser beam which is out of alignment. An oscilloscope basically displays how the electrical signals (input voltages) change over time, and the voltages are referred on the x-y axes in these figures. Lissajous figure indicates that the phase difference between multiple input signals is eliminated by aligning the laser in the latter case.

2.2.7 Microtribometer utilized in nitrogen (N_2) atmosphere

A microtribometer (Sandia National Laboratories, Albuquerque, NM, USA) which is purged with dry N_2 having < 10 ppm O_2 and < 40 ppm H_2O, was utilized for the friction experiments at ambient temperature. This tribometer also makes use of a two axis double leaf spring cantilever and orthogonal capacitance probes measure the cantilever displacement by means of its deflection in two independent axes, where the torsional motion might be assumed negligible [87]. A photograph of the tribometer is depicted in Figure 2.8.

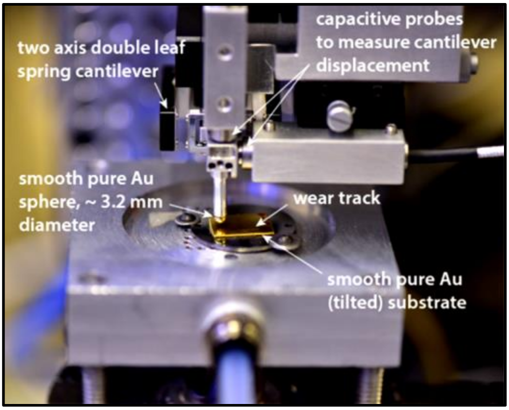
two axis double leaf spring cantilever
capacitive probes to measure cantilever displacement
smooth pure Au sphere, ~ 3.2 mm diameter
wear track
smooth pure Au (tilted) substrate

Figure 2.8: Picture of the tribometer of interest showing a sliding experiment between a smooth pure Au ball and a pure Au substrate [87]. The tribometer relies on a system within two axis double leaf spring cantilever and orthogonal capacitance probes measure the cantilever displacement by means of its deflection in two independent axes. Reprinted by permission from Springer Nature: Journal of Materials Science, 52, Linking microstructural evolution and macro-scale friction behavior in metals, 2780-2799, N. Argibay et al, Copyright (2016).

2.2.8 Focused ion beam (FIB) / scanning electron microscope (SEM)

Focused ion beam (FIB) technique has been widely used to prepare thin lamellas for the transmission electron microscope (TEM) analysis for more than two decades. It is a destructive tool where material is sputtered (milled) from the sample surface by emitting secondary ions (i+, i-) or neutral atoms

(n) in virtue of the bombardment of highly energetic (5–50 keV) gallium (Ga) ions [131]. In addition to that, secondary electrons (e^-) are also generated during this process via the inelastic scattering of the electron beam. A basic principle of Ga ion milling is illustrated in Figure 2.9 in which milled area marked with dashed line can be seen. So, by collecting signals coming from the emitted secondary electrons and ions by means of special detectors while scanning the sample surface, images can be created in two different imaging modes.

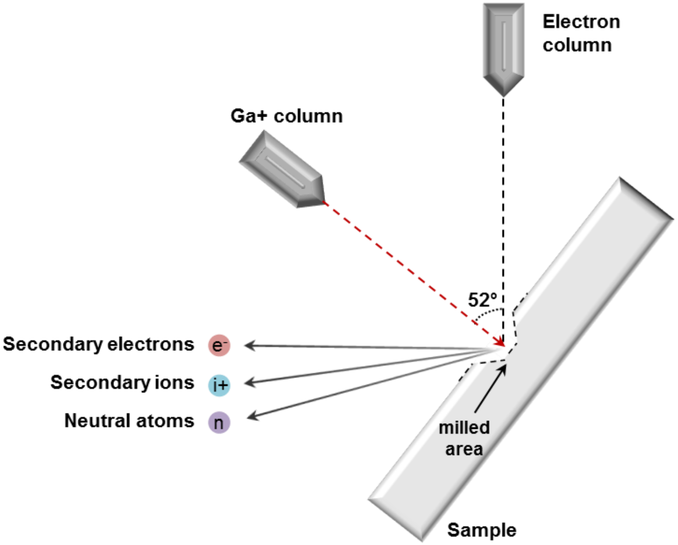

Figure 2.9: A basic illustration of the principle of gallium (Ga) ion milling (sputtering) via the focused ion beam (FIB) instrument. When highly energetic (5–50 keV) Ga ions strikes the sample surface, a sum of material is sputtered by emitting secondary ions (i+, i-) or neutral atoms (n). Secondary electrons (e^-) are also generated and images can be formed by collecting signals coming from these electrons or ions while scanning the sample surface.

2.2.9 Transmission electron microscope (TEM) / energy dispersive x-ray spectroscopy (EDXS) / high resolution (HR)TEM

In a TEM, the electron beam is focused into an ultra-thin specimen (lamella) by a condenser lens, and electrons are highly accelerated by an electron gun using electromagnetic coils and high voltages. Accelerated electrons are then transmitted through the specimen; and by the interaction of these electrons with the electrons emitted from the specimen surface, images are created on a fluorescent screen by means of an objective coil (magnetic lens) [132].

The image contrast is formed directly by diffraction and absorption of the electrons. For instance a bright field (BF) objective aperture is placed in the back focal plane of the objective lens and allows collecting electrons directly from the beam (Figure 2.10a). According to the interaction between these electrons and electrons emitted from the sample, thicker regions and/or heavy atoms appear with dark contrast since mass and thickness are the main contributors to the image formation. On the other hand, due to its settlement in the diffraction plane which is illustrated in Figure 2.10b, a dark field (DF) objective aperture usually blocks collecting these electrons while coherently diffracted (Bragg scattered) electrons are allowed to pass by the objective aperture. DF imaging is therefore assumed more useful to study planar defects and dislocations in the sample. In addition to this, a high-annular angle dark field (HAADF) objective aperture helps collecting incoherently diffracted electrons (to the contrary of coherently diffracted-Bragg scattered electrons in conventional DF) to provide images within more efficiency in many cases.

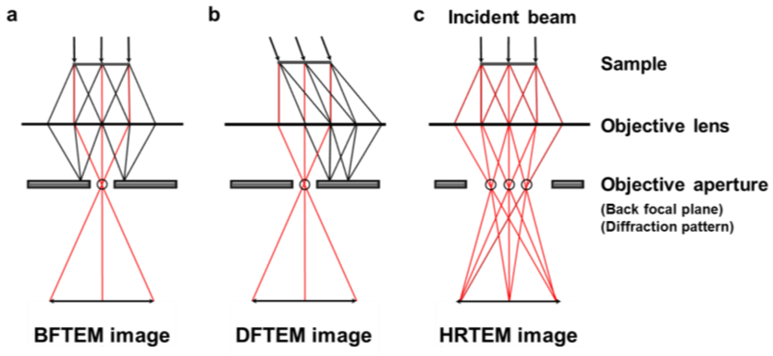

Figure 2.10 Basic illustrations of the imaging modes in TEM. (a) BF objective aperture is placed in the back focal plane of the objective lens and allows collecting electrons directly from the beam; (b) DF objective aperture is settled in the diffraction plane and coherently diffracted (Bragg scattered) electrons are collected by this aperture; (c) the objective aperture in HRTEM provides an enlarged image of the crystal pattern by the interference between all the diffracted beams and the primary incident beam.

HRTEM generally refers to observing crystallographic planes by achieving atomic resolution during imaging, due to the multi-beam approach. The objective aperture provides an enlarged image of the lattice structure by the interference between all the diffracted beams and the primary incident beam (Figure 2.10c) [132].

The basic theory of the XPS can be considered to explain the main principle of the EDXS. Notwithstanding that, these two techniques differentiate from each other in terms of the determination of the kinetic energy at the end of the process. The kinetic energy of the ejected electrons is determined in XPS [127], whereas the kinetic energy of the characteristic x-rays is the major parameter for the chemical analysis during an EDXS, since characteristic x-rays are released due to the energy decrement when the high level electron drops to the lower energy state and creates an electron hole subsequent to the collision of the electron in the first excitation stage. This principle was simply illustrated in Figure 2.11.

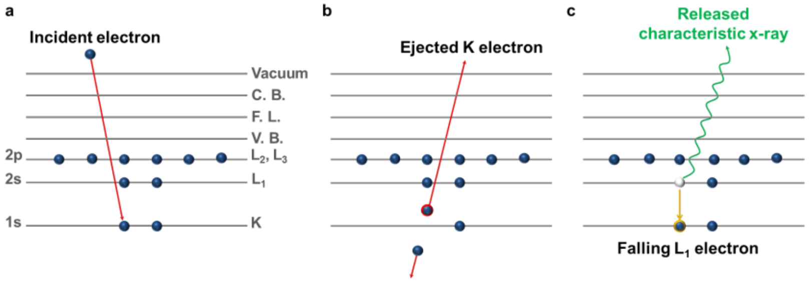

Figure 2.11: A basic illustration of the EDXS principle. (a) A highly energetic electron strikes another electron in the lower energy state (K); (b) and forces it to be ejected from the atom; (c) then, a characteristic x-ray is released due to the drop of the energy in the higher state (L_1) when its electron falls toward the lower energy state (K) and creates an electron hole in L_1.

2.2.10 Transmission Kikuchi diffraction (TKD)

TKD can be used as a mapping technique to mainly characterize the nanocrystalline and/or ultra-fine grain materials with a higher spatial resolution when it is compared to the conventional electron backscattered diffraction (EBSD) technique, where the materials with (sub-) micron grains are of the interest [133]. The main difference between TKD and EBSD is that the sample must be thin (similar to the situation of an electron transparent TEM lamella prepared via FIB-lift-out technique [131]) in the TKD case, and mounted to the proper sample holder, which is pre-tilted towards 70°, in an appropriate way (i.e. positioned horizontally or back-tilted as shown in Figure 2.12) away from the EBSD detector to provide the suitable diffraction patterns from the corresponding sample surface in an improved spatial resolution with a shorter working distance.

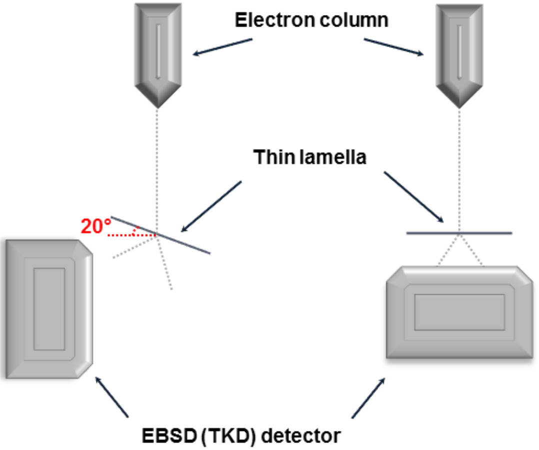

Figure 2.12: A typical experimental configuration for TKD analysis. The sample (thin TEM lamella) is mounted to the proper sample holder, which is pre-tilted towards 70°, in an appropriate way away from the EBSD (TKD) detector either backtilted towards 20° as illustrated on the left, or positioned horizontally as indicated by the right-handed figure.

An accelerating voltage of 30 kV is typically applied during measurements whereas it can be lowered down to 15 kV to enhance the diffraction intensity of ultra-thin samples and/or low atomic number materials. To decide on a suitable region for TKD patterns, thickness and density contrast of the SEM images could have a significant impact. DF images are thereof collected by a detector system where the diodes near to the screen can ensure good quality images within the enhanced contrast. And, when the contrast effect of thickness and density is mitigated by inverting one of the diode signals, orientation contrast of the image would be more dominant to reveal the functional microstructure for the TKD analysis [133].

2.3 Materials

2.3.1 Selection of materials: gold and nickel

Gold (chemical name Au, derived from the Latin name aurum) has been known since prehistoric times and was one of the first metals to be worked [134]. It is a transition metal and is located in the 6th period and 11th group of the periodic table with the atomic number of 79. Under standard conditions, Au is a solid, yellow-colored metal with the highest ductility and malleability among all other metals. It crystallizes in the face-centered cubic (FCC) lattice structure with a lattice parameter of 4.08 Å. The pure Au metal melts at 1064.18 °C and its atomic weight is 196.967 with a density of 19.32 g/cm^3 at 20 °C. Au has elastic modulus, E of 78 GPa, shear modulus, G of 27 GPa, and yield strength of 205 MPa. Also, Au is one of the most inert metals and does not oxidize under a wide range of conditions due to the fact that it retains its crystalline structure in a very large size range and exhibits high chemical stability [135].

The element of nickel (chemical name Ni) was discovered by Axel Fredrik Cronstedt [136] in 1751 and the name of this silvery-white metal was shortened from the German “kupfernickel” which might mean devil's copper or St. Nicholas's copper [137]. It is located in the 4th period and 10th group of the periodic table with the atomic number of 28. Ni crystallizes in the FCClattice structure with a lattice parameter of 3.52 Å. The pure Ni metal melts at 1455 °C and its atomic weight is 58.693 with a density of 8.9 g/cm^3 at 20 °C. Ni has elastic modulus, E of 200 GPa, shear modulus, G of 76 GPa, and yield strength of 480 MPa. Nickel highly resists corrosion and can be therefore used to coat other metals to protect them; nevertheless, it is also common to use Ni in alloying purposes. Compared to Au, Ni is stiffer, and has high hardness alongside of being ductile.

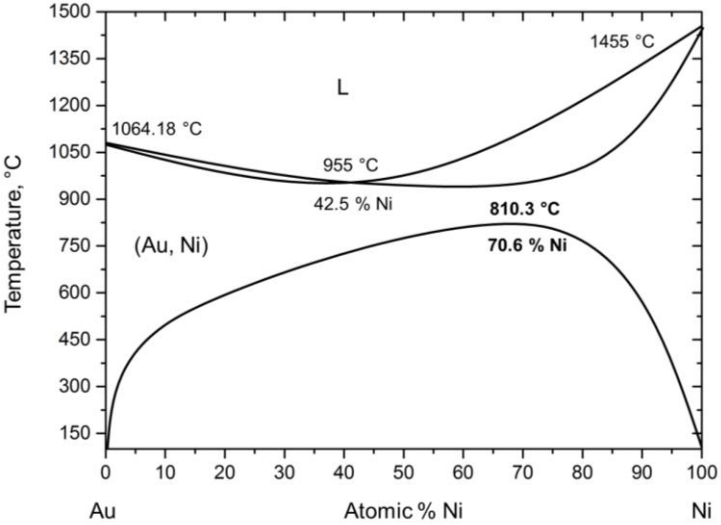

Figure 2.13: Equilibrium binary phase diagram for Au-Ni material system, adopted from [138]. As equilibrium phases, FCC continuous solid solutions are seen at low temperatures where the critical point of the miscibility gap is around 810.3 °C (1083 K) at 70.6 at.% Ni. At higher temperatures, equilibrium phases transform liquid, L, with a minimum freezing point of 955 °C at 42.5 at.% Ni.

According to the binary phase diagram of Au-Ni material system [138] in Figure 2.13 a miscibility gap can only exist at higher temperatures (above a critical temperature, 810.3 °C) because of the fact that in order for two metals to form a solid solution, they must crystallize in the same lattice structure and have similar chemical properties. Hence, the miscibility gap at lower temperatures (below 810.3 °C) leads to the decomposition, and the Au-Ni solid solution separates into two FCC structural phases below the critical temperature [139]. In other words, these metals do not create an alloy structure under normal circumstances and a separation gap is formed. Thus, the immiscibility nature of Au-Ni system at lower temperatures (below 810.3 °C) leads for these materials to exhibit an appropriate pair to be initially preparing as separable layers to examine the influence of microstructure on friction.

2.3.2 Preparation and structural characterization of Au-Ni multilayers

2.3.2.1 Growth of multilayers

Due to the possibility of non-mixed preparation, the Au-Ni material system was chosen for tribological studies explained later in this chapter. In order to coherently grow multilayer thin films (denser and better adhesion), a magnetron sputtering process was utilized. For this purpose, Si wafers (100) were initially cleaned with surfactant and acetone in an ultrasonic bath for 2 hours. Prior to thin film deposition, plasma etching was applied inside the physical vapor deposition (PVD) chamber (Leybold Z550) for 2 minutes to clean and activate the wafer surface at an atmosphere of 0.5 Pa Ar in 6N purity and a power of 500 W. Growth of Ni and Au layers with well-defined microstructures on Si substrates took place via magnetron sputtering at 0.4 Pa Ar in 6N purity atmosphere, and sputtering conditions for both Ni and Au layers are summarized in Table 2.1.

The individual interlayer spacing of the samples was 10 nm, 20 nm, 50 nm, 100 nm, respectively and the number of layers was changed from 100 to 10 thus fixing total film thickness at 1 µm. The topmost layer was chosen such that is Au layer in order to prevent the structure from possible oxidation whereas the nethermost layer is Ni in each multilayer sample. The HAADF scanning transmission electron microscope (STEM) images shown in Figure 2.14 provide a survey for the cross-sectional view of the as-grown Au-Ni multilayer samples subsequent to the sample preparation (details of the process will be explained later). Starting from a layer thickness of 10 nm, a waviness of the layers is seen in between Au and Ni layers due to residual strains possibly induced by the lattice mismatch between these metals which is about 15 %, as well as orientation dependent growth rate. At increasing layer thickness, this phenomenon of misfit softens as it can be clearly seen from following images in Figure 2.14.

Table 2.1 Sputtering conditions for Ni and Au layers

Spacing (nm)	Sputter time (s) 300 W HF, Ni	Sputter time (s) 20 W DC, Au
100	142	163
50	71	82
20	28	33
10	14	16

STEM analysis of the as-grown Au-Ni multilayers also proved the immiscible nature of Au and Ni metals in terms of making an alloy (mechanically mixing) structure in general procedure, in line with main purpose of using this material-pair in order to study the influence of microstructural changes on friction.

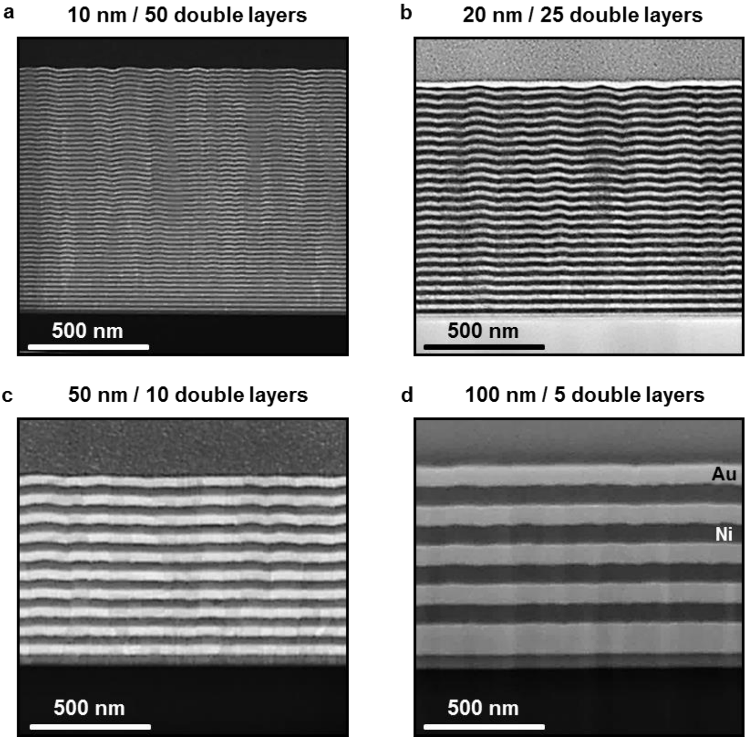
a
10 nm / 50 double layers
500 nm
b
20 nm / 25 double layers
500 nm
c
50 nm / 10 double layers
500 nm
d
100 nm / 5 double layers
Au
Ni
500 nm

Figure 2.14: HAADF STEM cross-sectional views of the as-grown Au-Ni multilayers for an interlayer spacing of 10 nm (a), 20 nm (b), 50 nm (c) and 100 nm (d), respectively.

2.3.2.2 Crystallographic identification via XRD

XRD measurements were carried out using CuK$_{\alpha 1/2}$ radiation in Bragg-Brentano geometry at a Seifert PAD II diffractometer equipped with a Meteor 1D detector. The profiles of individual Au-Ni multilayer samples are given in Figure 2.15. In all measurements, the diffraction peaks (111), (200) and (222) of Au were present as principal peaks. There were no reflections from the Ni layers since Ni(111) and Au(200) reflections have almost the same diffraction angle. An increment in the width of the peaks was also noticeable as the number of double layers increases (or the interlayer spacing decreases). This indicates the lower grain size with decreasing layer thickness, according to the approximation with Scherrer equation [140]:

$$\Delta(2\theta) = \frac{K\lambda}{L\cos\theta} \tag{2.6}$$

where L is the mean size of the ordered (crystalline) domains (grain size), K is a dimensionless shape factor - the Scherrer constant, λ is the x-ray wavelength, $\Delta(2\theta)$ is the line broadening at full width at half maximum (FWHM) intensity, and θ is the Bragg angle.

By using Eq. 2.6, grain sizes of each Au-Ni multilayer samples were calculated in terms of the XRD data. The initial grain size of Au(111) and Ni(111) layers are listed in Table 2.2, in which the calculated grain sizes of the layers for the cases of 20 nm, 50 nm and 100 nm samples are reliable whereas the calculated values for the 10 nm sample are slightly larger than the layer thickness which can be plausible if the possibly present crystal defects are taken into account.

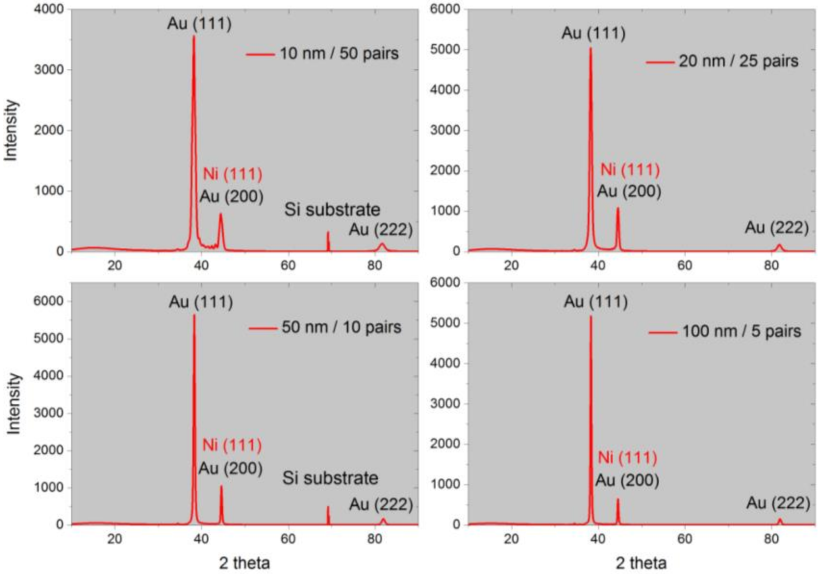

Figure 2.15: XRD profiles of individual Au-Ni multilayer samples. The diffraction peaks (111), (200) and (222) of Au are present as principal peaks and there seem no reflections from the Ni layers since Ni (111) and Au (200) reflections have almost the same diffraction angle. The broadening of the peaks is noticeable as the number of double layers increases, which also indicates the lower grain size with decreasing layer thickness.

Table 2.2 Grain size approximation via the XRD data

Au(111)

Spacing (nm)	Measured broadening at FWHM	Instrumentation broadening	Line broadening (MB - IB)	Scherrer constant, K	X-ray wavelength, λ (Å)	Bragg angle, 2θ	Grain size (nm)
10	0.8204°	0.07°	0.7504°	0.89	1.54056	38.3°	11.08
20	0.575°	0.07°	0.505°	0.89	1.54056	38.3°	16.47
50	0.3571°	0.07°	0.2871°	0.89	1.54056	38.3°	28.97
100	0.2406°	0.07°	0.1706°	0.89	1.54056	38.3°	48.75

Ni(111)

Spacing (nm)	Measured broadening at FWHM	Instrumentation broadening	Line broadening (MB - IB)	Scherrer constant, K	X-ray wavelength, λ (Å)	Bragg angle, 2θ	Grain size (nm)
10	0.8273°	0.07°	0.7573°	0.89	1.54056	44.5°	11.22
20	0.4855°	0.07°	0.4155°	0.89	1.54056	44.5°	20.43
50	0.2771°	0.07°	0.2071°	0.89	1.54056	44.5°	40.99
100	0.2280°	0.07°	0.158°	0.89	1.54056	44.5°	53.71

2.3.2.3 Roughness analysis via AFM

A Bruker AFM (Veeco Dimension V), was utilized in contact mode in order to topographically characterize the uppermost surfaces of the Au-Ni multilayer samples. A Si AFM cantilever (Budget sensors uncoated Tap300 series) with a nominal radius of curvature less than 10 nm, a resonant frequency of 300 kHz and a spring constant of 40 N/m, which is appropriate for intermittent contact mode (also calibrated with respect to the force-distance curve obtained over the surface of a Si calibration grating), is used during measurements applying a lower interaction force. The corresponding roughness profiles of each multilayer samples are given in Figure 2.16, in which ‘very slightly’ raising roughness has been observed with increasing interlayer spacing.

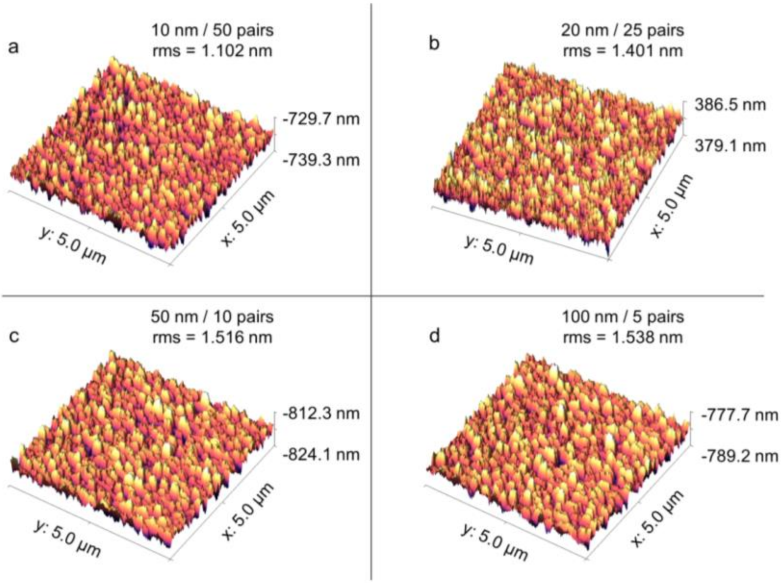
a
10 nm / 50 pairs
rms = 1.102 nm
-729.7 nm
-739.3 nm
y: 5.0 µm
x: 5.0 µm
b
20 nm / 25 pairs
rms = 1.401 nm
386.5 nm
379.1 nm
y: 5.0 µm
x: 5.0 µm
c
50 nm / 10 pairs
rms = 1.516 nm
-812.3 nm
-824.1 nm
y: 5.0 µm
x: 5.0 µm
d
100 nm / 5 pairs
rms = 1.538 nm
-777.7 nm
-789.2 nm
y: 5.0 µm
x: 5.0 µm

Figure 2.16: AFM topography analysis of the topmost layers of Au-Ni multilayers. Root mean square (rms) roughness values are (a) 1.102 nm for 10 nm-multilayer sample; (b) 1.401 nm for 20 nm-multilayer sample; (c) 1.516 nm for 50 nm-multilayer sample; (d) 1.538 nm for 100 nm-multilayer sample.

2.3.2.4 Nanoindentation hardness measurements

A ‘Hysitron Ti 950 Triboindenter’ (Bruker) was utilized to measure the indentation hardness of the as-grown Au-Ni multilayer samples, via the indentation load-displacement curves (see Appendix Figure A1). A standard, diamond, Berkovich type indenter was used in the measurements and different indentation loads from 2 to 8 mN, which were calibrated according to the load-displacement curves of the standard fused quartz sample, were applied to the multilayer samples. Although the determination of the critical indentation depth for each multilayer sample is a quite big challenge because of the fact that the critical depth value of each sample varies due to the different number of layers as well as different layer thickness having distinct chemistry and hardness, hardness of the multilayer samples from the corresponding nanoindentation measurements at 8 nN are indicated within the plot shown in Figure 2.17.

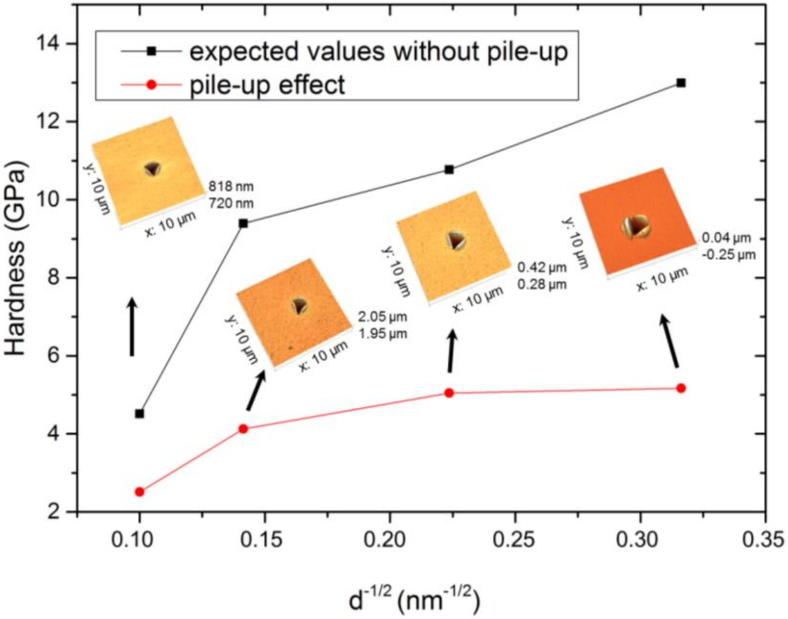

Figure 2.17: Nanoindentation measurements on Au-Ni multilayer samples. Indentation hardness as a function of the interlayer spacing of the multilayers at 8 mN applied load. An increase in the layer thickness leads to decrease in hardness of the multilayers by 58.3±7%, from 10 to 100 nm sample (without pile-up), which is in agreement with the Hall-Petch relationship. Note however that significant amount of pile-up has been observed in our measurements. Hence, in order to eliminate the pile-up effect and correct the hardness of multilayer samples, a simple geometrical approach is used based on the determination of the area of the triangle indent [142].

Although the maximum penetration depth is of importance to avoid the substrate effect during nanoindentation tests of thin film samples, and huge amount of pile-up has been observed in our measurements, it can be highlighted that the hardness of all Au-Ni multilayer samples at an applied load of 8 mN increases with decreasing the interlayer spacing, which would also denote the smaller-sized of grains in thinner multilayer samples and is in line with the Hall-Petch relationship where the increase in the number of layers (interfaces) per unit volume would lead to the increase in hardness due to the accumulation of dislocations at the boundaries (since the dislocation motion is blocked by the presence of additional interfaces). These results are in agreement with the previous observations by Jankowski [141] where he argued that hardness of the metallic multilayer samples depends on the layer thickness in relation to the biaxial modulus of the layers which is affected by the indentation depth.

In order to eliminate the pile-up effect and correct the hardness of multilayer samples, a simple geometrical approach is used based on the determination of the area of the triangle indent [142]:

$$A_{\mathrm{triangle}} = \frac{\sqrt{3}}{4}\mathrm{a}^2 \tag{2.7}$$

$$A_{\mathrm{pile\text{-}up}} = 3\left(\frac{\pi R^2}{6} - \frac{\sqrt{3}}{4}\mathrm{a}^2 \right) \tag{2.8}$$

2.4 Friction tests and characterization of worn Au-Ni multilayers

2.4.1 Friction tests under UHV conditions

Friction tests on Au-Ni multilayer structures were run via the UHV microtribometer (Figure 2.6) under the base pressure of 10^{-7} Pa. An inert ruby sphere with the diameter of 3 mm was slid on the surfaces of Au-Ni multilayers at a constant normal load of 1 mN and a constant sliding velocity of 33 µm/s, and experimental setup of interest is presented in Figure 2.18. The cantilever (calibrated normal and tangential spring constants; k_N = 800 mN/mm, k_T = 1320 mN/mm, respectively) was fixed while the sample was being scanned with the help of the piezo actuator, and the displacement of the cantilever was measured by means of the interferometers both horizontally and vertically. Cantilever deflections in the horizontal direction led obtaining friction force signals which were recorded during originating wear track (plastic deformation) on a sliding distance of 100 µm within a reciprocating motion for 100 cycles.

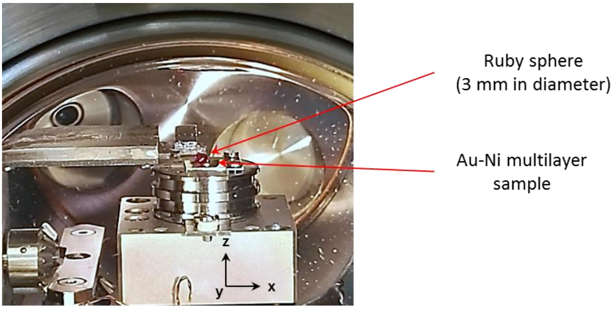

Figure 2.18: Picture of the experimental setup used in the friction tests. Note that the reciprocating sliding was always applied in the y direction while the sample was positioned in the x direction.

2.4.1.1 Cleaning the sample surface prior to the friction tests, via Ar sputtering

XPS analysis (PHI5000 Versaprobe II as shown in Figure 2.5a) was applied to the topmost surfaces of each Au-Ni multilayer samples when introduced into the UHV chamber, right before the friction tests in order to provide a clean surface. Figure 2.19a represents a corresponded overview of the topmost surface in which presence of the Au element was again confirmed (it has already been proved by the XRD) while peaks of carbon (C) and oxygen (O_2), which come from air, were marked in yellow. In this sense, it was necessary to apply Ar ion sputtering for the removal of these undesirable elements. Thus, the Ar ion beam was rastered over the area of interest of 5×5 mm^2 on the topmost surface of the sample for approximately 0.5 min (which would be equivalent an amount of less than 1 nm of the top surface) by accelerating with the voltage of 2 kV in the XPS chamber. As shown in Figure 2.19b, C and O_2 were removed from the topmost surface by the ion bombardment; and hence, surface cleaning was able to be achieved prior to the friction test. Once surface cleaning was provided, the sample was directly transferred from the XPS chamber to the microtribometer.

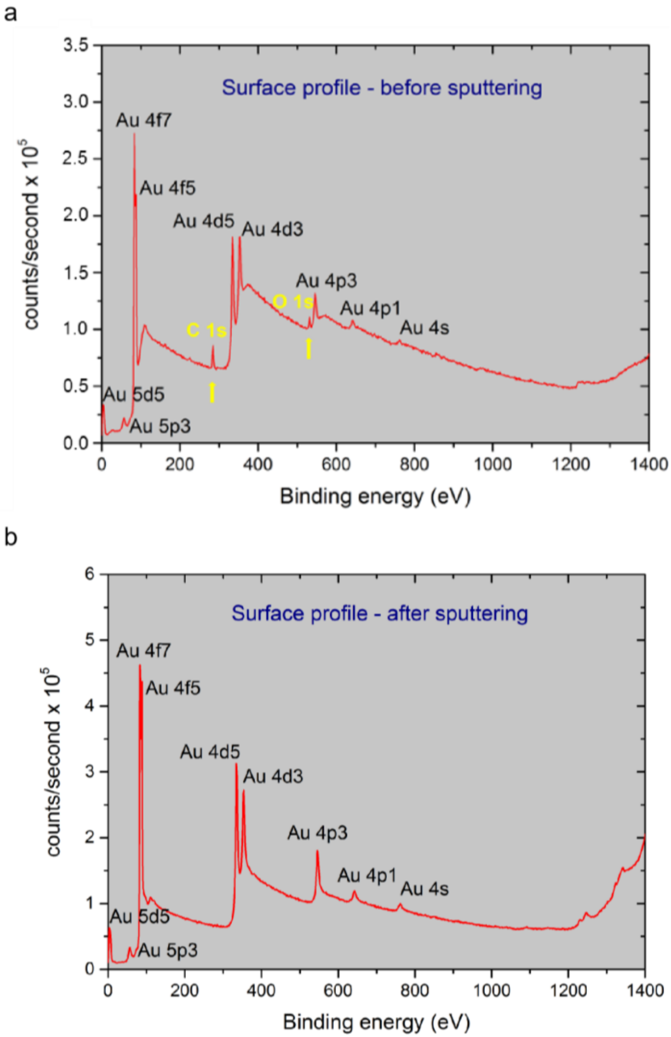

Figure 2.19: Uppermost surface profiles of Au-Ni multilayer samples using XPS. (a) C and O_2 peaks are present on the topmost surface when Au-Ni multilayer sample is introduced into the XPS chamber from air; (b) C and O_2 are removed from the topmost surface by Ar ion milling (sputtering), which means that surface cleaning can be achieved prior to the friction test in the UHV microtribometer.

2.4.2 Friction tests under N_2 atmosphere

These experiments were carried out at Sandia National Laboratories, Albuquerque, NM, USA, as part of the "Research Travel Grant" supported by KIT's KHYS between the dates of 1st of May-31th of July, 2018. With intent to compare frictional and microstructural results obtained by the UHV microtribometer, which is described in the previous section, supplemental experiments in a different atmospheric condition were decided to be performed. In line with this purpose, a microtribometer placed in a glove box (already shown in Figure 2.8) was utilized for the experiments in controlled humidity and ambient temperature, and friction experiments were run in 'less than 10 ppm H_2O' environment (i.e. pressure < 1 Pa). The relative humidity varied in the range of 10-20% and the temperature was 20 +/- 1 ºC. As in previously mentioned UHV experiments, 1 mN normal force was applied with a piezo positioner on a ruby sphere (3.2 mm in diameter) during sliding on Au-Ni multilayer samples within a velocity of 33 µm/s for 100 reciprocating cycles.

2.4.3 Post-sliding microstructure observation of Au-Ni multilayers

2.4.3.1 TEM lamella preparation via FIB/SEM

Cross-sectional Au-Ni multilayer samples were prepared parallel (y-z plane in Figure 2.18) and perpendicular to the sliding direction via FIB milling using a FEI Helios NanoLab DualBeam 650 (now ThermoFisher). Before preparing a cross-section of the sample, the interested area on the wear track was coated with two platinum (Pt) layers to be protected by ion beam damage arising from the high energy of Ga ions. The first Pt layer was deposited via the electron beam with a thickness of 0.2-0.3 µm at an acceleration voltage of 2 kV and a beam current of 6.4 nA, whereas the second Pt layer was deposited by the ion beam with a thickness of 1-1.5 µm at an acceleration voltage of 30 kV and a beam current of 0.77 nA (or 0.43 nA when needed). Also, in order to be able to study with the FIB instrument, the sample stage was already tilted towards 52°. Subsequently, cross-sectional rectangles were cut with the beam current of 45 nA from both sides of the Pt protected layer, following by the cleaning process of these cross-sections with a lower beam current of 9.4 nA by tilting the stage for 50.5° and 53.5°. In the meantime, an acceleration voltage of 2 kV and a beam current of 0.8 nA were used to take cross- sectional SEM images (by collecting secondary electron signals) in order to watch the whole process.

Following this process, common procedures for in-situ lift-out technique [131] were applied to prepare the TEM lamellas. Figure 2.20 shows a FIB image recorded at the last stage right before lifting-out the lamella. The lamella is still connected to the main sample from the region indicated with red rectangle after being Pt-welded to the omniprobe, and will be ready to be lifted-out after cutting the last connected region (red area). Then the next step will be thinning process of the lamella for upcoming TEM imaging.

As presented with the FIB images in Figure 2.21, thinning process takes place in 3 steps with different tilt angles, and beam currents which must be reduced in every step to more avoid beam damages because of the cross-sectional area getting smaller. And not displayed step in Figure 2.21 is the last cleaning process of the lamella to remove all the residuals before the TEM analysis, with an acceleration voltage of 5 kV and a beam current of 43 pA at a tilt angle of 57° (frontside) and 47° (backside). Once the lamella was present for the

TEM analysis, first images were tried to be taken via a STEM detector installed on the FIB/SEM system with an acceleration voltage of 30 kV and a beam current of 0.2 nA, as can be exemplified with the as-grown Au-Ni multilayer samples displaying in Figure 2.14.

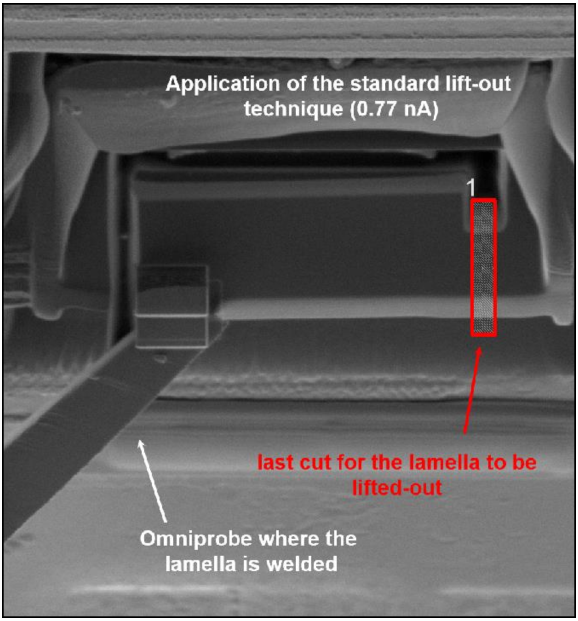
Application of the standard lift-out technique (0.77 nA)
1
last cut for the lamella to be lifted-out
Omniprobe where the lamella is welded

Figure 2.20: FIB image prior to the process of lifting-out. The lamella is still connected to the main sample from the region indicated with red rectangle after being Pt-welded to the OmniProbe, and will be ready to be lifted-out after cutting this red area.

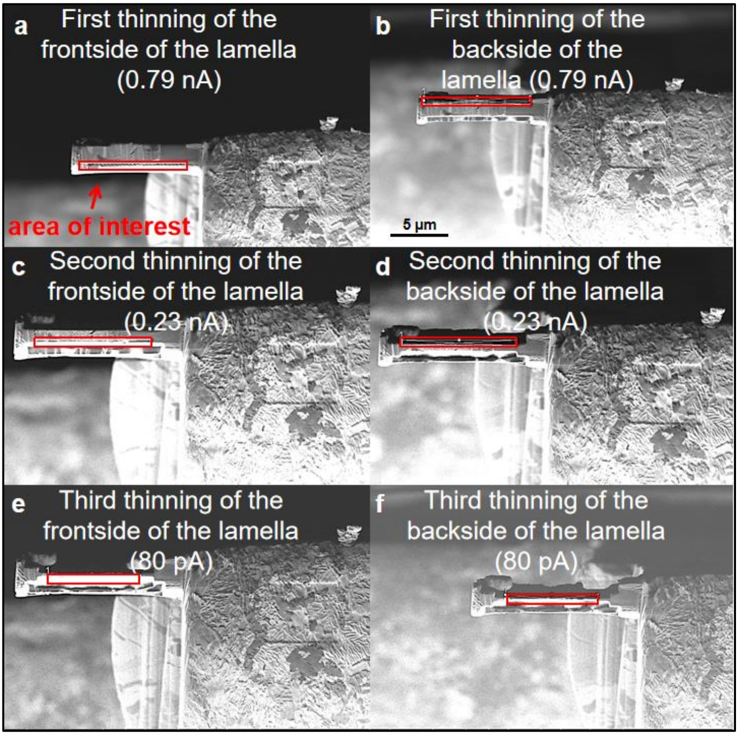
a
First thinning of the frontside of the lamella (0.79 nA)
area of interest
b
First thinning of the backside of the lamella (0.79 nA)
5 µm
c
Second thinning of the frontside of the lamella (0.23 nA)
d
Second thinning of the backside of the lamella (0.23 nA)
e
Third thinning of the frontside of the lamella (80 pA)
f
Third thinning of the backside of the lamella (80 pA)

Figure 2.21: FIB images taken while the process of thinning is in progress in 3 steps with different tilt angles and beam currents. Process for (a) the first thinning of the frontside of the TEM lamella with a beam current of 0.79 nA at a tilt angle of 53.5°; (b) the first thinning of the backside of the TEM lamella with a beam current of 0.79 nA at a tilt angle of 50.5°; (c) the second thinning of the frontside of the TEM lamella with a beam current of 0.23 nA at a tilt angle of 53.5°; (d) the second thinning of the backside of the TEM lamella with a beam current of 0.23 nA at a tilt angle of 50.5°; (e) the third thinning of the frontside of the TEM lamella with a beam current of 80 pA at a tilt angle of 53.2°; (f) the third thinning of the backside of the TEM lamella with a beam current of 80 pA at a tilt angle of 50.8°, respectively.

2.4.3.2 Microstructure evolution via TEM/HRTEM

TEM in (S)TEM mode in combination with the EDXS analysis were performed to investigate the sub-surface chemistry of Au-Ni multilayer samples after sliding under UHV conditions by using a FEI Osiris ChemiSTEM, with an acceleration voltage of 200 kV (this combination is definitely an advantage for an EDXS map to be concurrently recorded on a preselected area while scanning). (S)TEM (FEI Titan ChemiSTEM, operated at 200 kV) imaging in combination with the EDXS analyses were also performed on the multilayer samples worn under N_2 atmosphere. Images were obtained in BF, DF and HAADF modes by providing different contrasts.

In order to further analyze the microstructure of Au-Ni multilayer samples worn under UHV with atomic resolution, HRTEM analysis was applied via a Philips CM200 FEG/ST operated at an acceleration voltage of 200 kV. Selected area electron diffraction (SAD) aperture was also utilized to examine the crystal orientations in sub-surfaces, due to the diffraction patterns of electrons representing the periodic potential of the surface atoms [132]. For multilayer samples worn under N_2 atmosphere, TEM and HRTEM analyses were done utilizing a FEI Tecnai F30, operated at 300 kV.

2.4.3.3 Microstructure evolution via TKD

TKD measurement on the cross-sectional area of the 100 nm sample with high spatial resolution was performed by using a Bruker Quantax e^{-} Flash^{HD} EBSD detector in the FIB/SEM DualBeam microscope. The lamella was prepared using a lift-out technique [131] similar to that of TEM sample preparation, and it was placed to a special sample holder with a pre-tilt angle of -20° (Figure

2.12, on the left), as already explained in 2.1.10. In order to adjust the position of the Kikuchi diffraction patterns towards the center of the phosphorous screen of the EBSD detector, the working distance was set to 2 mm. The step size was selected 4 nm for the measurement to achieve the sufficient spatial resolution from the structure, and the EBSD (TKD) detector was tilted to 9°. An acceleration voltage of 30 kV and a beam current of 6.4 nA were applied during scanning the surface on the cross-sectional area of $1.3 \times 1.6\ \mu m^2$.

3 Results

3.1 Abstract

This chapter includes the experimental results obtained in this thesis study. The friction behavior of individual Au-Ni metallic multilayer system for 100 reciprocating cycles of sliding is initially given in both UHV conditions and N_2 environment. Their microstructural evolution via the electron microscopy is then explained in detail. Prior to concluding the chapter, 1000 cycles-friction tests are also addressed for the 10 nm and 100 nm multilayer systems, containing the microscopic structural observation.

3.2 Friction behavior of individual metallic multilayer system

3.2.1 Friction behavior under UHV conditions

Based on the fact that alloys are omnipresent in technical applications (i.e. transportation and machinery) in which friction and wear are made responsible for the energy losses, it is of high importance that the tribological characteristics of related material systems are quantified in detail. In line with this purpose, a comprehensive and systematic experimental study on Au-Ni multilayer model alloy which has been described in Chapter 2 is carried out and detailed tribological analysis is made.

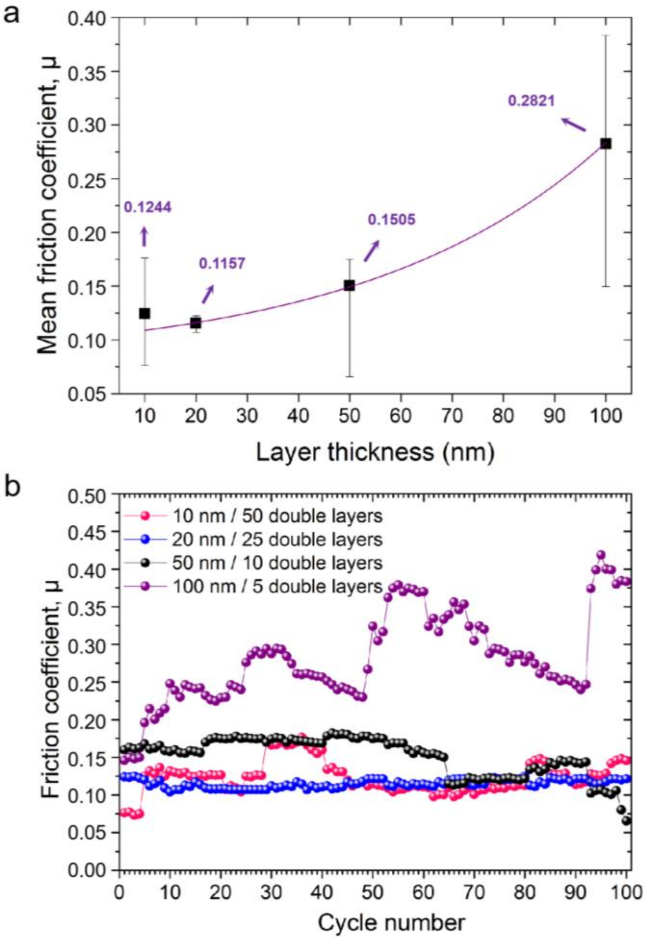

Figure 3.1: Friction behavior of Au-Ni multilayers. (a) Mean friction coefficient values of the multilayer systems for 100 reciprocating cycles as a function of layer thickness. A significant increase of the COF with increasing layer thickness is remarkable. The solid line is an exponential fit between the data points. Error bars are determined by the fluctuations in friction behavior during sliding over time as depicted in (b) with different stability. Note that the lines in (b) are for eye guidance only.

Subsequent to the friction tests via UHV mictrotribometer, different friction behavior is observed for individual Au-Ni multilayer sample exposed to the same sliding parameters. Figure 3.1a shows the mean friction coefficient values of the multilayer systems for 100 reciprocating cycles as a function of layer thickness where a significant increase of the coefficient of friction (COF) with increasing layer thickness is found.

Similar values of the COF, i.e. 0.1244 (±0.05) and 0.1157 (+0.0068, -0.086) are observed for the 10 nm and 20 nm samples, respectively. Slightly higher COF is achieved for the 50 nm sample with a value of 0.1505 (+0.0245, -0.085), while the highest friction behavior is seen in the thickest multilayer sample (μ = 0.2821±0.1) at the end of sliding. Divergent error bars are evaluated for each multilayer sample as indicated in Figure 3.1a, due to the different stability of the friction behavior during sliding over time as depicted in Figure 3.1b. This behavior will be associated to the microstructure evolution of individual multilayer sample later in this chapter.

3.2.2 Friction behavior under N_2 atmosphere

A change in the environment during experiments may lead to different friction behavior for the multilayer samples due to the presence of additional gases/vapors and even liquid molecules in an aqueous media depending on the chosen environment. In order to investigate the effect of ambient conditions on friction and wear, sliding experiments in a controlled N_2 atmosphere were carried out with the multilayer structures with the same experimental parameters such as counter body, velocity and applied load. And consequently, it has started with a higher friction force compared to the on-going behavior while reduced COF values are observed as the number of sliding cycles is increased.

The behavior of the friction of the Au-Ni multilayer samples studied for 100 reciprocating cycles is presented in Figure 3.2, in which different friction stability (for the stable normal force of 1 mN) over time can be recognized. The behavior of friction for the last 20 cycles of sliding is also demonstrated and explicitly more stable friction has been observed for each multilayer sample at last cycles in comparison with the overall.

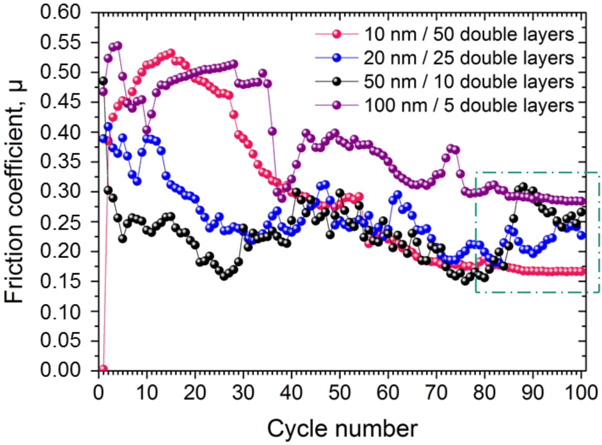

Figure 3.2: Friction behavior of Au-Ni multilayers. Different frictional stability is found throughout sliding for 100 reciprocating cycles. For all tribological systems the friction coefficient drops after the first few cycles. The COF decreases gradually for the system with 10 nm layer spacing while for others, the friction decreases suddenly. The 20 and 50 nm layer spacings still showed rather unstable friction behavior towards the end of the experiment, whereas for the other systems stable friction has been observed within the last 20 cycles in comparison with the overall. Note that the data point at zero COF (of the 10 nm multilayer sample) is a software-induced artifact and the lines in figures are for eye guidance only.

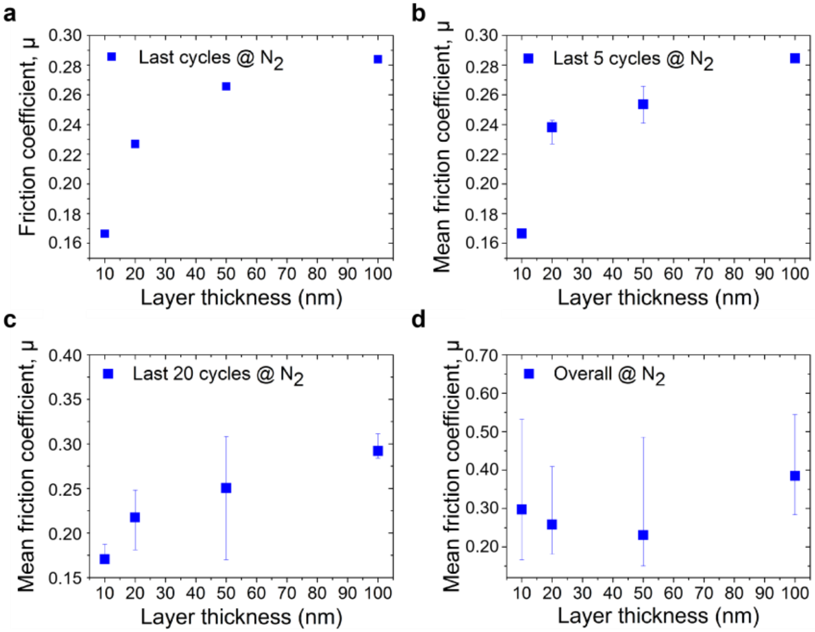

Figure 3.3: COF values of Au-Ni multilayers under N_2 atmosphere. (a) A significant increase of the COF with increasing layer thickness is remarkable at the last cycle. (b-c) The COF increases with increasing layer thickness at the last 5 and 20 cycles. (d) The trend for increasing COF with increasing layer thickness is completely distorted for 100 reciprocating cycles. Error bars are determined by the maximum and minimum records in friction during sliding over time as depicted in Figure 3.2.

As shown in Figure 3.3a the COF at the last cycle increases with increasing layer thickness. This trend is also observed when the COF is evaluated over the last 5 cycles (see Figure 3.3b), and the last 20 cycles with a slight difference in the COF values due to the fluctuations during sliding (see Figure 3.3c) mentioned before. When the mean friction coefficient values for 100 reciprocating cycles are calculated, it is found that no clear trend of the COF as function of the layer thickness can be evaluated (see Figure 3.3d) due to the unstable friction behavior (see Figure 3.2a).

Therefore, it is important to note that the relationship between the COF and the layer thickness up to the last 20 cycles would be reasonable since relatively stable friction behavior is observed in the latter cases. Beyond all question, the COF values of each multilayer sample are larger than the ones observed under UHV conditions; except the 100 nm sample for the last sliding cycles (up to the last 20 cycles), which is fairly similar for both cases.

3.3 Microstructure characterization of individual metallic multilayer system subsequent to the friction tests for 100 cycles

3.3.1 Microstructure characterization under UHV conditions

In order to analyze the microstructure of worn/deformed Au-Ni multilayers after friction tests and to realize a comparison with results for the as-grown multilayers, cross-sectional imaging by FIB milling has been utilized parallel to the sliding direction (y-z plane in Figure 2.18) as previously explained in detail. Micrographs of each Au-Ni multilayer system exposed to reciprocating sliding for 100 cycles under UHV conditions are shown in Figure 3.4. A new, completely structureless layer between Au and Ni layers of the 10 nm and 20 nm samples (corresponding to the lowest observed friction forces) are found that was not present before the sliding experiment. On the other hand, a very disordered Au rich structure is visible when increasing the layer thickness of the multilayer system to 50 nm. When further increasing the layer thickness (100 nm), rather than a new structure just the thinning of the uppermost Au layer is seen by plowing and accumulating some Au at the end of the wear track.

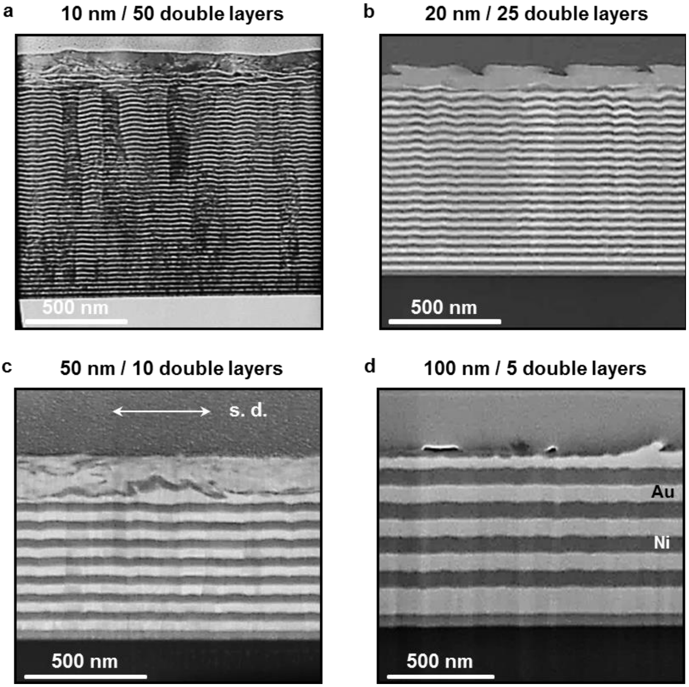
a
10 nm / 50 double layers
500 nm
b
20 nm / 25 double layers
500 nm
c
50 nm / 10 double layers
s. d.
500 nm
d
100 nm / 5 double layers
Au
Ni
500 nm

Figure 3.4: Characterization of the worn Au-Ni multilayers. HAADF STEM cross-sections of the worn Au-Ni multilayers for an individual layer thickness of (a) 10 nm; (b) 20 nm; (c) 50 nm; (d) 100 nm after sliding for 100 reciprocating cycles. The sliding process concludes with mixing (a-c), and the pile-up (only the uppermost Au-layer is influenced) (d), respectively. All cross-sections were prepared parallel to the sliding direction (y-z plane in Figure 2.18).

3.3.1.1 Cross-sectional (S)TEM analysis via TEM

(S)TEM imaging, operated in both the BF and the HAADF mode, in combination with the EDXS analyses have been performed on the multilayer samples to analyze the worn structures and investigate the sub-surface chemistry. The results of the 10 nm sample are presented in Figure 3.5.

It is observed that the first 8 layers are plastically deformed and possess a shear-induced or “mixed” microstructure while the remaining 92 layers are still unmixed. A reduction in the thickness of the upper layers, which are adjacent to the deformed, intermixed region, is visible and at the very surface, a zone is also found, where individual Au and Ni structures are not distinguishable in the STEM. The lower bound of the intermixing tribolayer, which is drawn right before these visible layers, is indicated with the red dashed line in Figure 3.5a. The region of 10-15 nm marked by the white dashed lines in Figure 3.5a-b depicts the ultrafine Ni grains which settle at the very outermost surface of the intermixing tribolayer (also in line with the EDXS map for Ni which will be presented in Figure 3.6). For the first 40 nm above, a zone is identified where individual Au and Ni structures are not distinguishable in the (S)TEM (see Figure 3.5b-c). Below, a zone which consists of mixed fragments of the former layers is also found. Thus, the thickness of the intermixing tribolayer varies from 40 nm to 100 nm for these cases.

As one can see in the micrographs in Figure 3.6, the presence of two zones becomes more obvious; as such inseparable layers on the first 40 nm from the surface, and a zone containing mixed fragments of the former layers starting from 40 nm up to 100 nm. The quantitative EDXS maps on the right-hand side in Figure 3.6 represent the atomic concentration of Ni (Figure 3.6a) and Au (Figure 3.6b) of the corresponding (S)TEM cross-section images on the left-hand side. By shearing, a mixed structure consisting of 60-65 at% of Ni in Au is obtained. Also, the more favorable place for ultrafine Ni grains can be recognized from white arrows in Ni map of Figure 3.6a, which completes the findings already shown in Figure 3.5a-b.

Figure 3.7 gives the detailed structural analysis for the multilayer system with the layer thickness of 20 nm. While already observed that mixing is possible between Au and Ni phases through shearing (the case for the 10 nm sample), Figure 3.7 also supports this assumption as found by performing both BF and HAADF (S)TEM cross-section imaging on the 20 nm multilayer sample after sliding. In this case, the first 7 layers are mixed from which 4 are Au and 3 are Ni while the remaining 93 layers are still unaffected. And beyond, (probably) adhesion-induced structures around 45 nm in height are homogeneously formed during sliding/mixing (see Figure 3.7a-b; however no residual material on the counter surface (ruby ball) is found according to the XPS analysis. For further information the reader can see Appendix Figure A2), and the mixing behavior is followed up to 120 nm from the surface. Therefore, the thickness of the mixed layer varies from 45 nm to 120 nm which also means that the thickness of the intermixing tribolayer increases slightly with increasing layer thickness of the multilayer system when the 10 nm sample is considered. Upper and lower bounds of the intermixing tribolayer are indicated with the red dashed lines in Figure 3.7c-d. The close-up BF (S)TEM image in Figure 3.7c especially discloses the refined grains on the intermixing tribolayer.

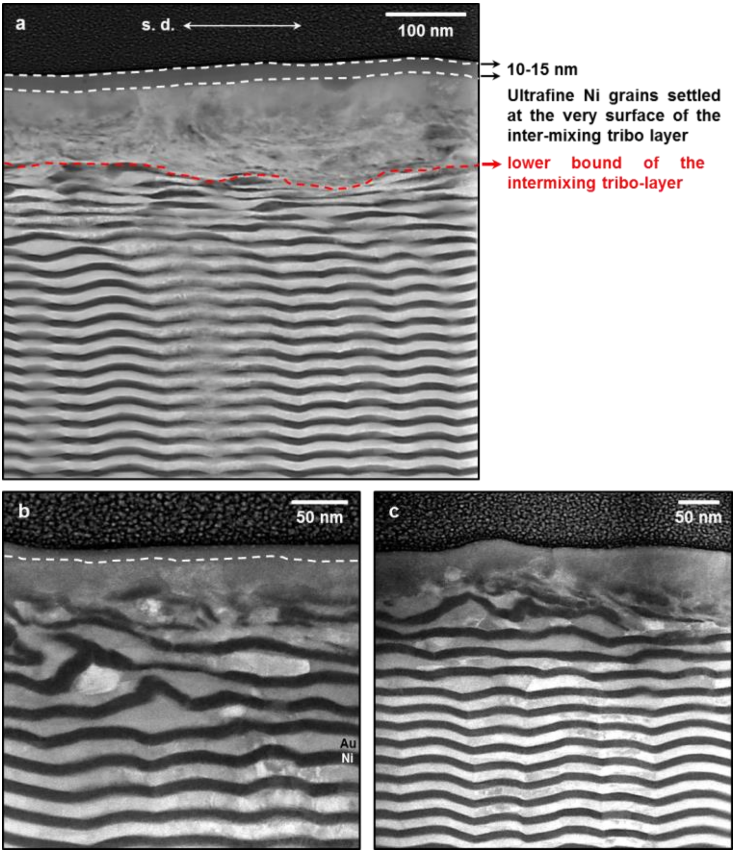
a
s. d.
100 nm
10-15 nm
Ultrafine Ni grains settled at the very surface of the inter-mixing tribo layer
lower bound of the intermixing tribo-layer
b
50 nm
Au
Ni
c
50 nm

Figure 3.5: Characterization of Au-Ni multilayers with the layer thickness of 10 nm on the intermixed tribolayer subsequent to the friction test under UHV conditions. (a) HAADF (S)TEM cross-section of the worn 10 nm multilayer sample where the lower bound of the intermixing tribolayer can be distinguished with the red dashed line. The region of 10-15 nm marked by the white dashed lines indicates ultrafine Ni grains which settle at the very outermost surface of the intermixing tribolayer. (b) More close-up HAADF (S)TEM cross-section of the worn 10 nm multilayer sample. White dashed line separates the region for ultrafine Ni grains. (c) Yet another HAADF (S)TEM cross-section which is taken from a different region of the intermixed tribolayer. All cross-sections were prepared parallel to the sliding direction (y-z plane in Figure 2.18).

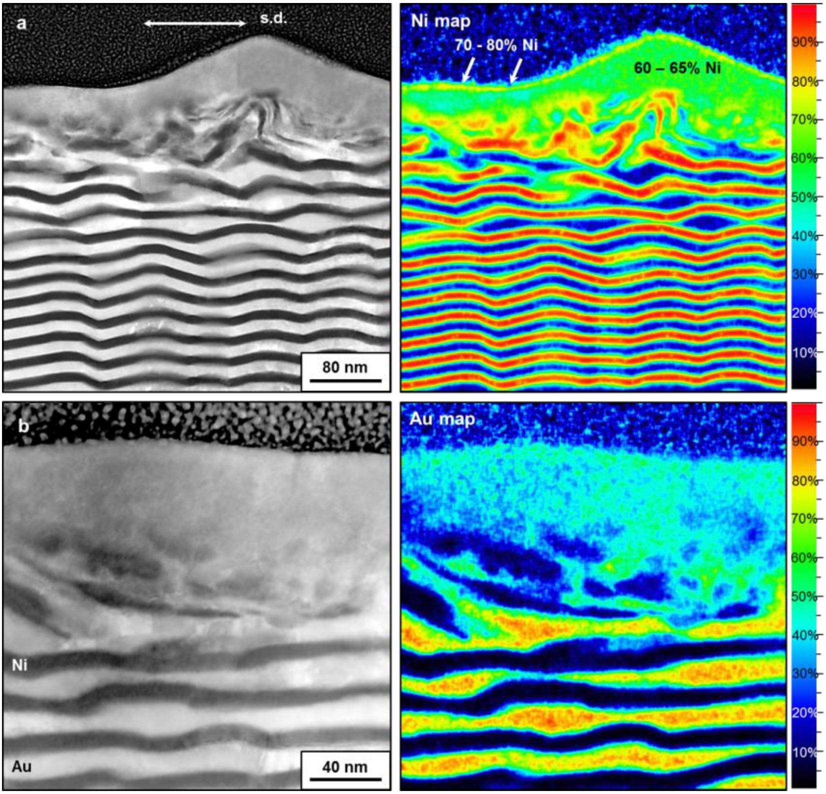
a
s.d.
80 nm
Ni map
70 - 80% Ni
60 – 65% Ni
90%
80%
70%
60%
50%
40%
30%
20%
10%
b
Ni
Au
40 nm
Au map
90%
80%
70%
60%
50%
40%
30%
20%
10%

Figure 3.6: EDXS analysis on the intermixing tribolayer of the worn 10 nm sample. (a) HAADF (S)TEM cross-section parallel to the sliding direction (left), and corresponded EDXS map showing atomic concentrations of Ni (right); (b) HAADF (S)TEM cross-section parallel to the sliding direction (left), and corresponded EDXS map showing atomic concentrations of Au (right).

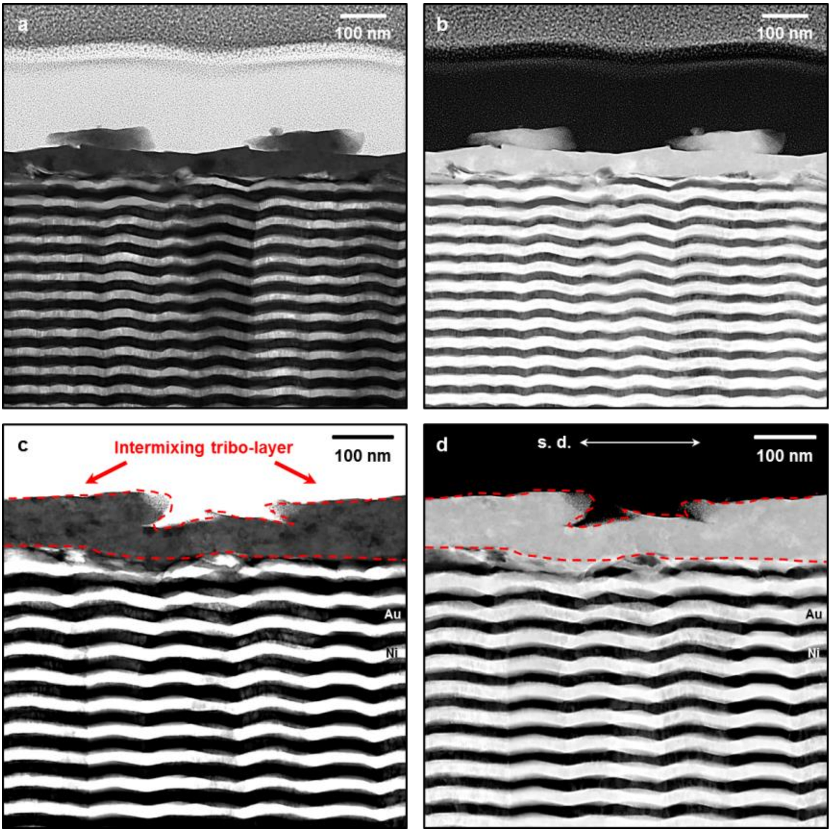

Figure 3.7: Characterization of Au-Ni multilayers with the layer thickness of 20 nm subsequent to the friction test under UHV conditions. (a) BF (S)TEM cross-section of the worn 20 nm multilayer sample. (b) HAADF (S)TEM cross-section of the worn 20 nm multilayer sample. (c) BF (S)TEM cross-section of the worn 20 nm multilayer sample where the intermixing tribolayer can be distinguished with the red dashed lines. The refined grains on the intermixing tribolayer become clearer in this close-up image. (d) HAADF (S)TEM cross-section of the worn 20 nm multilayer sample where the intermixing tribolayer can be distinguished with the red dashed lines. All cross-sections were prepared parallel to the sliding direction (y-z plane in Figure 2.18).

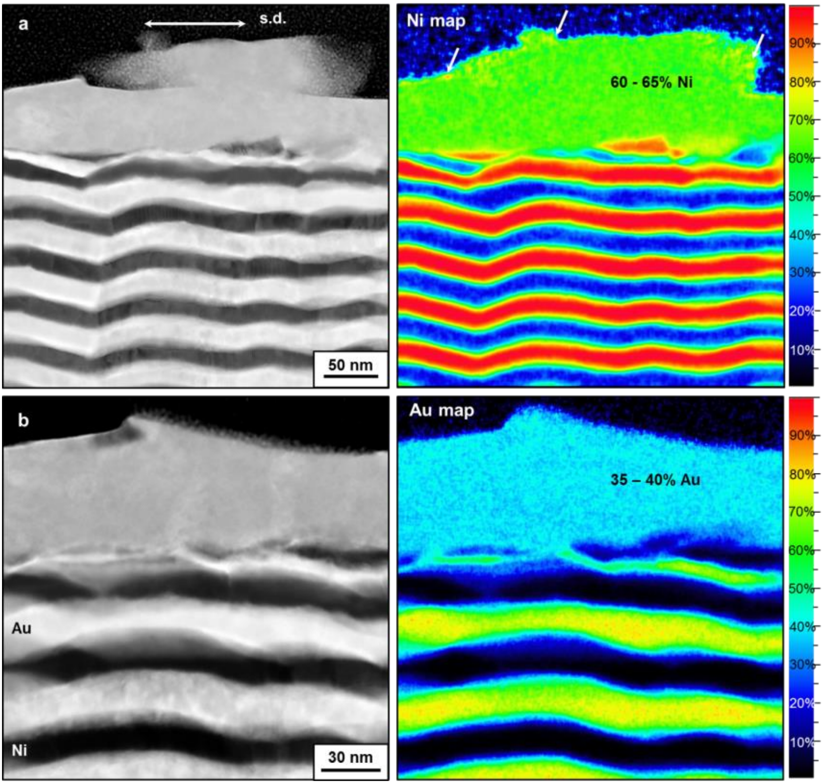

Figure 3.8: EDXS analysis on the intermixing tribolayer of the worn 20 nm sample. (a) HAADF (S)TEM cross-section parallel to the sliding direction (left), and corresponded EDXS map showing atomic concentrations of Ni (right); (b) HAADF (S)TEM cross-section parallel to the sliding direction (left), and corresponded EDXS map showing atomic concentrations of Au (right).

The quantitative EDXS maps on the right-hand side in Figure 3.8 represent the atomic concentration of Ni (Figure 3.8a) and Au (Figure 3.8b) of the corresponding (S)TEM cross-section images on the left-hand side. Differently from the 10 nm sample, the distribution of Au and Ni in the intermixed tribolayer seems to be more homogeneous, however, also giving a mean value of 35-40 at% Au and 60-65 at% Ni, respectively. Again, ultrafine Ni-grains tend to be present at the upmost surface region as seen from the EDXS map indicating with the white arrows (Figure 3.8a).

The shear-induced microstructure with the layer thickness of 50 nm is presented in Figure 3.9 and the structure situated at the start of the wear track is depicted in Figure 3.9a-b. From those images, it is quite obvious that shear instabilities (inhomogeneous structures on the sub-surface produced by the plastic deformation of the multilayers during sliding), which are shown with the red curved arrows, lead to mixing of the layers due to the formation of the localized strains. The microstructure of the 50 nm multilayer sample shown in Figure 3.9 differs from the 10 nm and 20 nm samples in so far as only 5 layers have been mixed from which 3 are Au and 2 are Ni but fragments of the individual layers can still be distinguished in the intermixed zone as depicted by the position almost the middle of the wear track in Figure 3.9c-d. Upper and lower bounds of the intermixing tribolayer are indicated with the red dashed lines in Figure 3.9c-d, and the thickness of the mixed layer is around 200 nm, supporting former hypothesis that thickness of the intermixed tribolayer increases with increasing individual layer thickness of the multilayer system.

The quantitative EDXS maps on the right-hand side in Figure 3.10 represent the atomic concentration of Ni (Figure 3.10a) and Au (Figure 3.10b) of the corresponding (S)TEM cross-section images on the left-hand side. Compared to the 10 nm and 20 nm samples, a more heterogeneous microstructure is observed in the 50 nm sample; where the atomic concentration of Au in the mixed tribolayer is much higher than that of Ni (mean values: 70 at% Au; 30 at% Ni).

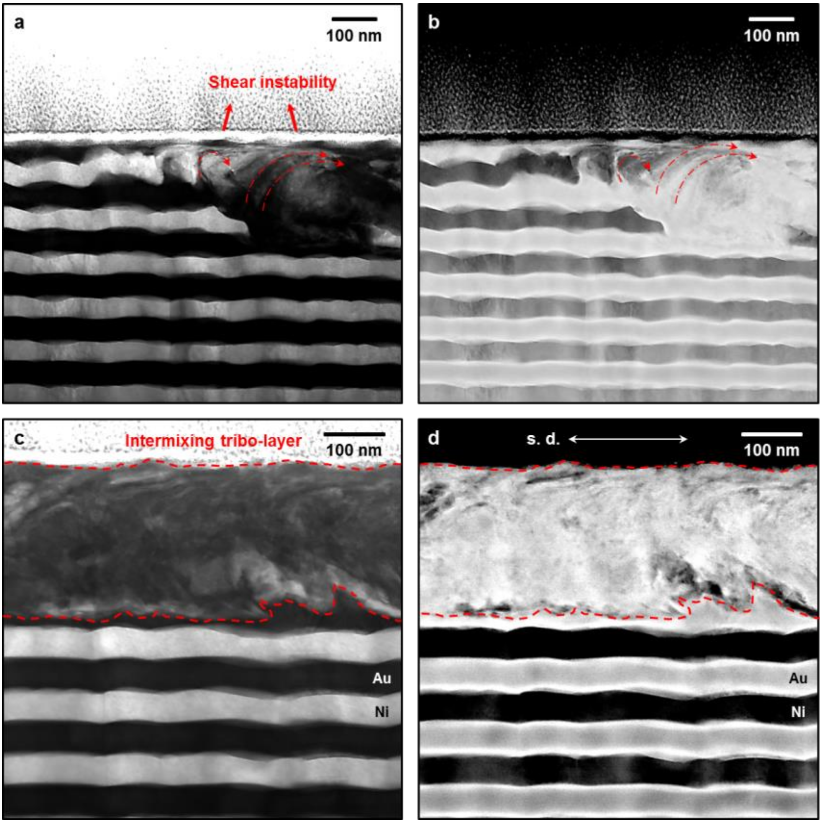

Figure 3.9: Characterization of Au-Ni multilayers with the layer thickness of 50 nm subsequent to thefriction test under UHV conditions. (a) BF (S)TEM cross-section of the worn 50 nm multilayer sample taken from the top of the wear track. (b) HAADF (S)TEM cross-section of the worn 50 nm multilayer sample taken from the top of the wear track. Shear instabilities (the early step of the mechanical mixing) lead to mixing of the layers due to the formation of the localized strains on the sub-surface (a-b). (c) BF (S)TEM cross-section of the worn 50 nm multilayer sample taken from the middle of the wear track. (d) HAADF (S)TEM cross-section of the worn 50 nm multilayer sample taken from the middle of the wear track. Red dashed lines indicate the intermixing tribolayer (c-d). All cross-sections were prepared parallel to the sliding direction (y-z plane in Figure 2.18).

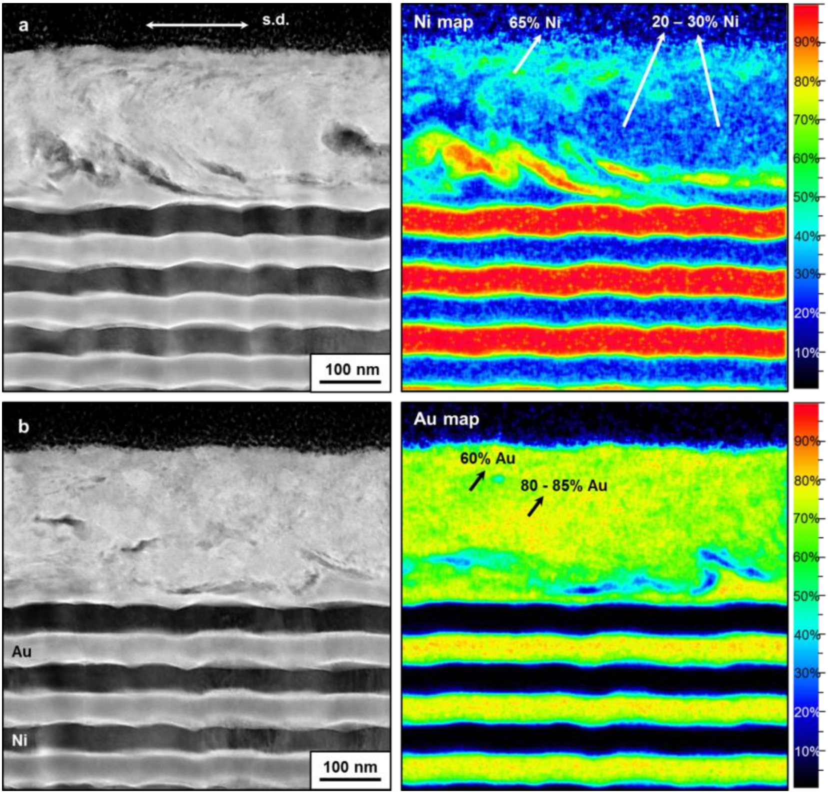
a
s.d.
100 nm
Ni map
65% Ni
20 – 30% Ni
90%
80%
70%
60%
50%
40%
30%
20%
10%
b
Au
Ni
100 nm
Au map
60% Au
80 - 85% Au
90%
80%
70%
60%
50%
40%
30%
20%
10%

Figure 3.10: EDXS analysis on the intermixing tribolayer of the worn 50 nm sample. (a) HAADF(S)TEM cross-section parallel to the sliding direction (left), and corresponded EDXS map (right). The white arrows show the atomic concentrations of Ni. (b) HAADF (S)TEM cross-section parallel to the sliding direction (left), and corresponded EDXS map (right). The black arrows show the atomic concentrations of Au.

Finally, the thickest multilayer structure with a layer thickness of 100 nm resulted in a thinning of the topmost Au layer, as such 25-30% in the very end, and 50-55% in the middle of the wear track; in other words, only first Au layer is plastically deformed during sliding for 100 cycles and subsequent layers are unaffected under these sliding conditions. Correspondingly, a pile-up of the ploughed Au can be seen at the end of the wear track from the STEM micrograph shown in Figure 3.4d.

3.3.1.2 TEM/HRTEM analysis

In order to further analyze the worn 10 nm Au-Ni multilayer sample at higher resolution/ magnification, a TEM/HRTEM investigation has been employed. Figure 3.11 summarizes the main findings of the investigation where micrographs of the intermixed nanocrystalline zone are shown. The zone is composed of ultrafine Au, Ni and/or AuNi grains, as well as coarsened ones between the 'incompletely' deformed layers beneath this zone. An overview of the corresponding surface is displayed in Figure 3.11a while a close-up image highlighted with the yellow dashed square is given in Figure 3.11b. The coarsened grains in different contrasts beneath the intermixing tribolayer are marked with the yellow arrows, and the shear-induced defects in grains can be better defined at this resolution. In Figure 3.11c deformed but unmixed, individual fragments are recognized and labeled by the blue dashed square. Beyond, the fully-mixed, nanocrystalline (grayish) zone can be distinguished at the very surface and a SAED pattern taken from this specific zone is depicted with the inset of the figure. The calculated diffraction intensities in the measurements vary in between 0.2180 and 0.2197 nm^{-1}. A HRTEM image taken from between the mixed and the unmixed regions is presented in Figure 3.11d. The red arrows depict the nanocrystalline grains and the strained nanocrystals in the worn region.

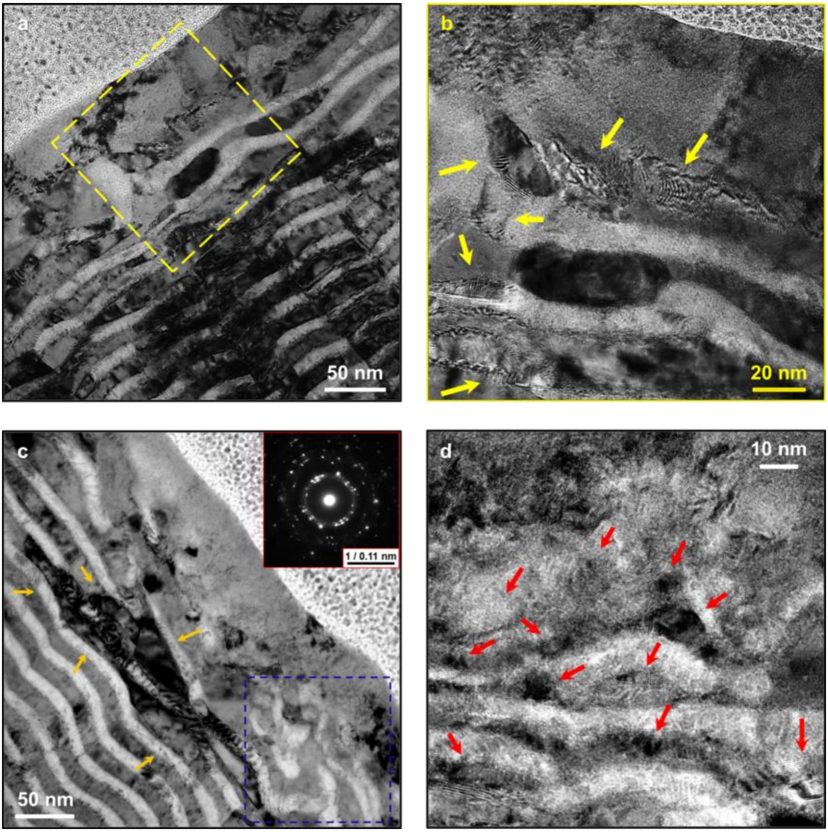

Figure 3.11: TEM images of the worn 10 nm multilayer sample under UHV conditions. The images show intermixed nanocrystalline zones with the ultrafine Au, Ni and/or AuNi grains, and the coarsened ones between ‘incompletely’ deformed layers beneath this zone. The crystal defects are visible both in the intermixed zone and among the individual Au and Ni layers. (a) An overview to the corresponding surface in which the coarsened grains situated between incompletely deformed layers right below the mixed nanocrystalline region are remarkable. (b) A close-up image which is highlighted with the yellow dashed square in (a). The yellow arrows indicate coarsened grains in different contrasts. The defects can become more definable in this resolution. (c) The yellow arrows remark the coarsened grains beneath the intermixed nanocrystalline

zone, and deformed but unmixed, individual fragments can be recognized from the blue dashed square. The fully-mixed, nanocrystalline (grayish) zone can easily be distinguished at the very surface and a SAED pattern taken from this specific zone is depicted with the inset of the figure. (d) A HRTEM image taken from between the mixed and the unmixed regions, where unmixed regions have however stress-induced deformed layers. The huge amount of the residual strain is the main parameter which inhibits taking a better quality image in this sample as clearly followed by the picture noise. The red arrows depict the nanocrystalline grains and the strained nanocrystals in the worn region.

3.3.2 Microstructure characterization under N_2 atmosphere

For microstructural evolution of the worn/deformed Au-Ni multilayers after the friction tests under N_2 atmosphere, cross-sectional imaging by FIB milling has been utilized either parallel (y-z plane in Figure 2.18) or perpendicular (x-z plane in Figure 2.18) to the sliding direction. In discordance with the UHV results previously given, A distinctive microstructural evolution has been found in dry N_2, attributed to different interface characteristics; rather than obtaining a mixture between Au and Ni layers, only the uppermost Au layers were affected by shearing.

3.3.2.1 Cross-sectional (S)TEM analysis via TEM

In order to analyze the worn structures and investigate the sub-surface chemistry, (S)TEM imaging, operated in both the BF and the HAADF mode, in combination with the EDXS analyses have been performed on the multilayer samples. The results of the 10 nm sample are presented in Figure 3.12. In contrast to the previous experiment in UHV any kind of intermixing between Au and Ni layers has been observed. Instead the first Au layer has been influenced only; in that a tribolayer having around 20 nm thickness segregated from the remaining material of the layer has been observed.

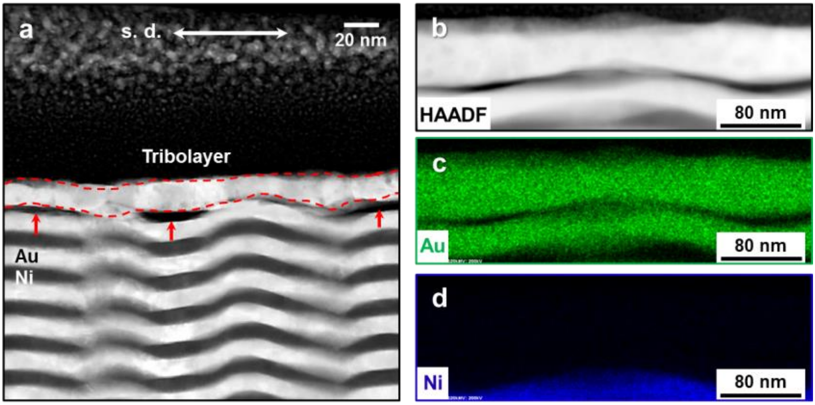

Figure 3.12: Characterization of Au-Ni multilayers with the layer thickness of 10 nm subsequent to the friction test in N_2 atmosphere. (a) HAADF (S)TEM cross-section of the worn 10 nm multilayer sample. Severance of the tribolayer is observed. (b) A close-up HAADF (S)TEM cross-section for the EDXS analysis. (c) Corresponded EDXS map showing weight concentration of Au. (d) Corresponded EDXS map showing weight concentration of Ni. All cross-sections were prepared parallel to the sliding direction (y-z plane in Figure 2.18).

The corresponding EDXS maps of the tribolayer are shown in Figure 3.12c-d. Figure 3.12c represents the weight concentration of Au and Figure 3.12d displays the weight concentration of Ni on the tribolayer of the corresponding (S)TEM image in Figure 3.12b. These EDXS maps revealed the existence of Au (Figure 3.12c) and the absence of Ni (Figure 3.12d) on the tribolayer.

Figure 3.13 gives the detailed structural analysis for the multilayer system with the layer thickness of 20 nm. Also in this case, no mixed structure of Au and Ni is observed. Only the first Au layer is influenced by shearing and the first Ni layer is still undeformed in common with the 10 nm sample. The affected Au layer has grown in thickness from 20 nm to 40-45 nm during shearing as noticed from Figure 3.13a.

The corresponding EDXS maps of the tribolayer are shown in Figure 3.13c-d. Figure 3.13c represents the weight concentration of Au and Figure 3.13d displays the weight concentration of Ni on the tribolayer of the corresponding (S)TEM image in Figure 3.13b. These maps confirm that there exists no Ni in the tribolayer; it only contains reproduced Au.

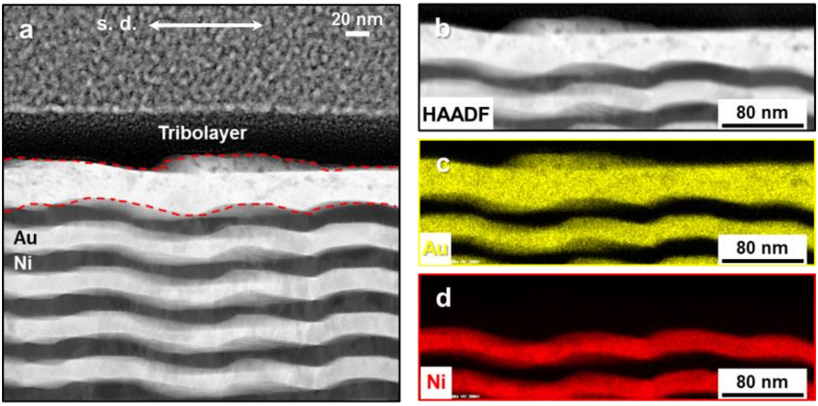

Figure 3.13: Characterization of Au-Ni multilayers with the layer thickness of 20 nm subsequent to the friction test in N_2 atmosphere. (a) HAADF (S)TEM cross-section of the worn 20 nm multilayer sample. (b) A close-up HAADF (S)TEM cross-section for the EDXS analysis. (c) Corresponded EDXS map showing weight concentration of Au. (d) Corresponded EDXS map showing weight concentration of Ni. All cross-sections were prepared parallel to the sliding direction (y-z plane in Figure 2.18).

In the 50 nm sample, it appears that the counter body (ruby ball) broke through the top Au layer, in that the bottom portion is still adhered to the Ni under layer, but the top portion is damaged and void formed. The cross-sections in Figure 3.14a-b, which are perpendicular to the sliding direction (x-z plane in

Figure 2.19), manifest the deformation of the uppermost Au layer where the red dashed line indicates the segregation between damaged and undamaged portions of this layer.

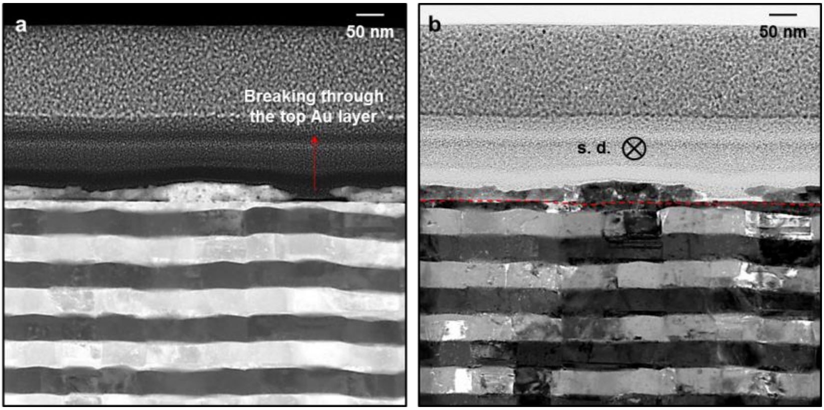

Figure 3.14: Characterization of Au-Ni multilayers with the layer thickness of 50 nm subsequent to the friction test in N_2 atmosphere. (a) HAADF (S)TEM cross-section of the worn 50 nm multilayer sample. (b) BF (S)TEM cross-section of the worn 50 nm multilayer sample. The top Au layer is completely broken in some zones, in that the bottom portion is still adhered to the Ni under layer (see the red dashed line), and void formed. All cross-sections were prepared perpendicular to the sliding direction (x-z plane in Figure 2.18).

The 100 nm sample also did not appear to have any kind of an intermixed layer. By comparison with the UHV result, little impact is observed following the thinning of the topmost Au layer by 10-30% as displayed in Figure 3.15a-b. Only first Au layer is plastically deformed while subsequent layers are unaffected under shearing.

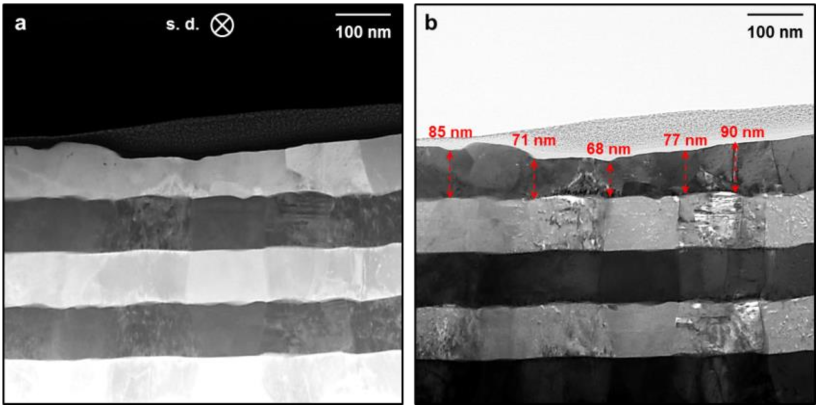

Figure 3.15: Characterization of Au-Ni multilayers with the layer thickness of 100 nm subsequent to the friction test in N_2 atmosphere. (a) HAADF (S)TEM cross-section of the worn 100 nm multilayer sample. (b) BF (S)TEM cross-section of the worn 100 nm multilayer sample. Only the top Au layer is damaged. All cross-sections were prepared perpendicular to the sliding direction (x-z plane in Figure 2.18).

3.3.2.2 TEM/HRTEM analysis

In order to further analyze the worn microstructures of Au-Ni multilayer samples with atomic resolution, TEM/HRTEM analyses have been performed. Figure 3.16 displays the TEM images of the worn 10 nm multilayer sample in which the crystalline zone is visible. An overview of the corresponding surface is displayed on the left hand-side while a close-up HRTEM image, which is highlighted with the red dashed square, is given on the right of Figure 3.16. The HRTEM image reveals obvious crystallinity on the tribolayer without any amorphization. Moiré patterns are visible in this high-resolution due to the shear-induced overlapping of the grains. Red arrow indicates the severed region between the tribolayer and the unaffected part of the first Au layer.

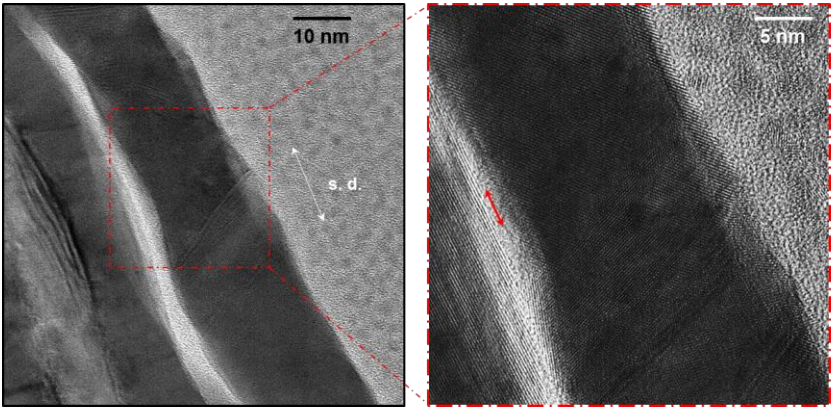

Figure 3.16: TEM images of the worn 10 nm multilayer sample in N_2 atmosphere. The images show the crystalline tribolayer. The close-up HRTEM image, which is highlighted with the red dashed square on the left, reveals obvious crystallinity of the tribolayer without any amorphization. Moiré patterns are visible in this high-resolution due to the shear-induced overlapping of the grains. Severed region between the tribolayer and the unaffected part of the first Au layer can be seen by the red arrow on the right figure.

The thickened, crystalline tribolayer of the 20 nm multilayer sample is shown in Figure 3.17a-b. A second shear-induced thinner layer on the affected (thickened) Au layer is also remarkable in the close-up TEM image in Figure 3.17b (see the black arrows).

HRTEM images of the worn 50 nm multilayer sample are given in Figure 3.18a-b. Damaged, crystalline top portion of the Au and the deformation-induced void are noticeable in both images while the bottom portion, which is still adhered to the Ni under layer, can be clearly seen in Figure 3.18b.

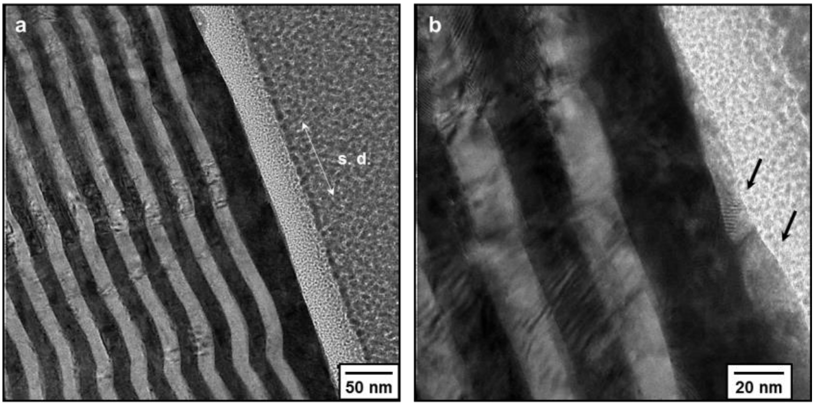
a
s. d.
50 nm
b
20 nm

Figure 3.17: TEM images of the worn 20 nm multilayer sample in N_2 atmosphere. (a) TEM image shows the thickened, crystalline tribolayer. (b) Close-up TEM image shows a second thinner layer on the thickened Au layer which is indicated with the black arrows.

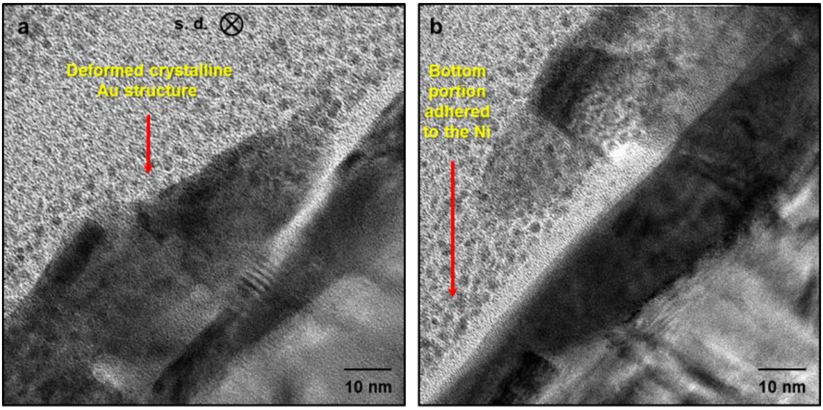
a
s. d.
Deformed crystalline
Au structure
10 nm
b
Bottom
portion
adhered
to the Ni
10 nm

Figure 3.18: HRTEM images of the worn 50 nm multilayer sample in N_2 atmosphere. (a-b) HRTEMimages show the damaged, crystalline tribolayer. The bottom portion is still adhered to the Ni under layer, but the top portion is damaged and void formed.

Figure 3.19 displays the TEM images of the worn 100 nm multilayer sample where the shear-deformed grains on the tribolayer can be distinguished, which also supports the aforesaid deformation of the first Au layer in Figure 3.15. Overlapping of the grains is remarkable in Figure 3.19a (see the red arrows) while the triple junction point of the grains is indicated with the white arrows in Figure 3.19b.

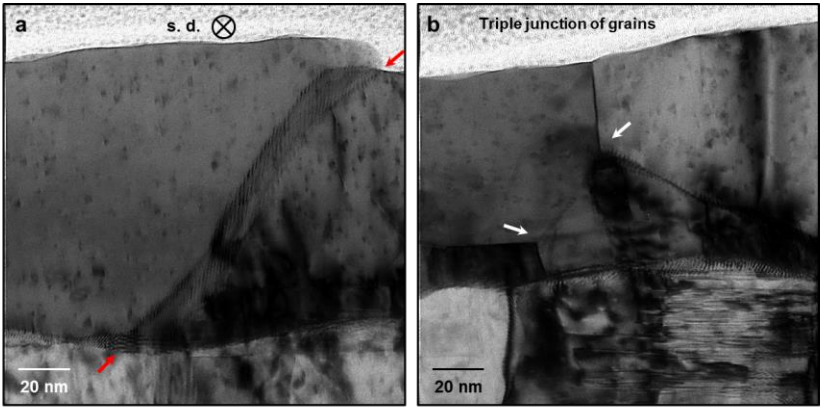

Figure 3.19: TEM images of the worn 100 nm multilayer sample in N_2 atmosphere. (a-b) TEM imagesshow the shear-induced grains on the tribolayer. Overlapping of the grains is remarkable (see the red arrows in (a)) while the triple junction point of the grains is indicated with the white arrows in (b).

3.4 Microstructure characterization of the 10 nm and 100 nm Au-Ni multilayers subsequent to the friction tests for 1000 cycles under UHV conditions

3.4.1 Cross-sectional FIB/SEM analysis

The investigation of the deformation behavior of the 100 nm sample after 100 cycles of sliding called for conducting an experiment for a longer time in order to find out if a mixing process starts when the first layer is completely worn through. For this purpose, the 100 nm sample was tested for 1000 sliding cycles under UHV conditions, and in order to analyze the worn structure, the FIB/SEM analysis has been utilized in its basic procedure for both preparation of the cross-sections and imaging in the high resolution (immersion mode; 10 kV, 3.2 nA). Three cross-sections are milled for a detailed microstructural evolution.

Analyzing the 100 nm multilayer sample after 100 reciprocating cycles of sliding under UHV ended in the observation of a pile-up of the first Au layer at the edge of the wear track (see Figure 3.4d). In a similar manner, sliding for 1000 cycles also results in pile-up of the Au either in the direction of sliding or perpendicular to the sliding surface (Figure 3.20). The perpendicular view of the cross section is given in Figure 3.20a and pile-ups as well as thinning of the first Au layer are present. Deep ploughing tracks of the Au in some areas can be noticed due to the multi-asperity roughness of the ruby ball. Figure 3.20b represents a cross section in the direction of sliding from nearly middle of the wear track, in which thinning of the first layer by 50-62.5% is distinguished. Notwithstanding that, back sweeping of some Au during reciprocating sliding was found in this case. The end of the wear track also possesses pile-up of swept Au as seen in Figure 3.20c. Compared to the sliding experiment for 100 cycles, 1000 cycles-experiment ended up with a lower mean COF as of 0.136.

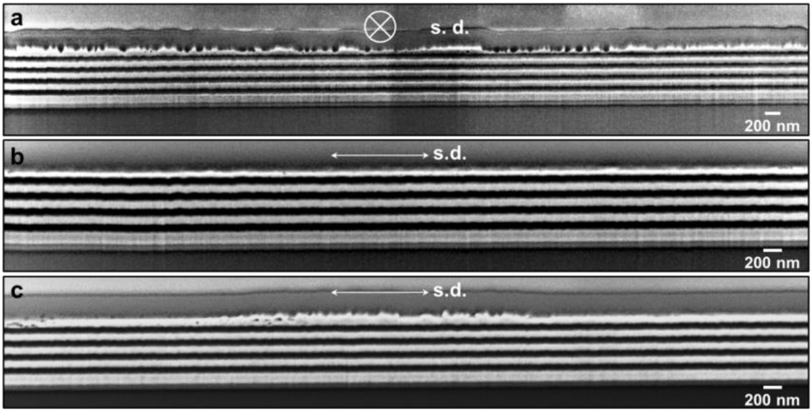

Figure 3.20: Characterization of Au-Ni multilayers with the layer thickness of 100 nm subsequent to the friction test for 1000 cycles. (a) FIB/SEM cross-section of the worn 100 nm multilayer sample, which is prepared perpendicular to the sliding direction. (b) FIB/SEM cross-section of the worn 100 nm multilayer sample, which is cut from the middle of the wear track parallel to the sliding direction. (c) FIB/SEM cross-section of the worn 100 nm multilayer sample, which is cut from the end of the wear track parallel to the sliding direction.

3.4.2 Cross-sectional (S)TEM analysis via TEM

In order to analyze the worn structure and investigate the sub-surface chemistry, (S)TEM imaging, operated in both the BF and the HAADF mode, in combination with the EDXS analyses have been performed on the 10 nm multilayer sample after sliding for 1000 reciprocating cycles.

As stated previously, the first 8 layers are mixed for the 10 nm multilayer sample exposed to 100 reciprocating cycles of sliding under UHV conditions. It is found that the rise in the number of sliding cycles leads to mixing of more layers in the tribolayer as depicted in Figure 3.21. In the latter case, it is observed that the first 18 layers are fully mixed while the remaining 82 layers are unaffected, and the thickness of few upper layers, which are adjacent to the deformed, intermixed region, is reduced. Differently from the previous UHV-fully mixing cases for the 10 nm and 20 nm samples, the formation of the voids (see Figure 3.21a-b) as well as the severance (see Figure 3.21c-d) of the intermixing region, which is indicated with the red dashed lines, is observed. The voids are generated for the first 47-53 nm from the very surface and apparently, these initially formed voids propagated up to 75-125 nm to produce the severance of the tribolayer. Including all these parts, the thickness of the intermixing tribolayer varies from 215 nm to 250 nm. It is important to note that completely breaking off of the intermixing region is also discovered in some parts of the wear track (see Appendix Figure A3).

Figure 3.22a-b also displays the voids and severance of the mixed region. The quantified EDXS maps represent the atomic concentration of Au (Figure 3.22c) and Ni (Figure 3.22d) of the corresponding (S)TEM cross-section images in Figure 3.21a-b. The distribution of Au and Ni in the intermixed tribolayer seems homogeneous in common with that observed for the 10 nm and 20 nm samples for 100 reciprocating cycles of sliding, and also gives a mean value of 35-40 at% Au and 60-65 at% Ni. Compared to the sliding experiment for 100 cycles ($\mu \approx 0.124$), higher friction force ($\mu \approx 0.2$) has been found in the end of the sliding experiment for 1000 cycles.

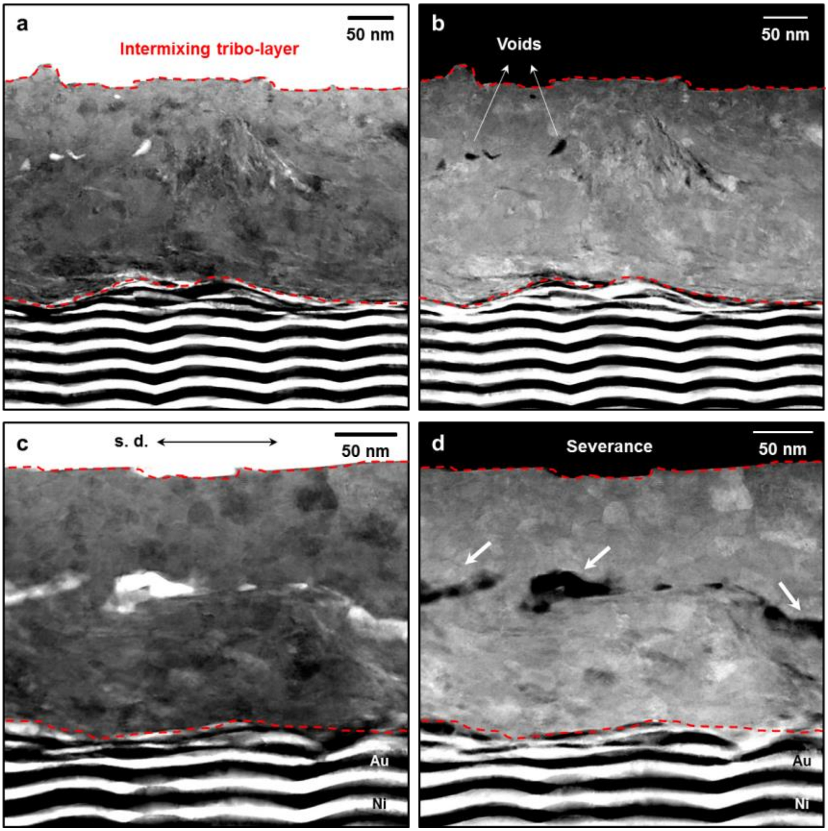
a
50 nm
Intermixing tribo-layer
b
50 nm
Voids
c
s. d.
50 nm
Au
Ni
d
Severance
50 nm
Au
Ni

Figure 3.21: Characterization of Au-Ni multilayers with the layer thickness of 10 nm subsequent to the friction test for 1000 cycles. (a) BF (S)TEM cross-section of the worn 10 nm multilayer sample. (b) HAADF (S)TEM cross-section of the worn 10 nm multilayer sample. (c) A close-up BF (S)TEM cross-section of the worn 10 nm multilayer sample. (d) A close-up HAADF (S)TEM cross-section of the worn 10 nm multilayer sample. The ultrafine grains on the intermixing tribolayer become clearer in this resolution. The intermixing tribolayer is marked with the red dashed lines, on which the formation of voids and severance are observed. All cross-sections were prepared parallel to the sliding direction (y-z plane in Figure 2.18).

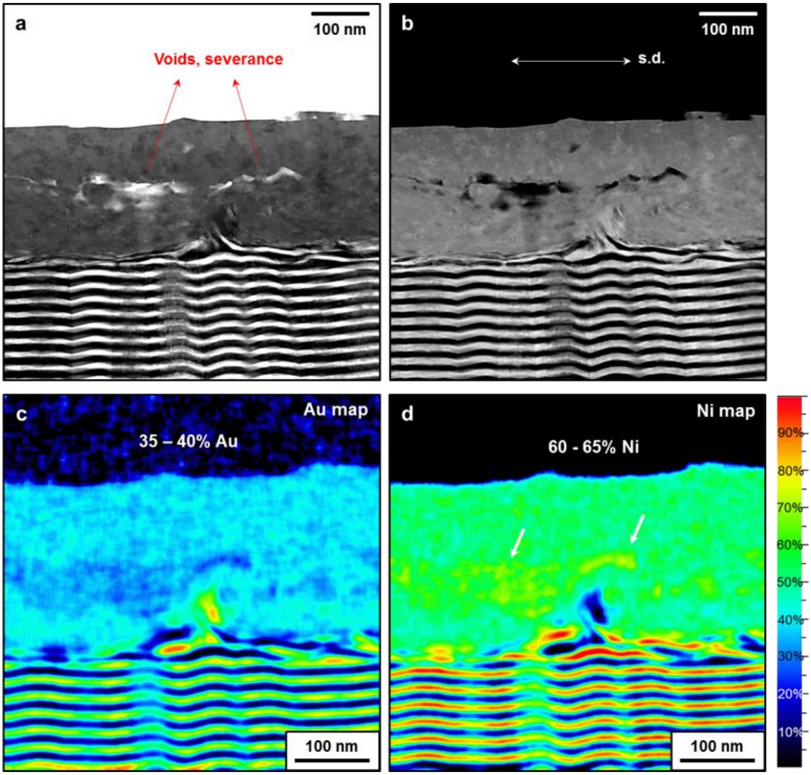
a
100 nm
Voids, severance
b
100 nm
s.d.
c
Au map
35 – 40% Au
100 nm
d
Ni map
60 - 65% Ni
100 nm
90%
80%
70%
60%
50%
40%
30%
20%
10%

Figure 3.22: EDXS analysis on the intermixing tribolayer of the 10 nm sample after sliding for 1000reciprocating cycles. (a) BF (S)TEM cross-section parallel to the sliding direction. (b) HAADF (S)TEM cross-section parallel to the sliding direction. (c) Corresponded EDXS map showing atomic concentrations of Au. (d) Corresponded EDXS map showing atomic concentrations of Ni.

3.4.3 TEM analysis

TEM analysis has been utilized to further analyze the microstructure of the 10 nm sample after 1000 cycles of sliding with the atomic resolution. Figure 3.23 shows the TEM image where the ultrafine Au, Ni and/or AuNi grains are observed in the tribolayer. The fully-mixed, nanocrystalline zone is noticeable at the very surface and a SAED pattern taken from this region is depicted with the inset of the figure. The diffraction intensity is calculated around 0.2184 nm^{-1} which is in the range of 0.2180 to 0.2197 nm^{-1} as already observed for the mixed structure formed after 100 cycles of sliding. The off-white color on the fully-mixed tribolayer indicates the severance.

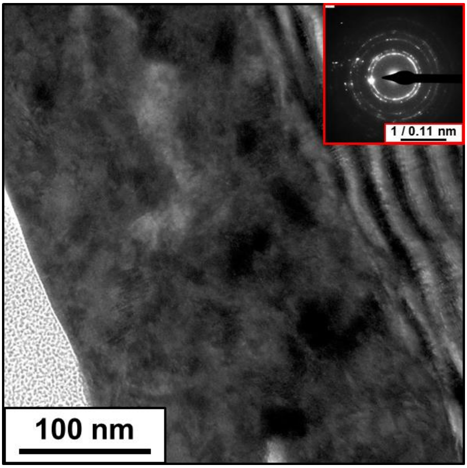

Figure 3.23: TEM image of the 10 nm multilayer sample after sliding for 1000 reciprocating cycles. The fully-mixed, nanocrystalline zone is remarkable at the very surface and a SAED pattern taken from this region is depicted with the inset of the figure.

3.5 Summary of the results

By performing sliding experiments with carefully prepared Au-Ni multilayer samples under well-defined UHV conditions, it has been shown that the individual layer thickness of Au-Ni multilayer systems has a strong impact on the resulting friction force due to the distinctive microstructure evolution close to the surface and a significant increase of the COF with increasing layer thickness has been found. Fully mixed structure between Au and Ni layers of the 10 nm and 20 nm samples (corresponding to the lowest observed friction forces) has been obtained while a partially mixed, Au rich layer has been formed when increasing the layer thickness of the multilayer system to 50 nm. When further increasing the layer thickness (100 nm), rather than a partially or fully mechanical mixing, the thinning of the uppermost Au layer eventuated by plowing and accumulating some Au at the end of the wear track. In N_2 atmosphere, the COF values of each multilayer sample were larger than the ones observed under UHV conditions; except the 100 nm sample for the last sliding cycles (up to the last 20 cycles), which is almost the same for both cases. Interestingly, the relationship between the COF and the layer thickness up to the last 20 cycles would be reasonable since relatively stable friction behavior has been observed in the latter cases. With regard to the microstructural analysis under N_2 environment, in discordance with the UHV results, no mixing behavior has been observed between the Au and Ni layers for all samples. While the deformation of the uppermost Au layers has arisen from plowing the material throughout sliding, material transfer from other areas in contact has also been observed occasionally (which contributes to the thickening of the tribolayer), whereas subsequent layers were unaffected for all samples. For the 10 nm sample, the localized stresses have led to originating severance of the tribolayer. Ultimately, sliding experiments for 1000 reciprocating cycles on the 10 nm sample under UHV conditions has led to increasing the number of fully-mixed layers while completely breaking off of the intermixed tribozone has also been observed in some regions, which has raised the mean COF ($\mu \approx 0.2$) for this multilayer sample. The 100 nm sample showed similarity with the previous 100 cycles-case in terms of deformation of the uppermost Au layer under the same 1000 cycles-sliding conditions, whereas lower friction force has been observed in this 1000 cycles-experiment ($\mu \approx 0.136$).

4 Discussion

4.1 Abstract

A detailed discussion of the results of individual multilayer sample exposed to shearing in different environments is given in this chapter. The possible reasons of the distinctive microstructure evolution under UHV conditions and N_2 atmosphere are initially explained. Following this, the comparison of the friction behavior with regard to the microstructure evolution under different environments is made, mentioning the behavior of wear which must directly depend on the surface characteristics. Afterwards, a theoretical model applied to the corresponding UHV results and based on the relationship between microstructure, deformation mechanism, and friction behavior is addressed by including the appointed limitations for our material system.

4.2 Distinctive microstructure evolution of metallic multilayers worn under UHV conditions

The friction experiments clearly demonstrate that changing the layer thickness leads to very distinctive microstructure evolution for individual Au-Ni multilayer system. While ‘partial mixing’ has been observed for the multilayer sample with the layer thickness of 50 nm, a ‘fully mixed’ material has been found for thinner samples (the case for the 10 nm and 20 nm samples). On the other hand, sliding of samples with a larger layer thickness of 100 nm did not result in mechanical mixing; in the latter case only deformation of the topmost Au layer took place.

4.2.1 ‘Partially mixing’ case: formation of vortex-like structures

During sliding of nanometer scaled ductile materials, local contact asperities lead to the accumulation of plastic strains (heterogeneous sub-structures) near to the surface. Shear instabilities then become more effective to force the material transfer in the sub-surface, which can be assumed as one of the early steps for mechanical mixing of sliding contacts [71]. Despite of a simple thermal diffusion, mechanical mixing takes place due to a plastic flow process from the surface to the emergent sub-surface by means of the material transfer, where local shear instabilities lead to the formation of vortex-like structures. This process has been reported by many authors [76-78, 88] and observed in the Au-Ni multilayer sample with the layer thickness of 50 nm exposed to 100 reciprocating cycles of sliding (see Figure 3.9-10) in the present study.

In our corresponding case, two immiscible metals (see the Au-Ni binary phase diagram in Figure 2.14) exhibit a mixing behavior without any chemical change when they are exposed to the shear stresses under UHV conditions. Although locally induced plastic strains (or applied stress) might not be strong enough to make a full mixture of the layers by creating new phase(s), they suffice to form vortex-like structures by folding 5 layers during sliding. Since the individual Au and Ni layers are still visible in the intermixing tribolayer as shown in Figure 3.9-10, this type of mixing is interpreted as ‘partial mixing’ in this thesis.

4.2.2 ‘Fully mixing’ case: formation of the metastable AuNi alloy

According to the results given in previous chapter, a fully mixed material has been observed for the 10 nm and 20 nm multilayer samples exposed to the reciprocating sliding for 100 cycles, as well as for 1000 cycles (only the 10 nm sample has been investigated). The process of interest is likely that the shear instabilities would be balanced via a more stable microstructure with finer grain sizes during mechanical mixing of Au and Ni layers, which might also lead to the changes in the sub-surface chemistry. This process can then be called mechanical alloying [88], which contributes to the case for the Au-Ni multilayer systems in this work. After friction tests for 100 and 1000 reciprocating cycles, the third-body is produced by grain refinement as well as mechanical alloying process near to the surface.

According to the binary phase diagram of the Au-Ni system [138] (see Figure 2.13), a miscibility gap can only exist at higher temperatures (above a critical temperature, 810.3 °C) because of the fact that in order for two metals to form a solid solution, they must crystallize in the same lattice structure and have similar chemical properties (i.e. similar electronegativity and atomic radius). Hence, the miscibility gap at lower temperatures (below 810.3 °C) leads to the decomposition, and the Au-Ni solid solution breaks down into two separate FCC structural phases below the critical temperature. In other words, these metals do not create an alloy structure under normal circumstances and a separation gap is formed. Because of the immiscibility of this metal pair at lower temperatures, experimental studies are restricted based on forming a thermodynamically stable alloy structure. Recently, Swiatkowska-Warkocka et al. has showed that a metastable AuNi alloy with 55 at% of Ni in Au can be produced via a method ‘pulsed laser irradiation’ of colloidal nanoparticles by overheating and rapid quenching [143]. It is therefore surprising that under shear it appears to be possible to also form a metastable AuNi alloy among these two immiscible metals at equilibrium. Apparently, the increment in the number of grain boundaries due to the grain refinement at the near surface has led to mixing of the ultrafine Au and Ni grains in our corresponding case. This novel, ‘fully mixed’ material is therefore most likely a metastable ‘AuNi’ phase.

To verify the presence of the proposed alloy structure, TEM/HRTEM analysis performed on the 10 nm sample has already been presented in Figure 3.11-23. This analysis confirms the formation of a new crystalline microstructure where individual layers or fragments of Au and Ni cannot be identified. To distinguish Au, Ni and/or AuNi alloy grains from each other, SAED analysis was carried out on the fully-mixed region, however, the diffraction analysis is extremely challenging since Au and Ni have the same crystal symmetry and space groups (Fm3m) in addition to the similar lattice constants [144] (a_{Au} = 0.408 nm, a_{Ni} = 0.352 nm and a_{AuNi} = 0.38 nm). Also, they are splitting off in their (111) Bragg diffraction conditions ($d_{hkl,\mathrm{Au}} = 0.235\ \mathrm{nm}^{-1}$, $d_{hkl,\mathrm{Ni}} = 0.203\ \mathrm{nm}^{-1}$ and $d_{hkl,\mathrm{AuNi}} = 0.22\ \mathrm{nm}^{-1}$) due to the high amount of strain inside the material during measurements as shown with the inset in Figure 3.11-23. Nevertheless, the diffraction intensities are calculated in between 0.2180-0.2197 nm^{-1} on the fully-mixed (alloyed) region, which might be strongly correlated to the value of 0.22 nm^{-1} for the AuNi alloy structure. Thus, it can be argued that within the experimental precision the observed lattice spacing is close to the expected one for the AuNi alloy.

4.2.2.1 Grain coarsening beneath the intermixinig tribolayer

Grain coarsening in nanocrystalline materials is driven by the excess surface free energy. In other words, grains in a material always try to minimize their surface free energies by reducing the total grain boundary energy [145]. At this point, it is worth further addressing the effect of alloying on the microstructure evolution. Alloying contributes to more durable microstructures by refining grains as well as creating Zener pinning sites in the polycrystalline surfaces. Those fine pinning sites reduce the grain boundary mobility by applying a pinning force which can eliminate and compensate the impact of driving force to trigger the mobility. Thus, grain coarsening within the sub-surface might be prevented during mechanical alloying (fully mixing in this thesis) by introducing this kind of pinning sites [146-152]. As previously mentioned, and presented in Figure 3.11, TEM analysis on the 10 nm sample confirmed the formation of a more stable microstructure by grain refinement due to fully mixing of Au and Ni layers near to the surface.

On the other hand, grain coarsening beneath the intermixed region has also been observed as displayed in Figure 3.11. Although residual strain is already present in the as-grown multilayers induced by the lattice mismatch between Au and Ni metals (15%), as well as orientation dependent growth rate, TEM analysis revealed that there should still exist high strain in the material after achieving a more stable microstructure by grain refinement (this evidence can also refer to the SAED analysis shown in Figure 3.11c). TEM images in Figure 3.11 depict the coarsened grains where the process takes place between not completely deformed layers close to the intermixed region, due to that a material tends to recrystallize itself in order to reduce strain. It can be also argued that deforming the hard Ni layers by shearing, it would be possible to fold (softer) Au layers in order to agglomerate them in the grain format.

4.2.2.2 Severance of the intermixinig tribolayer

As stated for 1000 cycles of sliding of the 10 nm sample in section 3.4.2, a longer shear process might contribute to the statement in that the major strain is absorbed by the intermixing region resulting in the severance of the tribolayer. In this latter case, it appears that, instead of dampening the excess surface energy (residual stress) by grain coarsening, the severance of the tribolayer takes this charge due to the propagation of the initially formed voids on the intermixing region. Comparably with grain coarsening beneath the alloyed structure for 100 cycles of sliding (Figure 3.11), the driving force for the severance of the alloyed structure can be the induced surface energy, which surpasses the fracture toughness [153] of the material on the tribolayer. It leads to the intensification of the stress [154] on that region, and then separation of this part would become unavoidable (the resulting higher COF ($\mu \approx 0.2$) compared to that for 100 cycles-experiment arises from the severance of the tribolayer).

4.2.3 Tribologically deformed-layer for the unmixing case: formation of the pile-up

The size of grains and the stress acting on the surfaces in contact are the main parameters which control the deformation processes during sliding. Accordingly, the size of grains must be limited up to a certain level and sufficient amount of applied stress must be provided to control the deformation mechanism, depending on the material applications.

When previous results are considered for the deformation process (the case of fully/partially mixing), it can be noted that the grain sizes of the 10 nm and 20 nm samples and/or the amount of applied stresses are adequate to achieve fully mixing of 7-8 Au and Ni layers, whereas the same conditions only serve the purpose for partially mixing of 5 layers in the 50 nm sample. On the other side, when further increasing the layer thickness up to 100 nm, rather than a partially or fully mechanical mixing, the thinning of the uppermost Au layer eventuates by ploughing and accumulating dislocations at the end of the wear track (see the material pile-up in Figure 3.4d). This process is likely that the major strain is absorbed by the first Au layer, which is exposed to more shear stress on top of the surface, and thus, only this layer is plastically deformed during sliding for 100 cycles since the applied stress is not sufficiently high to deform further layers and/or force the multilayer system for any kind of mixing. Besides, due to the larger grain size compared to the previous samples, a different evolution in the microstructure i.e. bulk-accumulation of dislocations (the pile-up) would become dominant in the deformation process of interest. Under any circumstances, it can be also indicated that the film life can be lengthened during sliding in certain conditions (i.e. unmixed case with the parameters used in this thesis) by utilizing a larger film thickness.

4.3 Distinctive microstructure evolution of metallic multilayers worn under N_2 atmosphere

In contrast to the observation of very distinctive microstructure evolution for individual Au-Ni multilayer system worn under UHV conditions, friction experiments performed in N_2 atmosphere resulted in different microstructure evolution. All in all, much gentler wear has been found for the multilayers sheared in N_2, which has led to the observation of different deformation levels. No mixing between Au and Ni has been detected in the multilayer samples, but rather, the uppermost Au layers only deformed.

4.3.1 Tribologically deformed-layer

When compared to the microstructure evolution under UHV [21], the microtribological experiments in nitrogen demonstrated that the impact of environment on the resulting microstructure is unavoidable. No mechanical mixing of Au and Ni has been observed for the multilayers slid in the glove box filled with nitrogen, in contrast with that obtained in the UHV chamber. Only the uppermost Au layers have been plastically deformed by ploughing in the present cases and smearing of Au from other regions in contact has even been seen for the samples with 10 nm and 20 nm layer thicknesses. As seen in Figure 3.13a, shearing has led for the 20 nm sample, to a thickness increase of about a factor of two (thickness after sliding 40-45 nm), which is most probably caused by the ploughing behavior. A possible explanation to the thickening at this contact asperity can be the accumulation of the material plowed from other areas in contact. For the 10 nm sample, in addition to the thickening of the first Au layer, some part of the tribolayer (around 15-20 nm) severed from the remainder that is a little less than 10 nm (Figure 3.12a). As seen in Figure 3.14, for the 50 nm sample, the same amount of normal stress caused to more damage in the top portion of the first Au layer which resulted in the formation of voids in the near-surface material whereas the bottom portion was still adhered to the Ni under layer. Following the former microstructure evolution of thinner multilayer samples, this groove (asperity) on the wear track must be the one more deeply ploughed amongst others, which would have probably caused to the thickening of the areas due to the redistribution of the plowed material (but we do not see this in the corresponding figures). On the other hand, less damage can be mentioned about sliding of the 100 nm sample by reason of the larger grain size distribution as well as the minor amount of the absorbed strain energy (Figure 3.15).

4.3.1.1 Severance of the tribolayer

In addition to the thickening of the first Au layer, severed structures that are parallel to the sliding surface were found underneath the tribolayer of the 10 nm sample (Figure 3.12). This mentioned process may arise from an increase in compressive stress within the intermixing tribolayer throughout sliding. It could be the result of higher localized stresses, as the plastic deformation can induce the formation and nucleation of cracks beneath the contact region depending on the severity of stress acting on the contacting surfaces [155]. If the stress concentration is high enough to propagate the cracks, sheet-like wear particles are generated. And if these wear particles are continued shearing to the surface, delamination/severance of the sheets takes place. So, according to the theory, it appears that the most destructive failure of sliding surfaces, severance, could occur via the generation of wear particles -initially propagated cracks- due to the stress concentration at the sub-surface of the 10 nm sample. On the other side, the situation for the 20 nm sample, where no separation of the tribolayer was observed, can be explained by the induced strain energy (stress concentration) as well. However in this latter case, the applied stress energy during sliding might have entirely been consumed during shearing without giving any chance to the intensification of the stresses at the sub-surface to form cracks and aforesaid wear particles.

4.4 Comparison of the friction behavior with regard to the microstructure evolution under UHV conditions and N_2 atmosphere

Before dealing with the microstructure evolution, it is significant to compare the friction behavior of the Au-Ni multilayer samples sheared in different environments. For the multilayer samples with the thickness of 10 nm, 20 nm, and 50 nm, low COF has been observed under UHV while the 100 nm sample resulted in much higher friction under the same sliding conditions. On the other hand, performing the tests in a different environment caused to obtain different friction behavior. Figure 4.1 points out this discrepancy among the multilayer samples exposed to different environmental conditions. If looked back on the corresponding graphs in Figures 3.2-3, the frictional stability was highly varying as the number of sliding cycles changes in N_2 atmosphere and besides that, the COF at last cycles were more stable as compared to the overall behavior. Thus, assuming that the last 20 cycles reflect a steady-state situation, the COF values up to the last 20 cycles were included in the comparison of the frictional behavior of the multilayer samples worn under N_2 atmosphere. The COF values for N_2 atmosphere were larger than that observed under UHV conditions; except the 100 nm sample for the last cycles (up to the last 20 cycles), which is identical within error bars in both cases. Interestingly, for the 10 nm, 20 nm, and 50 nm samples (where the mixing between Au and Ni is suppressed in N_2), the friction is higher than UHV. However there is no large difference for the 100 nm sample, where the mixing has not been present either in UHV or in N_2. Notwithstanding that, the higher friction ($\mu \approx 0.312$) can be emphasized under UHV conditions compared to that in N_2 ($\mu \approx 0.292$). Note that lower friction forces of thinner samples under UHV conditions must be associated to the final microstructure regarding to the mechanical mixing of Au and Ni [92], and this might be directly linked to the ‘critical size’ phenomenon [87, 107]. Since we have already verified ultrafine grain sized-microstructure in the 10 nm sample via HRTEM analysis (see Figure 3.11) we can assert that grain sizes observed thorough sliding experiments under UHV conditions (except the 100 nm sample) must be smaller than that observed in N_2 environment even though N_2 experiments also forced the grain size to change (fluctuations on the friction data can be arisen from this enforcement). And thus, lower friction has been found under UHV for thinner multilayer samples. In N_2 environment, the reason of why the lowest friction has been observed in the 10 nm sample also correlates with the size of grains which could be smaller than or on the order of the critical grain size [87].

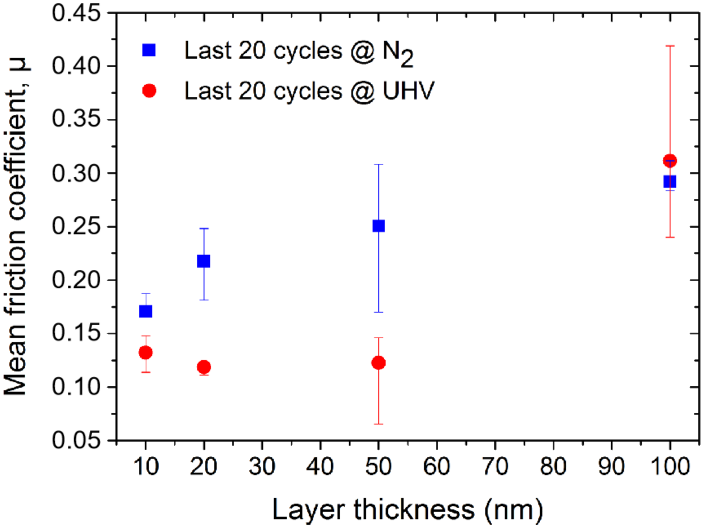

Figure 4.1: Comparison of the COF values between UHV conditions and N_2 atmosphere in terms of the last 20 sliding cycles. The COF values for N_2 atmosphere were larger than that observed under UHV conditions; except the 100 nm sample, where slightly higher friction was found compared to that in N_2.

As a matter of fact, the chosen counter body, ruby (Al_2O_3-Cr), is one of the hardest oxide materials [156], and as a consequence of this, ploughing the relatively soft metallic multilayers by the ruby sphere leads to creating grooves in the wear track. These grooves can have wavy patterns which show the so-called ‘telephone cord-like morphology’ [153, 157] that has become a common phenomenon in thin films under compression. According to Gioia et al. [157], the residual stress anisotropy of thin films might affect the formation of telephone cord-like structures on their surfaces since the mechanics between the thin film structure and the substrate is of responsibility. This interpretation would have a more significant meaning in our case when hardness and stiffness of Au (E_{Au} = 78 GPa) and Ni (E_{Ni} = 200 GPa) multilayers are considered rather than that of Si substrate (E_{Si} = 160-180 GPa for (100) crystal orientation). As a result of this significant difference among the elasticity behavior of Au and Ni, one would expect an anisotropy in the residual strain during the growth of multilayer thin films, in addition to the fact of their 15% lattice mismatch. Figure 4.2 demonstrates the structure of interest on the two referenced wear tracks. Although similar structures (telephone cord-like morphology) have been observed for the wear tracks created under UHV conditions and N_2 atmosphere, the intended environments resulted in quite different wear behavior. Much gentler wear has been found for the multilayer samples sheared in N_2 atmosphere compared to that under UHV, which leads to observing different deformation levels. Figure 4.2a recorded via AFM shows a plan view of the wear track for the 20 nm sample sheared under UHV conditions. Note that lighter colors indicate higher topography whereas darker one shows deeper regions. Also, the side view of the wear track, available below, reveals that the depth varies around 70-80 nm from the surface, which is in line with the previous microstructure evolution (the corresponding EDXS map revealing mechanical mixing of Au and Ni layers) due to the compression of the multilayers during sliding. In addition, a pile-up (≈100 nm) is visible on the surface of the wear track. By analyzing the topography of the other worn multilayer samples via AFM, the depths of the wear tracks are calculated 100 nm, 113-140 nm, and 35 nm for the 10 nm, 50 nm, and 100 nm samples, respectively, and the observed pile-ups are around 100 nm, 102 nm, and 122 nm.

On the other side, these results differ for the case in N_2 atmosphere. The wear behavior is much gentler in this case as recognized from the topographical image of the track in Figure 4.2b. Its side view also reveals the gentler wear behavior by reaching only 20-25 nm (13 nm in some cases) depth from the surface, and even creating several localized trenches on the surface. This analysis would also match to the previous microstructure evolution of the 20 nm sample sheared in N_2 environment where no mixing of Au and Ni was observed (see the corresponding EDXS map). Correspondingly, less pile-up (≈30 nm) has been found on the surface of the wear track. By utilizing topography analysis of other worn multilayer samples via AFM, the depths of the wear tracks are calculated 32 nm, 15 nm, and 36 nm for the 10 nm, 50 nm, and 100 nm samples, respectively, and the observed pile-ups are around 25 nm, 16 nm, and 48 nm.

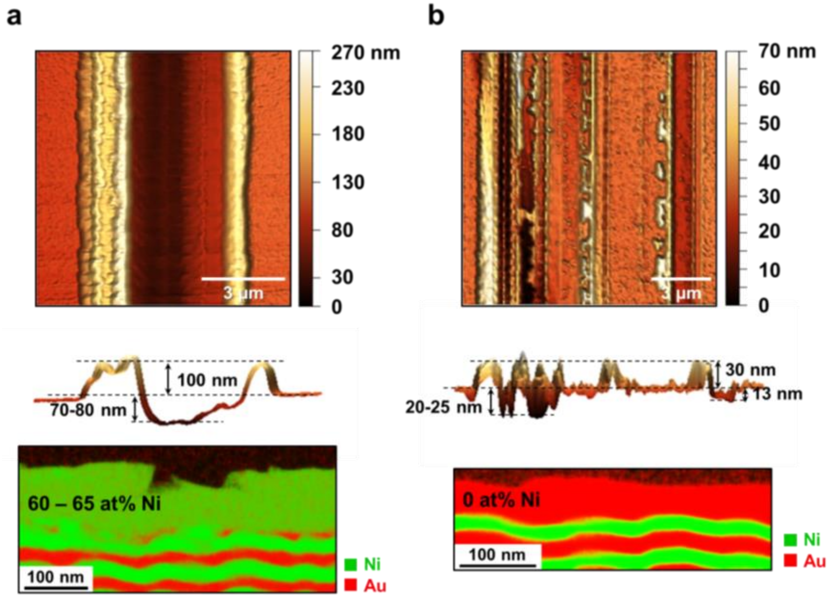

Figure 4.2: AFM topography images of the wear tracks for the 20 nm sample after 100 reciprocating cycles of sliding (a) under UHV conditions and (b) N_2 atmosphere. Ploughing soft multilayers by hard ruby sphere leads to creating grooves in the wear tracks.

At this point, even though the determination of the exact mechanism responsible is beyond the scope of this thesis, it might also be argued that even a minute amount of water vapor in N_2 atmosphere (< 40 ppm H_2O in the experiments presented in this work) can reduce the contact stress between the ruby sphere and the multilayer sample. When the adsorption of water on the initially clean surface of the 'sapphire' [158] is taken into account, one would not be misguided to speculate about the possibility for a similar treatment of water adsorption on the ruby surface. With reference to Schildbach et al., the sapphire surface can be covered by water monolayers at room temperature when it is exposed to higher pressure water. Accordingly, water adsorption leads to changing the surface electronic state of the sapphire and hydroxyl groups can be held responsible for the higher energy loss in the surface spectrum [158].

Considering this, the presence of the water adlayers on the ruby surface might also be conceived in N_2 environment and accountable for the gentler wear behavior of the multilayers by sliding the 'water-covered ruby sphere' over them. In the same direction, the adsorption of water molecule by the interface of the ruby sphere and the Au-Ni multilayer sample would also contribute to this scenario if it is possible energetically.

Furthermore, there might be another factor affecting the wear of the multilayer samples in N_2 atmosphere. Since the multilayer samples have always been cleaned via XPS/Ar ion sputtering prior to the friction tests carried out under UHV conditions, the residual gas structures, which can come from air (C and O_2 as displayed in Figure 2.19), have been removed and pure Au chemistry on top of the sample has been achieved each time; and thus, the influence of gases present in air has not been considered in the UHV experiments. However, in order to clarify the deformation behavior of the multilayer samples worn in N_2 atmosphere, it is important to take into account the gases which might be possible to exist in this mentioned condition. The literature can lend a hand to understand the effect of such an environment on the sliding pairs of the ruby ball and the Au-Ni multilayer sample. After the adsorptions of N_2 and O_2 on Au (111) surfaces have been confirmed, the wetting characteristics of these gases have been studied for Au (111) [159]. Beyond, according to the study reported by Wickham et al. [160], adsorption/chemisorption of N_2 dioxide (NO_2) on polycrystalline gold is also possible. Within this context, it appears that the probability of NO_2 adsorption on the first Au layer during sliding might be considered in our latter case. Similarly, NO_2 binding sites were found on Au (111) surface, in which NO_2 adsorbs as a chelate onto Au (Au (111) O,O´-nitrito surface chelate with C_{2v} symmetry). The chemisorbed NO_2 on Au (111) surface can even react with NO to form N_2O_3 (O=N-0-N=O) [161]. Moreover, it is worthy of note that C has already been found on the multilayer sample surface with respect to the XPS analysis (see Figure 2.19) before the friction test.

In sum, all these evidences bring to mind that adsorption of N_2, O_2, H_2O, and/or the other complexes such as hydrocarbons can serve a function for reducing the contact stress between the ruby ball and the multilayer sample under N_2 atmosphere, by comparison with the UHV conditions. The gas(es) of interest can adsorb onto the uppermost Au layer and form a very thin molecular film (i.e. buffer zone), which dilutes the contact between the sliding bodies when the sample is introduced into the glove box filled with N_2 gas.

4.5 A model based on the relationship between microstructure, deformation mechanism, and friction behavior

For bodies in contact, the applied load is randomly separated among the surfaces during sliding depending on the nature of the asperities, and the friction force leads to produce local changes in stress acting between these bodies due to the deformation of the contact points. In reaction to the deformation-induced plastic strains, the sub-surface microstructure tends to modify, and the friction behavior is supposed to be considered as strongly microstructure dependent.

Friction tests on the Au-Ni multilayer samples for 100 reciprocating cycles under UHV conditions contribute to this fact by having a notably distinctive microstructure evolution such as fully mixing due to the formation of a metastable AuNi alloy in the 10 nm and 20 nm samples, partially mixing driven by the vortex-like structures in the 50 nm sample, and bulk-accumulation of dislocations (the material pile-up) at the end of the wear track of the 100 nm sample. These observations are eventually caused by different deformation mechanisms taking place on the sub-surfaces. In connection with the previous explanations in section 4.2, it has been proposed that there is a critical grain size (so-called the strongest size) [162] which controls the dominant deformation mechanism on the sub-surface during sliding due to the fact that this level is approximately the smallest grain level which allows dislocation movement to continue (i.e. intragranular sliding) and thus can be assumed as the equilibrium distance between two edge dislocations. Within the scope of this idea, the dominant deformation mechanism changes from bulk to interface (from dislocation to grain boundary) below this critical size since the number of grains raises and dependently, grain boundaries become more dominant in the sub-surface [162]. According to the molecular dynamics (MD) simulations by Schiøtz et al. [163], each grain would be individually responsible for the slip events and the sum of these independent motions at grain boundaries constructs the dominant deformation mechanism in this latter case.

In line with this theory, a model, which attempts to relate the deformation mechanism to the friction force [87], has recently been presented by Argibay and coworkers. The equation to determine the critical grain size ***r*** by using the definition for the dislocation splitting distance r_0 found in Yamakov et al. [107] is given in Equation 4.1 [107, 87]:

$$r = \frac{r_0}{1 - \sigma_a / \sigma_\infty} \tag{4.1}$$

σ_a denotes the applied stress and $\sigma_\infty = 2\,\gamma_{sf} / \mathrm{b}$ is the critical shear stress of the material. r_0 is the equilibrium dislocation splitting distance at zero stress which is defined as:

$$r_0 = \frac{(2+\nu)\,G\,b^2}{8\,\pi\,(1-\nu)\,\gamma_{sf}} \tag{4.2}$$

where γ_{sf} is the stacking fault energy (SFE), ν is the Poisson's ratio, G is the shear modulus, and b is the Burgers vector for the dislocation. σ_a/σ_∞ can be utilized as the reduced stress parameter and the applied stress σ_a on the sliding surface is calculated using the Hamilton contact model as follows:

$$\sigma_a = \frac{3\,F_N}{2\,\pi\,a^2}\left[\frac{1-2\nu}{3} + \frac{4+\nu}{8}\,\pi\,\mu\right] \tag{4.3}$$

here F_N refers the applied load, μ is the friction coefficient and a is the contact radius calculated by the Hertzian contact model.

According to this model, high friction would be expected (in general) when a stress greater than the critical shear stress of the material is applied during sliding ($\sigma_a / \sigma_\infty \geq 1$). Otherwise, an applied stress which is lower than the critical shear stress would lead to lower friction force. Here, one can approach about two different probabilities:

1) The reduced stress parameter can be 0.5 and/or less than 0.5 ($\sigma_a / \sigma_\infty \leq 0.5$).
2) The reduced stress parameter can be less than 1, but greater than 0.5 ($0.5 < \sigma_a / \sigma_\infty < 1$).

At that point, the critical grain size ($2r_0$) would become a part of the activity to control the dominant deformation mechanism. The imposed grain size must be adequate to drive the dislocation motion resulting in dislocation-mediated deformation leading to a 'relatively' high friction force ($0.5 < \mu < 1$) for the case of $0.5 < \sigma_a / \sigma_\infty < 1$. On the other side, the grain size, which is smaller than the critical size, would lead to much lower friction force when the reduced stress parameter is 0.5 and/or below this value ($\sigma_a / \sigma_\infty \leq 0.5$) since the formation of stacking faults might be suppressed. In this case, purely grain boundary-mediated deformation would be expected due to the refinement of grains in the sub-surface. Thus, '0.5' would be the threshold value for the reduced stress parameter to transform the dominant deformation mechanism from grain boundary- to dislocation-mediated deformation, or vice versa depending on the critical grain size $2r_0$.

4.5.1 Predictions from the model for corresponding UHV results

The deformation mechanisms for individual multilayer system worn under UHV conditions have been carefully studied in this thesis, according to the initial surface grain size, d and the dislocation splitting distance, *r* as specified in the model [107, 87]. The values for the Au-Ni multilayer systems with different layer thicknesses are calculated by taking into account the parameters summarized in Table 4.1, and the map for the dominant deformation mechanisms related with the friction force, reduced applied stress and the surface grain size is plotted in Figure 4.3.

The model predicts that the multilayer samples with a layer thickness of 10 nm, 20 nm and 50 nm fall into the regime which belongs to the grain boundary-mediated deformation with low friction. On the other hand, the multilayer system with the layer thickness of 100 nm resulted in different behavior which means that dislocation-mediated deformation should be in charge for the observed higher friction behavior. The experimental observation shown in Figure 3.4d is also consistent with this argumentation due to the existence of a material pile-up at the end of the wear track subsequent to shearing process. Rather than a mixing, thinning of the uppermost Au layer has been observed in this sample which demonstrates a bulk-accumulation of dislocations as long as sliding occurs in mentioned conditions. As previously stated, the critical grain size phenomenon might be assigned to this observation. By using the Scherrer equation with the XRD data, the initial grain size has already been calculated around 48.75 nm for Au and 53.71 nm for Ni in the as-grown 100 nm sample which is the largest among the others (see Table 2.2), and the TKD measurement on the cross- sectional area in Figure 4.4 also shows large grains of the 100 nm sample after the friction test (mean value of the upmost 12 grains: 67 nm in height and 73 nm in width). In this regard, the grain size of this sample is large enough (greater than the critical grain size $2r_0$, which must be in the range of 9.8-17.26 nm according to the calculations presented in Table 4.1) to drive the dislocation motion during sliding in mentioned conditions.

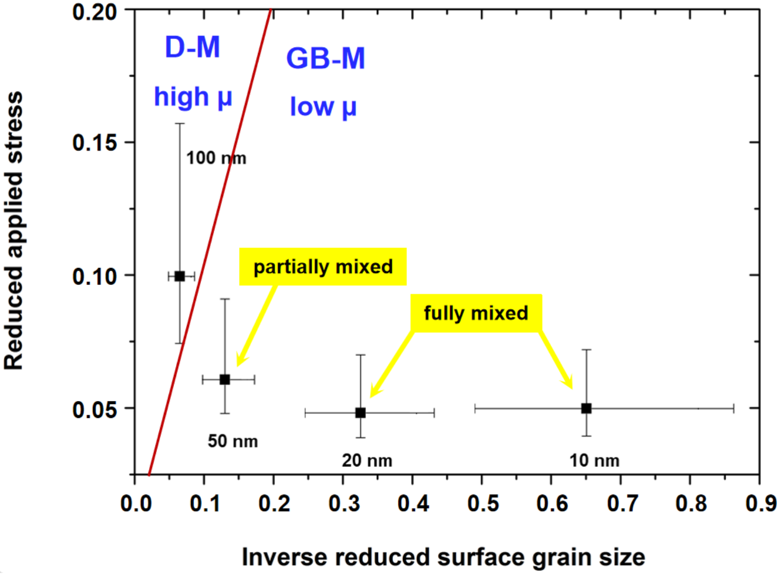

Figure 4.3: Map for the dominant deformation mechanism (grain boundary, GB- or dislocation, D-mediated) related with the friction force (µ, coefficient of friction) in terms of the reduced applied stress and the surface grain size which is adapted from [87]. Data points are calculated based on the mean values of Au and Ni using correspondent equations (see the text) and the error bars depict the individual values for Au and Ni. The model predicts that multilayer systems with a layer thickness of 10 nm, 20 nm and 50 nm fall into the regime which belongs to the grain boundary-mediated deformation with low friction whereas the 100 nm sample with higher friction should be connected to the dislocation-mediated deformation.

Table 4.1. Experimental data and calculated parameters for studied model

Au-Ni ($\nu = 0.375$; $E = 125$ GPa; $G = 51.5$ GPa; b = 2.69 A; $\gamma_{sf} = 86.5$ mJ/m^2)

d (nm)	μ	r_0 (nm)	r_e (nm)	r_0 / d	a (μm)	σ_∞ (MPa)	σ_a (MPa)	σ_a / σ_∞
10	0.124352	6.51	6.851	0.651	2.4	643	32	0.0498
20	0.115686	6.51	6.84	0.3255	2.47	643	31	0.0482
50	0.1505	6.51	6.93	0.1302	2.58	643	39	0.0607
100	0.28212	6.51	7.23	0.0651	2.52	643	64	0.0995

Au ($\nu = 0.44$; $E = 79$ GPa; $G = 27$ GPa; b = 2.88 A; $\gamma_{sf} = 45$ mJ/m^2)

d (nm)	μ	r_0 (nm)	r_e (nm)	r_0 / d	a (μm)	σ_∞ (MPa)	σ_a (MPa)	σ_a / σ_∞
10	0.124352	8.63	9.3	0.863	2.66	312	22.53	0.072
20	0.115686	8.63	9.28	0.4315	2.72	312	21.84	0.07
50	0.1505	8.63	9.494	0.1726	2.85	312	28.44	0.091
100	0.28212	8.63	10.24	0.0863	2.79	312	48.94	0.157

Ni ($\nu = 0.31$; $E = 170$ GPa; $G = 76$ GPa; b = 2.49 A; $\gamma_{sf} = 128$ mJ/m^2)

d (nm)	μ	r_0 (nm)	r_e (nm)	r_0 / d	a (μm)	σ_∞ (MPa)	σ_a (MPa)	σ_a / σ_∞
10	0.124352	4.9	5.1	0.49	2.27	1028	40.65	0.0395
20	0.115686	4.9	5.098	0.245	2.32	1028	40	0.0389
50	0.1505	4.9	5.147	0.098	2.43	1028	49.39	0.048
100	0.28212	4.9	5.293	0.049	2.38	1028	76.43	0.0743

To evaluate the critical size more precisely, the grain size of the other multilayer samples obtained from the XRD data must be highlighted once more. As given previously in Table 2.2, the calculated grain size values are 1.08 nm, 16.47 nm, and 28.97 nm for Au and 11.22 nm, 20.43 nm, 40.99 nm for Ni in the 10 nm, 20 nm, and 50 nm samples, respectively before the friction tests. The presence of an ultrafine grain structure of the intermixing tribolayer was experimentally confirmed to be achieved by fully mixing of the 10 nm and the 20 nm samples. Moreover, the HRTEM analysis even revealed this refinement process in the fully mixing tribolayer which is responsible for the lower friction. It can be argued that ultrafined grains lead to an increased number of grain boundaries which hinder the transmission of dislocations; and therefore, shearing occurs at the newly formed grain boundaries behaving as an incommensurate, low shear contact (corresponds to low friction). Even though a partially mixed structure is formed during sliding of the 50 nm sample, the vortex-like structures would probably prevent to result in high friction force in this case by refining grains in the partially mixing tribolayer. These observations can be regarded as the evidence of the results shown in the map based on grain boundary-mediated deformation when the range of the critical grain size (9.8 to 17.26 nm) is considered.

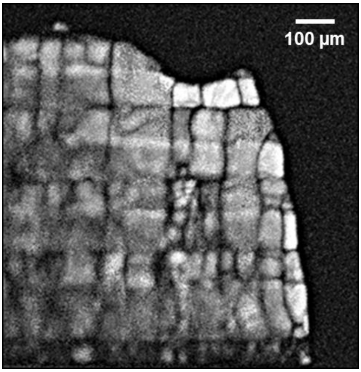

Figure 4.4: TKD measurement on the cross-sectional area of the 100 nm sample which shows relatively large grains after the friction test.

4.5.2 Limitations of the model for our material system

1) In the previous section, modifications in microstructures have already been shown after exposing the materials to shear in which they resulted in a process including partially and fully mixing within the more stable microstructures compared to the as-grown multilayer thin films. However, not explained by the model is the difference in friction between the 50 nm sample and thinner multilayers, in that the newly formed AuNi phase within the very small grain size at the very surface showing the lowest friction (for the 10 nm and 20 nm samples) might be ascribed.

   Indeed, this model can be extended beyond the state of the art at this stage because the origin of this proposed friction-deformation model is a modified version of the deformation model developed by Yamakov et al. [107] in which the distinction between perfect (complete) and partial (incomplete) slip deformations of low SFE and high SFE FCC metals has been explained very well. However, only perfect dislocations have been considered in the proposed model [87] without incorporating the partial dislocations even though grain boundary- and dislocation-mediated deformations have been handled properly. In fact, complete and incomplete dislocations usually cooperate with each other to manage the deformation behavior such as transition from conventional to partial slip at the dislocation-splitting line. Partial dislocations can therefore be the key to inhibit the propagation of dislocations across the grains since the stacking faults transect the grains when they are sufficiently small. Hence, considering the low and high stacking fault energies of Au (γ_{sf} = 45 mJ/m^2) and Ni (γ_{sf} = 128 mJ/m^2), we can for example refer to the possible transition from the partial dislocation- to grain boundary-mediated deformation during sliding of the 50 nm sample arising from the formation of the vortex-like structures (where the grain size is assumed on the fringe of critical size) as well as its inevitable impact on friction.

2) According to the assigned model, dislocation-mediated plasticity would be expected if the applied shear stress becomes greater than the critical shear stress, as such either $\sigma_a/\sigma_\infty \geq 1$ or $0.5 < \sigma_a/\sigma_\infty < 1$, having regard to the fact of grain size, however, in the present case for the 100 nm sample, the reduced stress parameter has been calculated as 0.0995 (see Table 4.1) which is interestingly lower than 0.5. It can be inferred that the model applied to Au-Au contact is in accordance with the results for thinner samples presented in this thesis since more stable microstructures within the refined grains have been reached at the end of the process. Nonetheless, for the non-mixing case, although the result shows a dislocation-mediated deformation and high friction in the map (Figure 4.3), the value for the reduced stress parameter is less than the threshold value. The discrepancy might stem from the fact that our material system consists of Au and Ni and the counter body is ruby instead of a pure metallic contact, which would indeed lead to higher stresses on metallic multilayer surfaces through the hard ceramic sphere. Moreover, the large difference in the stacking fault energies of Au (γ_{sf} = 45 mJ/m^2) and Ni (γ_{sf} = 128 mJ/m^2) cannot allow us for determining an exact value of the γ_{sf} for the shear-mixed Au-Ni alloy in thinner samples, as well as for the Au-Ni composite system in the case of 100 nm sample. Thus, we averaged these values as the main data point on the graph in Figure 4.3 whereas we used

the individual values of Au and Ni as the error bars (see Table 4.1), and since the γ_{sf} contributes to the calculations of parameters on the x-y axes, the large difference between error bars was inevitable. However, no discrepancy in the meaning of dominant deformation mechanism has been observed (a slight shift might only be expected), which I do consider quite significant for the purpose of testing of the model on our experimental observations.

5 Conclusions

By performing sliding experiments with carefully prepared Au-Ni multilayer samples under well-defined UHV conditions as well as under controlled N_2 atmosphere, it has been shown that the initial layer thickness of Au-Ni multilayer systems has a strong impact on the resulting friction force due to the distinctive microstructure evolution close to the surface. A significant increase of the COF with increasing layer thickness has been found in both cases. It was also shown that the effects of ambient conditions are undeniable. In particular I performed the following experiments and reached several conclusions:

- Au-Ni metallic multilayer systems with different interlayer spacing have been carefully prepared via magnetron sputtering in order to systematically study the influence of their initial microstructures on friction behavior. The control of the parameters such as hardness, thickness and surface roughness of thin films have been carefully taken into account. The crystallographic features of the multilayers have been identified via XRD analysis in which the presence of Au(111) crystallographic planes and possible Ni(111) planes which have similar diffraction angle with the (200) order of Au has been confirmed. To characterize the topography of the as-grown multilayer samples and to evaluate the effect of layer thickness on surface roughness, AFM experiments have been carried out and it has been observed that the roughness increases only slightly with increasing layer thickness. Moreover, the hardness of the multilayer samples has been measured via nanoindentation by observing that an increase in the layer thickness leads to decrease in hardness of the multilayers.

- Friction experiments performed on the Au-Ni multilayer samples under ultrahigh vacuum (UHV) conditions are reported in this thesis. It has been observed that the individual layer thickness of multilayer systems has a strong influence on friction behavior due to the transition in the dominant deformation mechanism near the surface. Fully mixed structure (shear-induced AuNi alloy) between Au and Ni layers of the 10 nm and 20 nm samples (corresponding to the lowest observed friction forces) has been obtained while a partially mixed; Au rich layer has been formed when increasing the layer thickness of the multilayer system to 50 nm. When further increasing the layer thickness (100 nm), rather than a partially or fully mechanical mixing, the thinning of the uppermost Au layer eventuated by plowing and accumulating some Au at the end of the wear track was found. Within the scope of the relevant theoretical background, deformation mechanisms associated with the friction force and the grain size [87] has carefully been investigated. With the formation of ultrafine grains by mechanical mixing (fully or partially), the number of grain boundaries strongly increased and grain boundary-mediated deformation resulted in the low friction coefficient for thinner multilayer samples. On the other side, dislocation-mediated deformation has been considered to be dominant in the 100 nm multilayer sample in which higher friction has been obtained. The possible transition from the partial dislocation- to grain boundary-mediated deformation during sliding of the 50 nm sample (in which the vortex-like structures formed) has also been addressed referring to the origin of the theory by Yamakov et al. [107].
- Friction experiments performed on the Au-Ni multilayer samples in N_2 atmosphere have also been reported in this thesis. Environmental

change from an UHV chamber to a glove box filled with N_2 had an impact on friction towards increasing the COF. The COF values of each multilayer sample were larger than the ones observed under UHV conditions; except the 100 nm sample for the last sliding cycles (up to the last 20 cycles), which is fairly similar for both cases. Much gentler wear has been found for the multilayers sheared in N_2 environment, which caused to the observation of different deformation levels. With regard to the microstructural analysis under N_2 environment, in contrast with the UHV results, no mixing behavior has been observed between the Au and Ni layers for thinner multilayer samples. While the deformation of the uppermost Au layers has arisen from plowing the material throughout sliding, material transfer from other areas in contact has also been observed occasionally (which contributes to the thickening of the tribolayer), whereas subsequent layers have been unaffected for all samples. For the 10 nm sample, the localized stresses have led to originating severance of the tribolayer.

- With increasing sliding cycles, i.e. up to 1000 reciprocating cycles, the number of fully-mixed layers has been increased in the 10 nm sample under UHV conditions and severe breaking off of the mixed zone, which raised the mean COF of the multilayer system, has been observed whereas the 100 nm sample showed similarity in terms of deformation of the uppermost Au layer. In this case lower friction force has been observed.

6 Outlook

Throughout this thesis, the results of a systematic experimental study aimed to investigate the dependence of metallic friction on the initial microstructure by utilizing an Au-Ni multilayer model alloy have been presented. Multilayer samples with different interlayer spacing have been analyzed under UHV conditions as well as N_2 atmosphere and it has been found that there is a regime of high friction when the interlayer spacing is large and low friction when it is small. Remarkably, a newly shear-induced phase, which can be interpreted as an AuNi alloy and does not exist in the phase diagram of Au and Ni [138], has been observed in the experiments under UHV conditions. With increasing sliding cycles, 60-65% Ni in Au has also been found only altering the number of fully-mixed layers. On the other hand, change in the environment has led to the different microstructural evolution coupled with the dissimilar friction behavior.

Above all, friction and wear are made responsible for approximately 30% of the energy losses in transportation and machinery. Therefore, a better understanding of these losses and strategies to reduce them even so slightly can have a huge economic impact and is contributing to the efforts to reduce future climate goals. The comprehensive, systematic experimental study on Au-Ni multilayer model alloy presented in this thesis has supported this claim, providing a new route for lowering the friction force of metallic material systems in dry contact by introducing more stable microstructures and alloy formation (fully mixing) in a clean environment (i.e. UHV conditions). Since the experimental studies are restricted based on forming a thermodynamically stable AuNi alloy structure because of the immiscibility of this metal pair under normal circumstances, it is curiously enough that under shear it appears to be possible to form a metastable AuNi alloy. Thereby, the experimental method under UHV conditions described in this thesis would be offered an alternative route to the formation of metastable AuNi alloy, in addition to the one produced via pulsed laser irradiation of colloidal nanoparticles in [143].

The influence of environment on friction and wear of the metals is of general interest for the tribologists, due to the susceptibility of the metals to the contaminants which can be adsorbed from the environment and modify the structure of the contact faces [9, 10]. To that end, the experiments carried out on the multilayer model alloy system in a controlled N_2 atmosphere have made contribution to this hypothesis by the evolution of different microstructures in comparison to that observed in UHV. Although we tried abstaining from ambient conditions as far as possible, we also learned that the relative humidity of the environment (2-5%) and the reactive gases in small quantities (<10-40 ppm) such as H_2O and O_2, or the other complexes such as hydrocarbons can have a substantial influence on friction and wear, corresponding with the microstructure. Therefore, further tribological investigations of the model alloy systems in operating conditions (i.e. in ambient) would be of critical importance.

Both experiments and simulation studies have shown that the deformation behavior of metallic materials is still needed to be elaborated. We thus believe that the analysis of our experimental observations by a proposed theory is worth to consider in regard to shedding light on developing the truest deformation mechanism model of the nanocrystalline metallic multilayer materials.

Within this context, I hope that our experiments will pave the way towards a better understanding of friction from a fundamental point of view and also lead to further developments of very low-friction material systems for many technical applications.

Bibliography

[1] Di Toro, G., Niemeijer, A., Tripoli, A., Nielsen, S., et al., From field geology to earthquake simulation: a new state-of-the-art tool to investigate rock friction during the seismic cycle (SHIVA), *Rend. Fis. Acc. Lincei* **21**, 95-114 (2010).

[2] Bogue, R., Recent developments in MEMS sensors: a review of applications, markets and technologies, *Sensor Review* **33**, 300-304 (2013).

[3] Urbakh, M., Klafter, J., Gourdon, D. and Israelachvili, J., The nonlinear nature of friction. *Nature* **430**, 525–528 (2004).

[4] Holmberg, K., Andersson, P., and Erdemir, A., Global energy consumption due to friction in passenger cars, *Tribol. Int.* **47**, 221–234 (2012).

[5] Freivalds, A., Biomechanics of the upper limbs, Mechanics, Modeling and Musculoskeletal Injuries (2nd edition), *CRC Press*, Boca Raton (2011).

[6] Kwak, J.-S. and Kim, T.-W., A review of adhesion and friction models for gecko feet, *International journal of precision engineering and manufacturing* **11**, 171-186 (2010).

[7] Ethier, C. R. and Simmons, C. A., Introductory biomechanics from cells to organisms, *Cambridge texts in biomedical engineering - Cambridge university press,* Cambridge (2007).

[8] Hough, W., Aboriginal fire-making, *American Anthropologist* **3(4)**, 359-372, (1890).

[9] Hutchings, I. and Shipway, P., Tribology: Friction and wear of engineering materials, Elsevier, Cambridge (2017).

[10] Bhushan, B., Introduction to tribology, Wiley, New York (2013).

[11] Nosonovsky, M., Oil as a lubricant in the ancient middle east, *Tribol. Online* **2(2)**, 44-49 (2007).

[12] Da Vinci, L., Codex Atlanticus, Biblioteca Ambrosiana, Milan, Italy, (1478-1518).

[13] Da Vinci, L., Codex Arundel, British Museum, London, UK, (1478-1518).

[14] Amontons, G., De la resistance causee dans les machines, Memoires de l'Académie des Sciences, Paris, (1699).

[15] Dowson, D., History of tribology, Longman Inc., New York, 153-167 (1979).

[16] Coulomb, C.A., Théorie des machines simples, en ayant égard au frottement de leurs parties, et a la roideur des cordages, Mem. de Math. et de Phys., Paris, (1779).

[17] Persson, B. N. J., Sliding friction, physical principles and applications, Springer-Verlag Berlin, Heidelberg (1998).

[18] Bowden, F.P. and Tabor, The nature of sliding and the analysis of friction, *Proc. Roy. Soc. A* **169**, 391-412 (1938).

[19] Bhushan, B., Israelachvili J. N., and Landman, U., Nanotribology: friction, wear and lubrication at the atomic scale, *Nature* **374**, 607-616 (1995).

[20] Mate, C. M., Tribology on the small scale: A bottom up approach to friction, lubrication, and wear," Oxford University Press, Oxford, (2008).

[21] Tabor, D., and Winterton, R. H. S., The direct measurement of normal and retarded van der Waals forces, *Proc. R. Soc. A* **312**, 435-450 (1969).

[22] Binnig, G., Quate, C. F. and Gerber, C., Atomic force microscope, *Physical Review Letters* **56**, 930–933 (1986).

[23] Mate, C. M., Mcclelland, G. M., Erlandsson, R., and Chiang, S., Atomic-scale friction of a tungsten tip on a graphite surface, *Physical Review Letters* **59**, 1942–1945 (1987).

[24] Hölscher, H., Schwarz, U. D., Zwörner, O., and Wiesendanger, R., Consequences of the stick-slip movement for the scanning force microscopy imaging of graphite, *Physical Review B* **57**, 2477-2482 (1998).

[25] Dienwiebel, M., Verhoeven, G. S., Pradeep, N., Frenken, J. W. M., Heimberg J. A., and Zandbergen, H. W., Superlubricity of graphite, *Physical Review Letters* **92**, 126101-1-4 (2004).

[26] Schwarz, U. D., Allers, W., Gensterblum, G., and Wiesendanger, R., Low-load friction behavior of epitaxial C 60 monolayers under Hertzian contact, *Physical Review B* **52**, 14976-14984 (1995).

[27] Putman, C. A. J., Igarashi, M., and Kaneko, R., Single-asperity friction in friction force microscopy: the composite-tip model, *Applied Physics Letters* **66**, 3221-3223 (1995).

[28] Schwarz, U. D., Köster, P., and Wiesendanger, R., Quantitative analysis of lateral force microscopy experiments, *Review of Scientific Instruments* **67**, 2560-2567 (1996).

[29] Meyer, E., Lüthi, R., Howald, L., Bammerlin, M., Guggisberg, M., and Güntherodt, H. J. Site-specific friction force spectroscopy, *Journal of Vacuum Science & Technology B* **14**, 1285-1288 (1996).

[30] Schwarz, U.D., Zwörner, O., Köster, P., and Wiesendanger, R., Quantitative analysis of the frictional properties of solid materials at low loads. I. Carbon compounds, *Phys. Rev. B* **56**, 6987-6996 (1997).

[31] Schwarz, U.D., Zwörner, O., Köster, P., and Wiesendanger, R., Quantitative analysis of the frictional properties of solid materials at low loads. II. Mica and germaniumsulfide, *Phys. Rev. B* **56**, 6997-7000 (1997).

[32] Enachescu, M., van den Oetelaar, R. J. A., Carpick, R. W., Ogletree, D. F., Flipse, C. F. J., and Salmeron, M., Atomic force microscopy study of an ideally hard contact: The diamond(111)/tungsten carbide interface, *Phys. Rev. Lett.* **81**, 1877-1880 (1998).

[33] Carpick, R. W., and Salmeron, M., Scratching the surface: Fundamental investigations of tribology with atomic force microscopy, *Chemical Reviews* **97**, 1163-1194 (1997).

[34] Sundararajan, S., and Bhushan, B., Topography-induced contributions to friction forces measured using an atomic force/friction force microscope, *Journal of Applied Physics* **88**, 4825-4831 (2000).

[35] Müser, M. H., Wenning, L., and Robbins, M. O., Simple microscopic theory of Amontons' laws for static friction, *Physical Review Letters* **86**, 1295-1298 (2001).

[36] Wenning, L., and Müser, M. H., Friction laws for elastic nanoscale contacts, *Europhys. Lett.* **54(5)**, 693-699 (2001).

[37] Garcia, R., and Perez, R., Dynamic atomic force microscopy methods, *Surface Science Reports* **47**, 197-301 (2002).

[38] Hölscher, H., Schirmeisen, A., and Schwarz, U. D., Principles of atomic friction: from sticking atoms to superlubric sliding, *Phil. Trans. R. Soc. A* **366**, 1383-1404 (2008).

[39] Szlufarska, I., Chandross, M., and Carpick, R. W., Recent advances in single-asperity nanotribology, *Journal of Physics D: Applied Physics* **41**, 123001-39 (2008).

[40] Li, Q. Y., Dong, Y. L., Martini, Y. L., and Carpick, R. W., Atomic friction modulation on the reconstructed Au (111) surface, *Tribology Letters* **43**, 369-378 (2011).

[41] Baykara, M. Z., Schwendemann, T., Albers, B., Pilet, N., Mönig, H., Altman, E., Schwarz, U. D., Exploring atomic-scale lateral forces in the attractive regime: A case study on graphite (0001), *Nanotechnology* **23**, 405703-405709 (2012).

[42] Bennewitz, R., Hausen, F., and Gosvami, N. N., Nanotribology of clean and modified gold surfaces, *Journal of Materials Research* **28**, 1279-1288 (2013).

[43] Ritter, C., Baykara, M. Z., Stegemann, B., Heyde, M., Rademann, K., Schroers J., and Schwarz, U. D., Nonuniform friction-area dependency for antimony oxide surfaces sliding on graphite, *Physical Review B* **88**, 045422-1-6 (2013).

[44] Dietzel, D., Feldmann, M., Schwarz, U. D., Fuchs, H., and Schirmeisen, A., Scaling laws of structural lubricity, *Physical Review Letters* **111**, 235502-1-5 (2013).

[45] Cihan, E., Özoğul, A., and Baykara, M. Z., Structure and nanotribology of thermally deposited gold nanoparticles on graphite, *Applied surface science* **354B**, 429-436 (2015).

[46] Cihan, E., Ipek, S., Durgun, E., and Baykara, M.Z., Structural lubricity under ambient conditions, *Nature communications* **7**, 12055-1-6 (2016).

[47] Vanossi, A., Dietzel, D., Schirmeisen, A., Meyer, E., et al., Recent highlights in nanoscale and mesoscale friction, *Beilstein Journal of Nanotechnology* **9(1)**, 1995-2014 (2018).

[48] Hertz, H., Ueber die Beruhrung fester elastischer Korper, *J. Reine Angew. Math.* **92**, 156-171 (1882).

[49] Johnson, K. L., Kendall, K., and Roberts, A. D., Surface energy and the contact of elastic solids, *Proc. R. Soc. A* **324**, 301-313 (1971).

[50] Muller. V. M., Derjaguin, B. V., and Toporov, Y. U. P., Effect of contact deformations on the adhesion of particles, *J. Colloid Interface Sci.* **53**, 314-326 (1975).

[51] Derjaguin, B. V., Muller. V. M., and Toporov, Y. U. P., On two methods of calculation of the force of sticking of an elastic sphere to a rigid plane, *J. Colloids and Surfaces* **7**, 251-259 (1983).

[52] Maugis, D., Adhesion of spheres: the JKR-DMT transition using a Dugdale model, *J. Colloid Interface Sci.* **150**, 243-269 (1992).

[53] Hamilton, G. M., and Goodman, L. E., Stress field created by a circular sliding contact, *J. Appl. Mech.* **33(2)**, 371-376 (1966).

[54] Hamilton, G. M., Explicit equations for the stresses beneath a sliding spherical contact, *Proc. Inst Mech. Eng. C* **197**, 53-59 (1983).

[55] Greenwood, J. A. and Williamson, J. B. P., Contact of nominally flat rough surfaces, *Proc. Roy. Soc. Lond. A.* **295**, 300-319 (1966).

[56] Rigney, D. A., Transfer, mixing and associated chemical and mechanical processes during the sliding of ductile materials, *Wear* **245**, 1-9 (2000).

[57] Scherge, M., Shakhvorostov, D., and Pöhlmann, K., Fundamental wear mechanism of metals, *Wear* **255**, 395–400 (2003).

[58] Dienwiebel, M., and Pöhlmann, K., Nanoscale evolution of sliding metal surfaces during running-in, *Tribology Letters* **27(3)**, 255–260 (2007).

[59] Godet, M., The third-body approach: A mechanical view of wear, *Wear* **100**, 437–452 (1984).

[60] Sawa, M., and Rigney, D. A., Sliding behavior of dual phase steels in vacuum and in air, *Wear* **119**, 369-390 (1987).

[61] Fischer, A., Sub-surface microstructural alterations during sliding wear of biomedical metals. Modelling and experimental results, *Computational Materials Science* **46(3)**, 586-590 (2009).

[62] Rupert, T. J., and Schuh, C. A., Sliding wear of nanocrystalline Ni-W-Structural evolution and the apparent breakdown of Archard scaling, *Acta Materialia* **58**, 4137–4148 (2010).

[63] Prasad, S. V., Battaile, C. C., and Kotula, P. G., Friction transitions in nanocrystalline nickel, *Scripta Materialia* **64**, 729-732 (2011).

[64] Padilla, H. A., Boyce, B. L., Battaile, C. C., and Prasad, S. V., Frictional performance and near surface evolution of nanocrystalline Ni-Fe as governed by contact stress and sliding velocity, *Wear* **297**, 860-871 (2013).

[65] Feser, T., Stoyanov, P., Mohr, F., and Dienwiebel, M., The running-in mechanisms of binary brass studied by in-situ topography measurements, *Wear* **303**, 465–472 (2013).

[66] Stoyanov, P., Merz, R., Romero, P. A., Wählisch F. C., et al., Surface softening in metal–ceramic sliding contacts: An experimental and numerical investigation, *ACS Nano* **9(2)**, 1478-1491 (2015).

[67] Linsler, D., Schröckert, F., and Scherge, M., Influence of sub-surface plastic deformation on the running-in behavior of a hypoeutectic AlSi alloy, *Tribology International* **100**, 224-230 (2016).

[68] Chen, X., Han, Z., Li, X., and Lu, K., Lowering coefficient of friction in Cu alloys with stable gradient nanostructures, *Science Advances* **2**, 1601942-1-7 (2016).

[69] Greiner, C., Liu, Z., Strassberger, L., and Gumbsch, P., Sequence of stages in the microstructure evolution in copper under mild reciprocating tribological loading, *ACS Applied Materials & Interfaces* **8**, 15809-15819 (2016).

[70] Brink, A., Lichtenberg, K., and Scherge, M., The influence of the initial near-surface microstructure and imposed stress level on the running-in characteristics of lubricated steel contacts, *Wear* **360-361**, 114-120 (2016).

[71] Rigney, D. A., and Karthikeyan, S., The evolution of tribomaterial during sliding: A brief introduction, *Tribology Letters* **39**, 3-7 (2010).

[72] Chandross, M., Curry, J. F., Babuska, T. F., Lu, P., Furnish, T.A., et al., Shear-induced softening of nanocrystalline metal interfaces at cryogenic temperatures, *Scripta Materialia* **143**, 54-58 (2018).

[73] Suh, N. P., and co-workers, The delamination theory of wear, *Elsevier Sequoia*, Lausanne (1977).

[74] Beckmann, N., Romero, P. A., Linsler, D., Dienwiebel, M., et al., Origins of folding instabilities on polycrystalline metal surfaces, *Physical Review Applied* **2**, 064004-1-7 (2014).

[75] Stoyanov, P., Romero, P. A., Järvi, T. T., Pastewka, L., Scherge, M., Stemmer, P., et al., Experimental and numerical atomistic investigation of the third-body formation process in dry tungsten/tungsten-carbide tribo couples, *Tribol Lett* **50(1)**, 67-80 (2013).

[76] Subramanian, K., Wu, J. H., and Rigney, D. A., The role of vorticity in the formation of tribomaterial during sliding, *Materials Research Society Proceedings* **821**, 9.6.1–9.6.6 (2004).

[77] Luo, Z. P., Zhang, G. P., and Schwaiger, R., Microstructural vortex formation during cyclic sliding of Cu/Au multilayers, *Scripta Materilia* **107**, 67-70 (2015).

[78] Pouryazdan, M., Kaus, B. J. P., Rack, A., Ershov, A., and Hahn, H., Mixing instabilities during shearing of metals, *Nature Communications* **8**, 1611 (2017).

[79] Kim, H. J., Karthikeyan, S., and Rigney, D., A simulation study of the mixing, atomic flow and velocity profiles of crystalline materials during sliding, *Wear* **267**, 1130-1136 (2009).

[80] Kim, H. J., Kim, W. K., Falk, M. L., and Rigney, D. A., MD simulations of microstructure evolution during high-velocity sliding between crystalline materials, *Tribol lett* **28**, 299-306 (2007).

[81] Karthikeyan, S., Agrawal, A., and Rigney, D. A., Molecular dynamics simulations of sliding in an Fe–Cu tribopair system, *Wear* **267**, 1166-1176 (2009).

[82] Hall, E. O., The Hall-Petch Relationship, *Proc. Phys. Soc. Ser. B*. **64**, 474 (1951).

[83] Benjamin J. S., and Volin, T. E., The mechanism of mechanical alloying, *Metallurgical Transactions* **5**, 1929-1934 (1974).

[84] Schuh, C. A., Nieh, T. G., and Yamasaki, T., Hall–Petch breakdown manifested in abrasive wear resistance of nanocrystalline nickel, *Scripta Materialia* **46**, 735–740 (2002).

[85] Meyers, M. A., Mishra, A., and Benson, D. J., Mechanical properties of nanocrystalline materials, *Progress in Materials Science* **51**, 427–556 (2006).

[86] Argibay, N., Furnish, T. A., Boyce, B. L., Clark, B. G., and Chandross, M., Stress-dependent grain size evolution of nanocrystalline Ni-W and its impact on friction behavior, *Scripta Materialia* **123**, 26–29 (2016).

[87] Argibay, N., Chandross, M., Cheng, S., and Michael, J. R., Linking microstructural evolution and macro-scale friction behavior in metals, *J Mater Sci* **52**, 2780-2799 (2017).

[88] Rigney, D. A., Chen, L. H., Naylor, M. G. S., and Rosenfield, A.R., Wear processes in sliding systems, *Wear* **100 (1-3)**, 195-219 (1984).

[89] Odunuga, S., Li, Y., Krasnochtchekov, P., Bellon, P., and Averback, R. S., Forced chemical mixing in alloys driven by plastic deformation, *Physical Review Letters* **95**, 045901-1-4 (2005).

[90] Ma, E., He, J. H., and Schilling, P. J., Mechanical alloying of immiscible elements: Ag-Fe contrasted with Cu-Fe, *Phys. Rev. B* **55**, 5542-5545 (1997).

[91] Xu, J., Herr, U., Klassen, T., and Averback, R. S., Formation of supersaturated solid solutions in the immiscible Ni–Ag system by mechanical alloying, *J. Appl. Phys.* **79**, 3935-3945 (1996).

[92] Cihan E., Störmer, H., Leiste, H., Stüber, M., and Dienwiebel, M., Low friction of metallic multilayers by formation of a shear-induced alloy, submitted to *Scientific Reports* (2019).

[93] Bowden, F. P., and Tabor, D., Mechanism of metallic friction, *Nature* **150**, 197-199 (1942).

[94] Bowden, F. P., and Tabor, D., The friction and lubrication of solids, Clarendon Press, Oxford (1950).

[95] Scharf, T. W., and Prasad, S. V., Solid lubricants: A review, *J. Mater. Sci.* **48(2)**, 511–531 (2013).

[96] Wen, M., Wen, C., Hodgson, P. D., and Li, Y. C., Tribological behaviour of pure Ti with a nanocrystalline surface layer under different loads, *Tribol. Lett.* **45**, 59–66 (2012).

[97] Farhat, Z. N., Ding, Y., Northwood, D. O., and Alpas, A. T., Effect of grain size on friction and wear of nanocrystalline aluminum, *Mater. Sci. Eng. A* **206**, 302–313 (1996).

[98] Zhang, Y. S., Han, Z., Wang, K., and Lu, K., Friction and wear behaviors of nanocrystalline surface layer of pure copper, *Wear* **260**, 942–948 (2006).

[99] Chen, X., Han, Z., and Lu, K., Enhancing wear resistance of Cu–Al alloy by controlling sub-surface dynamic recrystallization, *Scr. Mater.* **101**, 76–79 (2015).

[100] Ren, F., Arshad, S. N., Bellon, P., Averback, R. S., et al., Sliding wear induced chemical nanolayering in Cu–Ag, and its implications for high wear resistance, *Acta Mater.* **72**, 148–158 (2014).

[101] Shakhvorostov, D., Pohlmann, K., and Scherge, M., Structure and mechanical properties of tribologically induced nanolayers, *Wear* **260**, 433–437 (2006).

[102] Linsler, D., Schlarb, T., Weingartner, T., and Scherge, M., Influence of sub-surface microstructure on the running-in of an AlSi alloy, *Wear* **332–333**, 926–931 (2015).

[103] Stoyanov, P., Stemmer, P., Järvi, T. T., Merz, R., et al., Friction and wear mechanisms of tungsten–carbon systems: A comparison of dry and lubricated conditions, *ACS Appl. Mater. Interfaces* **5**, 6123–6135 (2013).

[104] Kato, K., Wear in relation to friction-A review, *Wear* **241**, 151–157 (2000).

[105] Van Swygenhoven, H., Derlet, P. M., and Hasnaoui, A., Atomic mechanism for dislocation emission from nanosized grain boundaries, *Phys Rev B* **66**, 024101-1-8 (2002).

[106] Van Swygenhoven, H., and Derlet, P. M., Grain-boundary sliding in nanocrystalline fcc metals, *Phys Rev B* **64**, 224105-1-9 (2001).

[107] Yamakov, V., Wolf, D., and Phillpot, S. R., Mukherjee, A. K., and Gleiter, H., Deformation-mechanism map for nanocrystalline metals by moleculardynamics simulation, *Nature Materials* **3**, 43–47 (2004).

[108] Gosvami, N. N., Feldmann, M., Peguiron, J., Moseler, M., et al., Ageing of a microscopic sliding gold contact at low temperatures, *Physical Review Letters* **107**, 144303-1-5 (2011).

[109] Buckley, D. H., Surface Effects in Adhesion, Friction, Wear and Lubrication, Tribology series no. 5, *Elsevier*, Amsterdam (1981).

[110] Rigney, D. A., Large strains associated with sliding contact of metals, *Mat. Res. Innovat.* **1**, 231-234 (1998).

[111] Donnet, C., and Erdemir, A., Historical developments and new trends in tribological and solid lubricant coatings, *Surface and Coatings Technology* **180–181**, 76-84 (2004).

[112] Springer, R. W. and Catlett, D. S., Structure and mechanical properties of Al/AlxOy vacuum deposited laminates, *Thin Solid Films* **54**, 197–205 (1978).

[113] Bunshah, R. F., Nimmagadda, R., Doerr, H. J., Movchan, B. A., Grechanuk, N. I. and Didkin, G. G., Structure–property relationships in Cr/Cu and Ti/Ni microlaminate composites, *Thin Solid Films* **112**, 227–236 (1984).

[114] Barnett, S. A., Deposition and mechanical properties of superlattice thin Films, *Physics of thin films* **17**, 1-77 (1993).

[115] Holleck, H., Material selection for hard coatings, *Journal of Vacuum Science and Technology A* **4**, 2661–2669 (1984).

[116] Holleck, H. and Schier, V., Multilayer PVD coatings for wear protection, *Surface and Coatings Technology* **76–77**, 328–336 (1995).

[117] Holmberg, K., Matthewst, A., and Ronkainen, H., Coatings tribology-contact mechanism and surface design, *Tribology international* **31**, 107-120 (1998).

[118] Podgornik, B., and Vizintin, J., Tribology of thin films and their use in the field of machine elements, *Vacuum* **68**, 39–47 (2003).

[119] Misra, A., Hirth, J.P., and Hoagland, R.G., Length-scale-dependent deformation mechanisms in incoherent metallic multilayered composites *Acta Mater.* **53**, 4817-4824 (2005).

[120] Kelly, P. J., and Arnell R. D., Magnetron sputtering: a review of recent developments and applications, *Vacuum* **56** 159-172 (2000).

[121] Smith, W.F. and Hashemi, J., Foundations of materials science and engineering (4th edition), *Mc Graw Hill International Edition*, Ch. 3: 105-112, New York (2006).

[122] Bragg, W.H., and Bragg, W.L., The reflexion of X-rays by crystals, *Proc. R. Soc. Lond. A.* **88**, 428-38 (1913).

[123] Eaton, P. J. and West, P., Atomic force microscopy, *Oxford University Press*, Oxford (2010).

[124] Bhushan, B., Springer Handbook of Nanotechnology, *Springer-Verlag Berlin*, Heidelberg (2004).

[125] Fischer-Cripps A. C., Nanoindentation (3rd edition), *Mechanical Engineering Series-Springer*, Ch. 2: 21-37, New York (2011).

[126] Pharr, G. M., Measurement of mechanical properties by ultra-low load indentation, *Materials Science and Engineering A* **253**, 151-159 (1998).

[127] Wang, H., and Linford, M.R., X-ray photoelectron spectroscopy and auger electron spectroscopy: Comparison and basic principles, *Vacuum Technology & Coating*, (March 2015).

[128] Marchetto D., UHV tribometer manual, *Fraunhofer IWM* (2012).

[129] Scherge, M., and Gorb, S.N., Using biological principles to design MEMS, *Journal of Micromechanics and Microengineering* **10(3)**, 359-364 (2000).

[130] Farrell, C. T., and Player, M. A., Phase step measurement and variable step algorithms in phase-shifting interferometry, *Meas. Sci. Technol.* **3**, 953-958 (1992).

[131] Giannuzzi, L.A., and Stevie, F.A., A review of focused ion beam milling techniques for TEM specimen preparation, *Micron* **30(3)**, 197-204 (1999).

[132] Smith, W.F., and Hashemi, J., Foundations of materials science and engineering (4th edition), *Mc Graw Hill International Edition*, Ch. 4: 158-161, New York (2006).

[133] Sneddon G. C., Trimby, P. W., and Cairney, J. M., Transmission Kikuchi diffraction in a scanning electron microscope: A review, *Materials Science and Engineering R* **110**, 1–12 (2016).

[134] http://www.rsc.org/periodic-table/element/79/gold
(visited on 30.11.18)

[135] Hammer, B., and Norskov, J. K., Why gold is the noblest of all the metals, *Nature* **376**, 238-240 (1995).

[136] http://www.rsc.org/periodic-table/element/28/nickel
(visited on 30.11.18)

[137] Baldwin, W.H., The story of nickel - I. How "old Nick's" gnomes were outwitted, *Journal of Chemical Education* **8(9)**, 1749 (1931).

[138] Koziorowska, J.S., Grzanka, S., Litwin-Staszewska, E., Piotrzkowski, R., et al., Ni–Au contacts to p-type GaN – Structure and properties, *Solid State Electronics* **54(7)**, 701-709 (2010).

[139] Raynor, G.V., The alloying behaviour of gold, *Gold Bulletin: The Journal of Gold Science, Technology and Applications* **9(1)**, 12-19 (1976).

[140] Scherrer, P., Nachrichten von der Gesellschaft der Wissenschaften zu Göttingen, *Mathematisch-Physikalische Klasse* **2**, 98-100 (1918).

[141] Jankowski, A. F., Superhardness effect in Au/Ni multilayers, *Journal of Magnetism and Magnetic Materials* **126**, 185-191 (1993).

[142] Zhou, X., Jiang, Z., Wang, H., and Yu, R., Investigation on methods for dealing with pile-up errors in evaluating the mechanical properties of thin metal films at sub-micron scale on hard substrates by nanoindentation technique, *Materials Science and Engineering A* **488**, 318-332 (2008).

[143] Swiatkowska-Warkocka, Z., Pyatenko, A., Krok, F., Jany, B. R., and Marszalek, M., Synthesis of new metastable nanoalloys of immiscible metals with a pulse laser technique, *Scientific Reports* **5**, 09849-1-6 (2016).

[144] Foiles, S. M., Baskes, M. I., and Daw, M. S., Embedded-atom-method functions for the fcc metals Cu, Ag, Au, Ni, Pd, Pt, and their alloys, *PRB* **33**, 7983-7991 (1986).

[145] Porter, D. A., and Easterling, K. E., Phase transformations in metals and alloys, *Springer-Science+Business Media, B.Y.* – 2nd Edition, Ch. 3, Boca Raton (1992).

[146] Zener, C., Grains, phases and interfaces: an interpretation of microstructure, *Trans. Am. Inst. Min. Engrs.* **175**, 15-51 (1948).

[147] Gladman, T., On the theory of the effect of precipitate particles on grain growth in metals, *Proc. R. Soc*, **294A**, 298-309 (1966).

[148] Hellman, P. and Hillert, M., Effect of second-phase particles on grain growth, *Scandinavian Journal of Metallurgy* **4**, 211-219 (1975).

[149] Hillert, M., Inhibition of grain growth by second-phase particles, *Acta metallurgica* **36**, 3177-3181 (1988).

[150] Hunderi, O., and Ryum, N., Computer simulation of stagnation in grain growth, *Acta metallurgica* **29**, 1737-1745 (1981).

[151] Hunderi, O., and Ryum, N., On the stagnation of grain growth, *Acta metallurgica* **30**, 739-742 (1982).

[152] Nes, E., Ryum, N., and Hunderi, O., On the Zener drag, *Acta metallurgica* **33**, 11-22 (1985).

[153] Moon, M.W., Jensen, H.M., Hutchinson, J.W., Oh, K.H., and Evans, A.G., The characterization of telephone cord buckling of compressed thin films on substrates, *Journal of the Mechanics and Physics of Solids* **50**, 2355-2377 (2002).

[154] Evans, A.G., and Hutchinson, J.W., On the mechanics of delamination and spalling in compressed films, *International Journal of Solids and Structures* **20**, 455-466 (1984).

[155] Suh, N. P.: Update on the delamination theory of wear – fundamentals of friction and wear of materials. In: Rigney, D. A. (ed.) pp 43-71. *ASM*, Pittsburgh (1981).

[156] Léger, J. M., Haines, J., Schmidt, M., Petitet, J. P., Pereira A. S., da Jornada, J. A. H., Discovery of hardest known oxide, *Nature* **383**, 401 (1996).

[157] Gioia, G., and Ortiz, M., Delamination of compressed thin films, *Advances in Applied Mechanics* **33**, 119-192 (1997).

[158] Schildbach, M.A., and Hamza, A.V., Clean and water-covered sapphire (1102) surfaces: structure and laser-induced desorption, *Surface Science* **282**, 306-322 (1993).

[159] Krim, J., Dash, J.G., and Suzanne, J., Triple-point wetting of light molecular gases on Au (111) surfaces, *PRL* **52**, 640-643 (1084).

[160] Wickham, D.T., Banse, B.A., and Koel, B.E., Adsorption of nitrogen dioxide on polycrystalline gold, *Catalysis Letters* **6**, 163-172 (1990).

[161] Bartram, M.E., and Koel, B.E., The molecular adsorption of NO_2 and the formation of N_2O_3 on Au (111), *Surface Science* **213**, 137-156 (1989).

[162] Yip, S., The strongest size, *Nature* **391,** 532-533 (1998).

[163] Schiøtz, J., Di Tolla, F.D., and Jacobsen, K.W., Softening of nanocrystalline metals at very small grain sizes *Nature* **391**, 561–563 (1998).

Appendix Figures

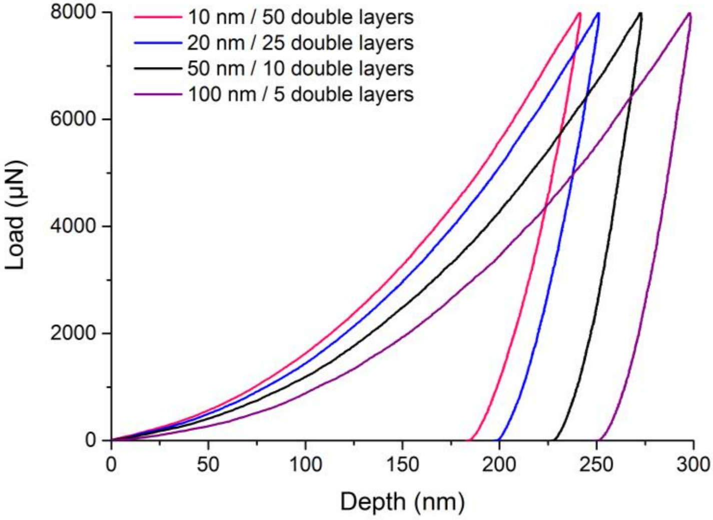

Figure A1: Load-displacement (depth) curves created by the 'Hysitron Ti 950 Triboindenter' (Bruker). A Berkovich type indenter was used in the measurements at an indentation load of 8 mN, which were calibrated according to the load-displacement curves of the standard fused quartz sample.

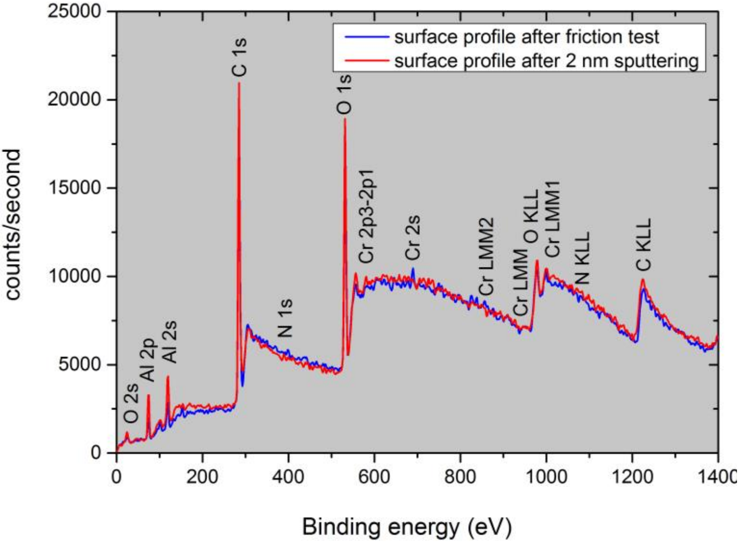

Figure A2: XPS surface profiles of the corresponding ruby ball, as counter body. The blue XPS profileshows the present elements on its surface subsequent to the friction test. Since the ruby ball was exposed to air for the purpose of placing onto a suitable sample holder prior to the XPS analysis, Ar ion milling ≈ 2 nm depth was also applied to remove the residual gases in order to be able to see the Au content if it is already adhered. However, no residual material from the Au-Ni multilayer sample is found on the counter surface.

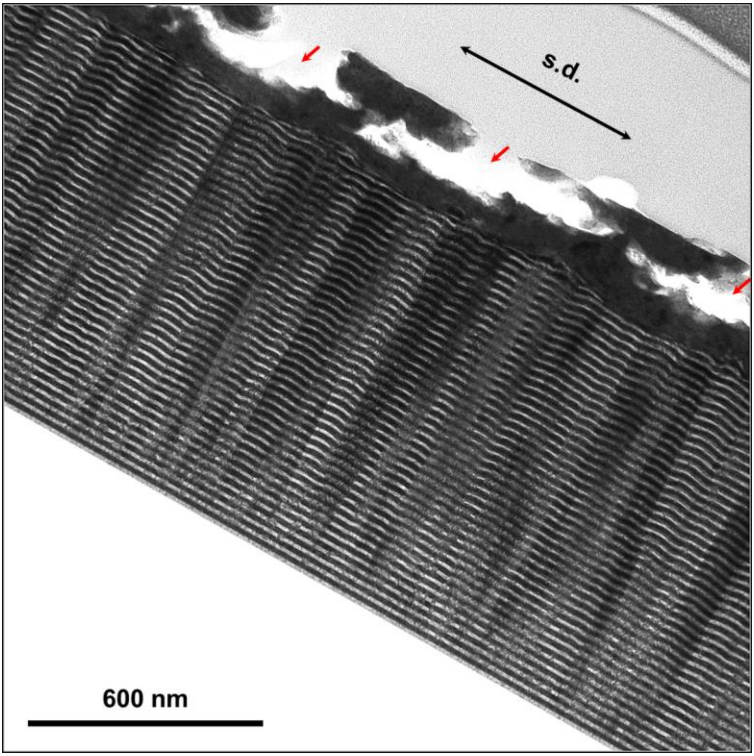

Figure A3: TEM image displaying completely breaking off of the intermixing region for the 10 nm sample after the 1000 cycles of sliding. The fully-mixed, nanocrystalline zone is remarkable at the very surface whereas Ni (light) and Au (dark) layers are separable beneath this region.

Dissemination

Journal publications based on the present dissertation

- Cihan, E.*, Störmer, H., Leiste, H., Stüber, M., and Dienwiebel, M., Low friction of metallic multilayers by formation of a shear-induced alloy, *Scientific Reports* 9, 9480: 1-10 (2019)
- Cihan, E.*, Argibay, N., Chandross, M., and Dienwiebel, M., Effect of environment on microstructure evolution and friction of Au-Ni multilayers, submitted to *Tribology Letters* 68 (1), 30 (2019)

Contributed talk to conferences

- Cihan, E.*, Störmer, H., Leiste, H., Stüber, M., and Dienwiebel, M., Low friction of metallic multilayers by formation of a shear-induced alloy, 7th European Conference on Tribology, Wien, Austria (June 13, 2019)

Contributed posters to conferences

- Cihan, E.*, Störmer, H., and Dienwiebel, M., Low friction of metallic multilayers by formation of a shear-induced alloy, STLE Tribology Frontiers Conference - Tribology, Chicago, Illinois, USA (October 28-31, 2018)
- Cihan, E.*, Störmer, H., and Dienwiebel, M., Low friction of metallic multilayers by formation of a shear-induced alloy, Gordon Research Conference - Tribology, Lewiston, USA (June 24-29, 2018)
- Cihan, E.*, and Dienwiebel, M., Understanding the third-body formation during friction utilizing multilayer model alloys, Gordon

Research Conference - Physical Metallurgy, Biddeford, USA (July 23-28, 2017)

- Cihan, E.*, and Dienwiebel, M., Understanding the third-body formation during friction utilizing multilayer model alloys, 7th European Nanomanipulation Workshop, Jena, Germany (February 20-22, 2017)

Schriftenreihe des Instituts für Angewandte Materialien

ISSN 2192-9963

Band 1 Prachai Norajitra
Divertor Development for a Future Fusion Power Plant. 2011
ISBN 978-3-86644-738-7

Band 2 Jürgen Prokop
Entwicklung von Spritzgießsonderverfahren zur Herstellung von Mikrobauteilen durch galvanische Replikation. 2011
ISBN 978-3-86644-755-4

Band 3 Theo Fett
New contributions to R-curves and bridging stresses – Applications of weight functions. 2012
ISBN 978-3-86644-836-0

Band 4 Jérôme Acker
Einfluss des Alkali/Niob-Verhältnisses und der Kupferdotierung auf das Sinterverhalten, die Strukturbildung und die Mikrostruktur von bleifreier Piezokeramik $(K_{0,5}Na_{0,5})NbO_3$. 2012
ISBN 978-3-86644-867-4

Band 5 Holger Schwaab
Nichtlineare Modellierung von Ferroelektrika unter Berücksichtigung der elektrischen Leitfähigkeit. 2012
ISBN 978-3-86644-869-8

Band 6 Christian Dethloff
Modeling of Helium Bubble Nucleation and Growth in Neutron Irradiated RAFM Steels. 2012
ISBN 978-3-86644-901-5

Band 7 Jens Reiser
Duktilisierung von Wolfram. Synthese, Analyse und Charakterisierung von Wolframlaminaten aus Wolframfolie. 2012
ISBN 978-3-86644-902-2

Band 8 Andreas Sedlmayr
Experimental Investigations of Deformation Pathways in Nanowires. 2012
ISBN 978-3-86644-905-3

Die Bände sind unter www.ksp.kit.edu als PDF frei verfügbar oder als Druckausgabe bestellbar.

Band 9 Matthias Friedrich Funk
Microstructural stability of nanostructured fcc metals during cyclic deformation and fatigue. 2012
ISBN 978-3-86644-918-3

Band 10 Maximilian Schwenk
Entwicklung und Validierung eines numerischen Simulationsmodells zur Beschreibung der induktiven Ein- und Zweifrequenzrandschichthärtung am Beispiel von vergütetem 42CrMo4. 2012
ISBN 978-3-86644-929-9

Band 11 Matthias Merzkirch
Verformungs- und Schädigungsverhalten der verbundstranggepressten, federstahldrahtverstärkten Aluminiumlegierung EN AW-6082. 2012
ISBN 978-3-86644-933-6

Band 12 Thilo Hammers
Wärmebehandlung und Recken von verbundstranggepressten Luftfahrtprofilen. 2013
ISBN 978-3-86644-947-3

Band 13 Jochen Lohmiller
Investigation of deformation mechanisms in nanocrystalline metals and alloys by in situ synchrotron X-ray diffraction. 2013
ISBN 978-3-86644-962-6

Band 14 Simone Schreijäg
Microstructure and Mechanical Behavior of Deep Drawing DC04 Steel at Different Length Scales. 2013
ISBN 978-3-86644-967-1

Band 15 Zhiming Chen
Modelling the plastic deformation of iron. 2013
ISBN 978-3-86644-968-8

Band 16 Abdullah Fatih Çetinel
Oberflächendefektausheilung und Festigkeitssteigerung von niederdruckspritzgegossenen Mikrobiegebalken aus Zirkoniumdioxid. 2013
ISBN 978-3-86644-976-3

Band 17 Thomas Weber
Entwicklung und Optimierung von gradierten Wolfram/EUROFER97-Verbindungen für Divertorkomponenten. 2013
ISBN 978-3-86644-993-0

Die Bände sind unter www.ksp.kit.edu als PDF frei verfügbar oder als Druckausgabe bestellbar.

Band 18 Melanie Senn
Optimale Prozessführung mit merkmalsbasierter Zustandsverfolgung. 2013
ISBN 978-3-7315-0004-9

Band 19 Christian Mennerich
Phase-field modeling of multi-domain evolution in ferromagnetic shape memory alloys and of polycrystalline thin film growth. 2013
ISBN 978-3-7315-0009-4

Band 20 Spyridon Korres
On-Line Topographic Measurements of Lubricated Metallic Sliding Surfaces. 2013
ISBN 978-3-7315-0017-9

Band 21 Abhik Narayan Choudhury
Quantitative phase-field model for phase transformations in multi-component alloys. 2013
ISBN 978-3-7315-0020-9

Band 22 Oliver Ulrich
Isothermes und thermisch-mechanisches Ermüdungsverhalten von Verbundwerkstoffen mit Durchdringungsgefüge (Preform-MMCs). 2013
ISBN 978-3-7315-0024-7

Band 23 Sofie Burger
High Cycle Fatigue of Al and Cu Thin Films by a Novel High-Throughput Method. 2013
ISBN 978-3-7315-0025-4

Band 24 Michael Teutsch
Entwicklung von elektrochemisch abgeschiedenem LIGA-Ni-Al für Hochtemperatur-MEMS-Anwendungen. 2013
ISBN 978-3-7315-0026-1

Band 25 Wolfgang Rheinheimer
Zur Grenzflächenanisotropie von $SrTiO_3$. 2013
ISBN 978-3-7315-0027-8

Band 26 Ying Chen
Deformation Behavior of Thin Metallic Wires under Tensile and Torsional Loadings. 2013
ISBN 978-3-7315-0049-0

Band 27 Sascha Haller
Gestaltfindung: Untersuchungen zur Kraftkegelmethode. 2013
ISBN 978-3-7315-0050-6

Band 28 Nicht erschienen

Band 29 Gunnar Picht
Einfluss der Korngröße auf ferroelektrische Eigenschaften dotierter $Pb(Zr_{1-x}Ti_x)O_3$ Materialien. 2013
ISBN 978-3-7315-0106-0

Band 30 Esther Held
Eigenspannungsanalyse an Schichtverbunden mittels inkrementeller Bohrlochmethode. 2013
ISBN 978-3-7315-0127-5

Band 31 Pei He
On the structure-property correlation and the evolution of Nanofeatures in 12-13.5% Cr oxide dispersion strengthened ferritic steels. 2014
ISBN 978-3-7315-0141-1

Band 32 Jan Hoffmann
Ferritische ODS-Stähle – Herstellung, Umformung und Strukturanalyse. 2014
ISBN 978-3-7315-0157-2

Band 33 Wiebke Sittel
Entwicklung und Optimierung des Diffusionsschweißens von ODS Legierungen. 2014
ISBN 978-3-7315-0182-4

Band 34 Osama Khalil
Isothermes Kurzzeitermüdungsverhalten der hoch-warmfesten Aluminium-Knetlegierung 2618A (AlCu2Mg1,5Ni). 2014
ISBN 978-3-7315-0208-1

Band 35 Nicht erschienen

Band 36 Christoph Hage
Grundlegende Aspekte des 2K-Metallpulverspritzgießens. 2014
ISBN 978-3-7315-0217-3

Band 37 Bartłomiej Albiński
Instrumentierte Eindringprüfung bei Hochtemperatur für die Charakterisierung bestrahlter Materialien. 2014
ISBN 978-3-7315-0221-0

Die Bände sind unter www.ksp.kit.edu als PDF frei verfügbar oder als Druckausgabe bestellbar.

Band 38 Tim Feser
Untersuchungen zum Einlaufverhalten binärer alpha-Messinglegierungen unter Ölschmierung in Abhängigkeit des Zinkgehaltes. 2014
ISBN 978-3-7315-0224-1

Band 39 Jörg Ettrich
Fluid Flow and Heat Transfer in Cellular Solids. 2014
ISBN 978-3-7315-0241-8

Band 40 Melanie Syha
Microstructure evolution in strontium titanate Investigated by means of grain growth simulations and x-ray diffraction contrast tomography experiments. 2014
ISBN 978-3-7315-0242-5

Band 41 Thomas Haas
Mechanische Zuverlässigkeit von gedruckten und gasförmig abgeschiedenen Schichten auf flexiblem Substrat. 2014
ISBN 978-3-7315-0250-0

Band 42 Aron Kneer
Numerische Untersuchung des Wärmeübertragungsverhaltens in unterschiedlichen porösen Medien. 2014
ISBN 978-3-7315-0252-4

Band 43 Manuel Feuchter
Investigations on Joule heating applications by multiphysical continuum simulations in nanoscale systems. 2014
ISBN 978-3-7315-0261-6

Band 44 Alexander Vondrous
Grain growth behavior and efficient large scale simulations of recrystallization with the phase-field method. 2014
ISBN 978-3-7315-0280-7

Band 45 Tobias Kennerknecht
Fatigue of Micro Molded Materials – Aluminum Bronze and Yttria Stabilized Zirconia. 2014
ISBN 978-3-7315-0293-7

Band 46 Christopher Scherr
Elektrochemisches Verhalten von Lithium-Schwefel-Zellen mit unterschiedlicher Kathodenstruktur. 2015
ISBN 978-3-7315-0296-8

Band 47 Konstantin Frölich
Der Decal-Prozess zur Herstellung katalysatorbeschichteter Membranen für PEM-Brennstoffzellen. 2015
ISBN 978-3-7315-0334-7

Band 48 Benedikt Haspel
Werkstoffanalytische Betrachtung der Eigenschaften von mittels neuartiger RTM-Fertigungsprozesse hergestellten glasfaserverstärkten Polymerverbunden. 2015
ISBN 978-3-7315-0337-8

Band 49 Marco Berghoff
Skalenübergreifende Modellierung und Optimierung vom atomistischen kristallinen Phasenfeldmodell bis zur mesoskopischen Phasenfeldmethode. 2015
ISBN 978-3-7315-0416-0

Band 50 Michael Selzer
Mechanische und Strömungsmechanische Topologieoptimierung mit der Phasenfeldmethode. 2016
ISBN 978-3-7315-0431-3

Band 51 Michael Mahler
Entwicklung einer Auswertemethode für bruchmechanische Versuche an kleinen Proben auf der Basis eines Kohäsivzonenmodells. 2016
ISBN 978-3-7315-0441-2

Band 52 Christoph Bohnert
Numerische Untersuchung des Verformungs- und Bruchverhaltens von einkristallinem Wolfram auf mikroskopischer Ebene. 2016
ISBN 978-3-7315-0444-3

Band 53 Stefan Guth
Schädigung und Lebensdauer von Nickelbasislegierungen unter thermisch-mechanischer Ermüdungsbeanspruchung bei verschiedenen Phasenlagen. 2016
ISBN 978-3-7315-0445-0

Band 54 Markus Klinsmann
The Effects of Internal Stress and Lithium Transport on Fracture in Storage Materials in Lithium-Ion Batteries. 2016
ISBN 978-3-7315-0455-9

Die Bände sind unter www.ksp.kit.edu als PDF frei verfügbar oder als Druckausgabe bestellbar.

Band 55 Thomas Straub
Experimental Investigation of Crack Initiation in Face-Centered Cubic Materials in the High and Very High Cycle Fatigue Regime. 2016
ISBN 978-3-7315-0471-9

Band 56 Maren Lepple
Kupfer- und Eisenoxide als Konversions-Elektrodenmaterialien für Lithium-Ionen-Batterien: Thermodynamische und Elektrochemische Untersuchungen. 2016
ISBN 978-3-7315-0482-5

Band 57 Stefan Andreas Slaby
Charakterisierung und Bewertung der Zug- und Ermüdungseigenschaften von Mikrobauteilen aus 17-4PH Edelstahl. Ein Vergleich von mikropulverspritzgegossenem und konventionell hergestelltem Material. 2017
ISBN 978-3-7315-0484-9

Band 58 Kumar Ankit
Phase-field modeling of microstructural pattern formation in alloys and geological veins. 2016
ISBN 978-3-7315-0491-7

Band 59 Kuo Zhang
Characterization and Modeling of the Ratcheting Behavior of the Ferritic-Martensitic Steel P91. 2017
ISBN 978-3-7315-0503-7

Band 60 Nicht erschienen

Band 61 Fabian Lemke
Untersuchung des Sinterverhaltens von $SrTiO_3$ unter Berücksichtigung der Defektchemie. 2016
ISBN 978-3-7315-0510-5

Band 62 Johannes Kümmel
Detaillierte Analyse der Aufbauschneidenbildung bei der Trockenzerspanung von Stahl C45E mit Berücksichtigung des Werkzeugverschleißes. 2016
ISBN 978-3-7315-0518-1

Band 63 László Hagymási
Modellierung der Stoffübertragung beim Niederdruckcarbonitrieren mit Ammoniak und Acetylen. 2016
ISBN 978-3-7315-0568-6

Band 64 Reza Eslami
A novel micro-mechanical model for prediction of multiaxial high cycle fatigue at small scales. 2017
ISBN 978-3-7315-0583-9

Band 65 Sebastian Schulz
Phase-field simulations of multi-component solidification and coarsening based on thermodynamic datasets. 2017
ISBN 978-3-7315-0618-8

Band 66 Markus Stricker
Die Übertragung von mikrostrukturellen Eigenschaften aus der diskreten Versetzungsdynamik in Kontinuumsbeschreibungen. 2017
ISBN 978-3-7315-0658-4

Band 67 Luis Straßberger
Untersuchung und Modellierung des viskoplastischen Verformungsverhaltens oxidpartikelverstärkter Stähle. 2018
ISBN 978-3-7315-0674-4

Band 68 Mark Wobrock
Microplasticity of idealized single crystalline Ag cantilevers characterized with methods of high resolution. 2017
ISBN 978-3-7315-0682-9

Band 69 Amritesh Kumar
Micromechanical study on the deformation behaviour of directionally solidified NiAl-Cr eutectic composites. 2017
ISBN 978-3-7315-0694-2

Band 70 Johannes Hötzer
Massiv-parallele und großskalige Phasenfeldsimulationen zur Untersuchung der Mikrostrukturentwicklung. 2017
ISBN 978-3-7315-0693-5

Band 71 Thomas Hupfer
Herstellung von LATP für den Einsatz als Festkörperelektrolyt und dessen Eigenschaften. 2017
ISBN 978-3-7315-0702-4

Band 72 Florentin Pottmeyer
Schädigungsverhalten von in CFK-Laminaten eingebetteten Inserts unter bauteilnahen Beanspruchungen. 2017
ISBN 978-3-7315-0719-2

Die Bände sind unter www.ksp.kit.edu als PDF frei verfügbar oder als Druckausgabe bestellbar.

Band 73 Andres Höweling
Untersuchung der Hochvoltstabilität und Tiefentladung von dotierten $\mathrm{LiNi_{0,5}Mn_{1,5}O_4}$-Hochvoltspinellen. 2018
ISBN 978-3-7315-0728-4

Band 74 Tabea Gisela Schwark
Deformation and Fracture Properties of the Soft Magnetic Composite Somaloy 700 3P on Different Length Scales. 2018
ISBN 978-3-7315-0759-8

Band 75 Klaudia Lichtenberg
Metallmatrixverbunde mit Verstärkungselementen aus metallischem Glas $\mathrm{Ni_{60}Nb_{20}Ta_{20}}$ – Herstellung und Charakterisierung. 2018
ISBN 978-3-7315-0782-6

Band 76 Claudio Findeisen
Charakterisierung und Modellierung von instabilen Metamaterialien. 2019
ISBN 978-3-7315-0869-4

Band 77 Nilesha Mishra
Influence of strain on the functionality of ink-jet printed thin films and devices on flexible substrates. 2019
ISBN 978-3-7315-0853-3

Band 78 Simon Werner Bonk
Plastische Verformungsmechanismen in hochgradig kaltgewalzten, ultrafeinkörnigen Wolframblechen. 2019
ISBN 978-3-7315-0878-6

Band 79 Tim Gräning
Herstellung, Charakterisierung und Optimierung von austenitischen ODS Stählen. 2019
ISBN 978-3-7315-0732-1

Band 80 Peter Rupp
Herstellung, Prüfung und Modellierung neuartiger hybrider Aluminiumschaum-CFK-Sandwichverbunde. 2019
ISBN 978-3-7315-0880-9

Band 81 Benjamin Sebastian Ehreiser
Einfluss mechanischer Lasten auf die Herstellung von Stahl-Glaskeramik-Verbunden. 2019
ISBN 978-3-7315-0954-7

Band 82 Hans Giel
Weiterentwicklung experimenteller Methoden zur Ermittlung thermodynamischer Werkstoffdaten von Lithium-Ionen-Batterien. 2020
ISBN 978-3-7315-0981-3

Band 83 Anna Trauth
Characterisation and Modelling of Continuous-Discontinuous Sheet Moulding Compound Composites for Structural Applications. 2020
ISBN 978-3-7315-0950-9

Band 84 Jonas Johannes Hüther
The Impact of Recycling on the Fibre and the Composite Properties of Carbon Fibre Reinforced Plastics. 2020
ISBN 978-3-7315-0983-7

Band 85 Nicolas A. Mayer
Thermodynamik von Kobaltoxid Anodenmaterialien für Lithium-Ionen-Batterien und ihr elektrochemisches Verhalten. 2020
ISBN 978-3-7315-0996-7

Band 86 Ulrich Führer
Untersuchung und Modellierung des Haltezeiteinflusses auf die zyklische Entfestigung ferritisch-martensitischer Stähle. 2020
ISBN 978-3-7315-0837-3

Band 87 Ebru Cihan
Structure evolution in tribological interfaces studied by multilayer model alloys. 2020
ISBN 978-3-7315-0999-8

KARLSRUHER INSTITUT FÜR TECHNOLOGIE (KIT)
SCHRIFTENREIHE DES INSTITUTS FÜR ANGEWANDTE MATERIALIEN

Understanding of the governance of friction and wear of metallic surfaces is of an on-going endeavor for engineers and scientists since when examining the industrial world of the 21st century; one would definitely meet with a considerable amount of energy dissipation during friction processes that brings about huge economic impact. Furthermore, it becomes extremely difficult to predict friction and wear behavior of metallic surfaces when the influence of sub-surface deformations during sliding is taken into account. Recent studies of deformation mechanisms of metals and alloys pioneer the better investigation of the friction and wear behavior of materials with well-defined initial microstructures. Within this scope, in this book, the effect of sub-surface deformations on the resulting friction and wear behavior has been searched by means of a systematic experimental study on Au-Ni metallic multilayer model alloy system.

ISBN 978-3-7315-0999-8
9 783731 509998 >

ISSN 2192-9963
ISBN 978-3-7315-0999-8

Gedruckt auf FSC-zertifiziertem Papier